VORTEX-ENHANCED HEAT TRANSFER BY A NEW DELTA-WINGLET ARRAY

BY

JING HE

DISSERTATION

Submitted in partial fulfillment of the requirements
for the degree of Doctor of Philosophy in Mechanical Engineering
in the Graduate College of the
University of Illinois at Urbana-Champaign, 2012

Urbana, Illinois

Doctoral Committee:

Professor Anthony M. Jacobi, Chair and Director of Dissertation Research
Professor Predrag S. Hrnjak
Professor John G. Georgiadis
Associate Professor Xinlei Wang

ABSTRACT

Liquid-to-air and phase-change heat exchanger performance is crucial to meet efficiency standards with low cost and environmental impact in numerous end-use energy applications. Research on performance improvement of heat exchangers often focuses on the air side because transport coefficients are inherently lower for air than for liquid or two-phase flow. Vortex generation has emerged as a promising method for enhancing air-side heat transfer. Compared to fin interruption, this technique has the advantage of low cost and ease of implementation, and is usually accompanied by a modest pressure drop penalty.

In this study, a new vortex-generator array deployed in a "V" is proposed, aiming to utilize favorable interaction between generators and produce strong vortices even at low Reynolds numbers. A preliminary investigation of vortex strength in a water tunnel shows that boosting effects occur in a V-array which makes the design superior to an offset arrangement. The strongest vortex is measured for a two-row zero-spacing V-array deployed at 30º. The impact of V-formation arrays on heat transfer is assessed in a developing channel flow using infrared thermography. Over a Reynolds number range based on channel height of 340 to 940, the two-pair V-array yields the largest augmentation of 14-32% in heat transfer, as compared to 7-19% and 15-27% obtained from the conventional two-row pairs and the three-pair V-array, respectively. CFD analysis is also conducted to illustrate the evolving counter-rotating longitudinal vortices and to provide pressure drop data. Based on the heat transfer and pressure drop performance and taking other factors such as manufacturing cost and spatial constraints

into consideration, the two-pair V-array deployed at 30º is recommended as an appropriate design for implementation in prototype plain-fin heat exchangers.

The proposed design is finally examined in a prototype plain-fin-and-tube heat exchanger through full-scale wind-tunnel testing under dry surface conditions. Overall performance evaluation using the criteria of the modified area goodness factor and the volume goodness factor indicates superiority of the heat exchanger enhanced by the V-array. The average enhancement ratio of 1.21 in the modified area goodness factor could lead to a 25% reduction in the required heat transfer area. As a result, the heat exchanger can be manufactured with less material, which allows more compactness and reduced cost. The VG array is found more effective at comparatively low Reynolds numbers, representative of many HVAC&R applications and compact heat exchanger designs.

ACKNOWLEDGEMENTS

My much appreciation and gratitude first go to my advisor, Professor Anthony Jacobi, for his wisdom, insight, and enthusiasm in guiding my research, and particularly, for his perseverance with me throughout my graduate life. This work would not have been possible without his consistent encouragement and support. I also want to thank other committee members, Professor Predrag Hrnjak, Professor John Georgiadis, and Professor Xinlei Wang for their time and efforts in supervising my study. My fellow colleagues at the Air Conditioning and Refrigeration Center (ACRC), who endured this long process with me, deserve my best thanks for their friendship and assistance.

Financial support from ACRC and ASHRAE is gratefully acknowledged. Martin Kaern conducted the ink visualization experiments. Junling Xie assisted in the CFD simulation. The heat exchanger sample and infrared thermal imager were provided by Luvata and Creative Thermal Solutions Co., respectively.

As a personal note, I would like to thank my father and mother, Zaibin He and Shaofen Wang, who devote their lives to raising and educating my brother and me. Special thanks to my beloved wife, Liping Liu, who brightens my life and always stands by my side during the ups and downs of those past years.

TABLE OF CONTENTS

LIST OF FIGURES

LIST OF TABLES

NOMENCLATURE

ENGLISH SYMBOLS

A	=	heat transfer area, m^2
b	=	winglet height, m
c	=	winglet chord, m
C_p	=	specific heat, J/kg-K
c_1	=	radiative Nusselt number, $\sigma T_0^3 H / k_f$
c_2	=	normalized heating power, $q_s / \sigma T_0^4$
D	=	tube diameter, m
F	=	correction factor
$F_{k\to l}$	=	view factor from area k to l
f	=	Fanning fraction factor
G	=	irradiation normalized by the external heating flux, q_s, or mass flux at minimal free flow area, kg/m^2-s
g	=	gravitational acceleration, m/s^2
Gr	=	Grashof number, $g\beta H^3 \Delta T_{ref} / \nu_f^2$
H	=	channel height, m
h	=	heat transfer coefficient, W/m^2-K
h_0	=	natural convection coefficient, W/m^2K
J	=	normalized radiosity by the external heating flux, q_s
j	=	Colburn j factor
k	=	thermal conductivity, W/m-K

L	=	flow length, m
L_1	=	length of the opaque, insulated region on the top wall, m
L_2	=	length of the transparent region on the top wall, m
$LMTD$	=	log mean temperature difference, ºC
$\dot{m}$	=	mass flow rate, kg/s
Nu	=	Nusselt number
P	=	dimensionless pressure, $p/(\rho_f u_0^2)$
p	=	pressure, Pa
Pr	=	Prandtl number
PW	=	pumping power
Q	=	normalized heat flux by the external heating flux, q_s, or heat transfer rate, W
q_s	=	external heating flux, W/m^2
R	=	thermal resistance, K/kW
Re	=	Reynolds number
R_{eq}	=	equivalent radius for circular fin, m
S	=	source term
T	=	temperature, K
U	=	dimensionless velocity in X-coordinate, u/u_0 , or overall heat transfer coefficient, W/m^2-K
u	=	velocity in x-coordinate, m/s
u_0	=	incoming air velocity, m/s

V = dimensionless velocity in Y-coordinate, v/u_0

v = velocity in y-coordinate, m/s

X = dimensionless x-coordinate, x/H

x = x-coordinate, m

X_L = half longitudinal tube pitch, m

X_M = half transverse tube pitch, m

Y = dimensionless y-coordinate, y/H

y = y-coordinate, m

z = z-coordinate, m

GREEK SYMBOLS

α = thermal diffusivity, m^2/s

β = volumetric thermal expansion coefficient, K^{-1}, or angle of attack

Γ = effective diffusion coefficient

δ = fin thickness, m

ε = emissivity

η = fin efficiency

θ = dimensionless temperature, $T/\Delta T_{ref}$

ξ = uncertainty in heat transfer rate

ρ = density, kg/m^3; reflectivity

σ	=	Stefan-Boltzmann constant, 5.67×10^{-8} W/(m^2-K^4), or surface ratio A_{min}/A_{front}
τ	=	transmissivity
μ	=	dynamic viscosity, N-s/m^2
ν	=	kinematic viscosity, m^2/s
ω	=	weighting factor of heat transfer rate
ϕ	=	generalized dependent variable
ΔT_{ref}	=	reference temperature difference, $q_s H / k_f$
ΔW	=	affected width, m

SUBSCRIPTS

a	=	air
ave	=	average
c	=	coolant
cond	=	conduction
Cu	=	copper
dh	=	hydraulic diameter
down	=	downstream of heat exchanger
e	=	exterior surface of the transparent sheet
f	=	fluid or fin
front	=	frontal area of heat exchanger
i	=	interior surface of the channel, inlet, or inside
k	=	*k*th area

l	=	*l*th area
m	=	mean value over a channel cross section
min	=	minimum
o	=	outlet, outside, or overall
s	=	substrate
tot	=	total
up	=	upstream of heat exchanger
w	=	wall
0	=	ambient or inlet properties

SUPERSCRIPTS

cond	=	conduction
conv	=	convection
rad	=	radiation

CHAPTER 1

INTRODUCTION

1.1 Introduction

High heat-exchanger performance is crucial to meet efficiency standards with low cost and environmental impact in numerous end-use energy applications, especially in heating, ventilation, air-conditioning and refrigeration (HVAC&R) systems. According to recent statistics by the U.S. Department of Energy, HVAC&R systems account for 54% of the total energy consumed in residential buildings (~11×10^{15} Btu) and 57% in commercial buildings (~9×10^{15} Btu). Achieving even a small amount of performance enhancement in heat exchangers could have profound implications in technical, economical and ecological aspects. Because transport coefficients are inherently lower for air than for liquid or two-phase flow, the air-side convective resistance is usually dominant in typical liquid-to-air and phase-change heat exchangers, representing 75-90% of the total thermal resistance. This limitation, along with the desire to improve heat-exchanger performance with reduced volume and manufacturing and operating costs, continues to motivate research in air-side heat transfer enhancement. Two widely used techniques are interrupted fins and vortex generation.

Fin interruption causes boundary layer restarting and periodic vortex shedding above some critical Reynolds number. The former reduces average boundary-layer thickness and the latter promotes flow oscillation and unsteadiness. Both result in increased heat transfer coefficient (DeJong and Jacobi, 1997). Common interruptions appear in slit-fin, offset-strip and louvered-fin patterns. Kays and London (1998) provided a comprehensive database of heat transfer and flow friction for a variety of modified surfaces. More recent studies can be found in Webb and Kim (2005).

Vortex generation is another technique that holds promise in surface convection enhancement. In this method, a passive flow manipulator, known as vortex generator (VG), is punched or mounted on a heat-transfer surface. As the flow encounters the VG,

the adverse pressure gradient causes the boundary layer to separate along the leading edge and form a vortex system as shown in Fig. 1.1. The vortices are advected downstream and persist for a length of many VG sizes. Presence of the vortices improves thermal transport by boundary layer modification, enhanced mixing or unsteadiness, and flow destabilization. This enhancement technique has the advantage of low cost and ease of implementation, and is usually accompanied by a modest pressure drop penalty.

Considerable research has been undertaken on heat transfer augmentation by vortex generation for different generator shapes, surface geometries, and flow conditions. The study in this dissertation focuses on vortex-enhanced channel flows because of their relevance to heat-exchanger configuration. A literature review is first conducted to outline the current status in this area. The review is organized in the order of *i*) channel flows without tubes, *ii*) channel flows with round tubes, *iii*) channel flows with flat/oval tubes, *iv*) flows in prototype heat exchangers, and *v*) a brief comparison between fin interruption and vortex generation. Novelty of a proposed V-formation delta-winglet array is discussed next, followed by a statement of objectives.

1.2 Literature Review

1.2.1 Channel Flow without Tubes

A plain channel is representative of single element of plain-fin crossflow heat exchangers. Tiggelbeck *et al*. (1993) investigated heat transfer enhancement and flow loss in a channel with double rows of punched delta-winglet pairs. The experiments consisted of flow visualization by laser light sheet, unsteady liquid crystal thermography (LCT) for local heat transfer and a balance measurement for drag. Two arrangements, with the second row either aligned or staggered relative to the first row, were considered. The flow structures behind the second row were observed to be qualitatively similar where the vortices exhibited more unsteadiness in both configurations. At Re=4600 and an attack angle of 45º, the aligned geometry yielded 60% increase in heat transfer and 145% additional pressure drop, as compared to a value of 52% and 129% in the staggered case. The higher performance of the aligned geometry may be due to the tendency of a

common inflow pair to remain close to the surface, while a common outflow pair tends to move away (Jacobi and Shah, 1995).

Biswas *et al*. (1994) computed laminar flow and heat transfer characteristics associated with a punched delta wing or winglet pair in a rectangular channel. Inclusion of the holes beneath in the computational domain was found to reduce the average Nusselt number and the friction coefficient. By observation of a downwash velocity field in the presence of holes, the authors attributed the reduction in flow loss to the spiral flow with less vortex strength. Their simulation also indicated that the delta wing performed better than the winglet pair in heat transfer but was less effective in terms of entropy generation based on an irreversibility analysis.

Gentry and Jacobi (2002) measured vortex strength, local and average mass transfer, and pressure drop in a developing channel flow with a delta wing placed at the leading edge. It was revealed that tip vortices had a significant impact on transport characteristics for both walls. Local enhancements as high as 150% were found in regions where a vortex induced a normal inflow. They reported area-averaged enhancement of 20-50% for Reynolds numbers in the range 400-2000, accompanied by an additional pressure loss up to 110%. Vortex strength and pressure drop increased with Reynolds number, wing aspect ratio and angle of attack, which was consistent with the findings for flat-plate flows.

Yuan *et al*. (2003) investigated heat transfer and pressure drop in a duct mounted with rectangular-winglet rows. Their work confirmed superiority of longitudinal vortices to transverse vortices in heat transfer augmentation. Over the parametric space considered, the impact of duct aspect ratio on thermal-hydraulic performance was found to be much more significant than the winglet spacing.

Dietz *et al*. (2006) employed the commercial software FLUENT to compute heat transfer and velocity field in a turbulent channel flow for Reynolds numbers between 80,000-600,000. The effects of number of delta wings, lateral and longitudinal displacement were analyzed. Predictions on heat transfer at varying wing numbers and displacements were also compared with the measurement using LCT. While the numerical model overpredicted the enhancement ratio by roughly 25%, it captured the

trend in a reasonable manner. For a number of two wings, variation in the longitudinal displacement had little influence on the enhancement. Addition of a third wing did not improve heat transfer appreciably.

Wu and Tao (2008) performed a numerical study on heat transfer and flow characteristics in a rectangular channel with punched VGs at various geometries. Under a fixed VG area, a delta-winglet pair introduced higher heat transfer than a rectangular-winglet pair and judiciously decreasing the aspect ratio of rectangular VGs (defined as height to chord length) could yield further enhancement at a modest pressure drop penalty.

Min *et al*. (2010) compared performance between two winglet shapes, rectangle and octagon (by cutting off the four corners of a rectangle). Their experimental results favored the octagon winglet as it induced higher heat transfer and lower friction for the same VG area. The authors attributed higher heat transfer to a longer edge for generating the vortices and lower friction to the cutting corners that tended to inhibit flow disturbance.

The experimental investigation by Storey and Jacobi (1999) appears to be first to assess the influence of longitudinal vortices on frost growth. They used a scale analysis of simplified equations to guide data interpretation of frost growth in a laminar channel flow. Upon introduction of vortices, the local growth rate increased by over 7% in vortical downwash regions. No heat transfer and pressure drop data were provided.

1.2.2 Channel Flow with Round Tubes

Two commonly employed VG placements in finned-tube geometries are the so called “common-flow-down” and “common-flow-up”, as depicted in Fig. 1.2.

VGs in common-flow-down are placed as a pair downstream of the tube (Fig. 1.2a). The generated longitudinal vortices introduce high-momentum fluid of the main flow toward the fin surface behind the tube, thus improving the poor heat transfer in the wake and suppressing flow separation. Fiebig *et al*. (1993) measured 55-65% heat transfer augmentation with 20-45% increase in the apparent friction factor in the

Reynolds number range 600-2700 for an inline arrangement of three tube rows. For the staggered tube pattern, the associated increases became much lower (below 9%). Rectangular winglet pairs were investigated numerically and experimentally by Leu *et al*. (2004) for three in-line tube rows. Among all considered angles of attack, the 45º arrangement provided the best overall performance and achieved up to 25% area reduction under the variable geometry performance criteria (Webb and Kim, 2005). The improvement was found more pronounced for low-to-moderate Reynolds numbers ($\lesssim$ 2000). O'Brien and Sohal (2005) measured local and overall heat transfer coefficients in a fully developed channel fitted with a circular cylinder and/or a delta-winglet pair over a Reynolds number range based on channel height of 670-6300. The thermal images clearly indicated a reduced wake zone after the addition of the winglet pair. The mean Nusselt number increased by 50-200%, with the highest enhancement achieved at Re=670 which corresponded to typical operating conditions of geothermal air-cooled condensers. A 3D numerical simulation by Wu and Tao (2007) took into account VG thickness, punched holes and conjugate conduction and convection on the fin surface. For elements with three tube rows, the delta-winglet pairs at 30º enhanced the average Nusselt number by 16-20% and simultaneously decreased pressure drop by 8-10% over a Reynolds number range of 800-2000. Aside from the above-mentioned tube-wake manipulation of common-flow-down, the existence of the punched holes also contributes to a reduced pressure drop, albeit in a less important manner.

VGs in common-flow-up are usually located further upstream relative to the tube (Fig. 1.2b), forming a nozzlelike flow passage together with the aft portion of the tube. By promoting fluid acceleration, this design is intended to delay separation on the tube and narrow the wake zone. Torii *et al*. (2002) reported 10-20% heat transfer enhancement and 8-15% pressure drop reduction for inline tube banks. The corresponding values were 10-30% and 34-55%, respectively, for staggered tube banks. The authors (Kwak *et al*., 2005) extended their work by applying a second row of common-flow-up winglet pairs. Instead of simultaneous heat transfer enhancement and pressure drop reduction, they measured less than 9% increase in both heat transfer and pressure drop for inline tube arrangement, and 6-15% increase in heat transfer and 61-117% pressure drop penalty for staggered tube arrangement. To understand the relation between flow field and local heat

transfer, Joardar and Jacobi (2007) performed 3D simulation on a seven-row inline-tube heat exchanger with various delta-winglet arrangements. They identified the impingement of winglet redirected flow on the downstream tube as an important enhancement mechanism. At Re=850, the three-pair inline array caused 74% increase in *j* factor at the cost of 41% additional pressure loss. A similar study was undertaken by Chu *et al*. (2009a). The authors used rectangular winglet pairs and analyzed both inline and staggered fin-tube geometries. The staggered tube bank with seven rows of winglet pairs yielded the highest heat transfer and core pressure drop, but the inline tube bank with a single winglet pair exhibited the best overall performance using the London area goodness factor (*i.e*. *j*/*f*).

While delta and rectangle are the most common shapes for vortex generation, annular VGs were investigated by Lin and Jang (2002) and Wang *et al*. (2002) in fin-tube heat exchangers. As was the case for delta and rectangular winglets, Lin and Jang (2002) showed that performance of annular winglets also improved with its size. Over the parametric range considered, a maximum enhancement of 18.5% in heat transfer, along with 48% increase in the Fanning friction factor, was obtained using the largest generators. This amounted to 20% reduction in the total heat transfer area. Wang *et al*. (2002) compared flow characteristics and pressure drop in staggered fin-tube elements with delta and annular winglets. For the same winglet height, the delta winglet introduced stronger vortical motion and flow unsteadiness, leading to better bulk fluid mixing, as well as lower pressure drop. The pressure drop penalty associated with both winglets was found to be relatively insensitive to Reynolds numbers.

1.2.3 Channel Flow with Flat/Oval Tubes

One may reduce the wake size and drag force by using, instead of round tubes, flat or oval tubes with their major axis parallel to the flow direction. The associated drawback is that the heat transfer coefficient for the flat/oval tube geometry is relatively low because of diminished strength of horseshoe vortex generated by the tube. Additional enhancement can be achieved through the use of VGs.

Fiebig *et al*. (1994) measured heat transfer and flow loss in fin-tube elements with flat or round tubes in staggered arrangements. The implementation of VGs doubled the average Nusselt number for flat tubes, but caused only 10% increase for round tubes. As pointed out by Jacobi and Shah (1995), this was largely due to the positioning of the first row of flat tubes at the leading edge as no horseshoe vortex formed, so the unenhanced flat-tube configuration was artificially inferior and the impact of VGs was almost certain to be greater. Nevertheless, the enhanced flat-tube element offered 30-80% more in heat transfer and 44-60% less in pressure drop as compared to the round-tube element with identical VGs.

Chen *et al*. (1998a, 1998b, 2000) performed a serial numerical investigation in a laminar developing channel flow with a built-in oval tube and punched delta winglets. A finite volume method in body-fitted grids was employed to solve the governing equations. For a single winglet (Chen *et al*., 1998a), the highest enhancement ratio of heat transfer to flow loss, defined as $(j/j_0)/(f/f_0)$, occurred for the winglet with an aspect ratio of 2 and deployed at 30°. These parameters were retained as the authors extended the winglet number up to three (Chen *et al*., 1998b). The values of $(j/j_0)/(f/f_0)$ were computed to be 1.04, 1.01 and 0.97 for one, two and three inline winglets, respectively. Two and four staggered winglets were considered in a later study (Chen *et al*., 2000), with the former yielding the maximum enhancement ratio of 1.151 among all arrangements. The simulation showed that the pressure drop penalty predominately resulted from the form drag of delta winglets and the boost effect by the incoming vortex was more pronounced in the staggered geometry.

Wang and coworkers (2002, 2003, 2004a, 2004b, 2006, 2008, 2009) have been assiduous in studying heat transfer characteristics and pressure drop in a VG-enhanced fin-and-flat-tube heat exchanger (see Fig. 1.3), with the main purpose of seeking an optimal VG design. Naphthalene sublimation experiments were conducted to obtain local heat transfer coefficients using the heat and mass transfer analogy. The results indicated enhancement on both fin surfaces with and without VGs. The enhanced regions on the fin surface without VGs were located further away from the tubes. Overall heat transfer enhancement of 47.5%, 41.4%, and 37.5% was acquired under the constraints of identical mass flow rate, identical pumping power, and identical pressure drop, respectively (Wang

et al., 2002). Based on the performance evaluation criterion of modified area goodness factor, $(j/j_0)/(f/f_0)^{1/3}$, fin spacing of approximately 2 mm (Shi *et al*., 2006) and a winglet height equal to 80% of fin spacing (Gao *et al*., 2003) was recommended for commonly encountered fin thickness and material; winglets should be mounted as close as possible to the tubes (Zhang *et al*., 2004a). Use of six and four winglets per tube yielded highest heat transfer for identical pumping power and pressure drop, respectively (Zhang *et al*., 2004b). For a fixed longitudinal tube pitch, heat transfer improved with the spanwise tube pitch, probably due to less destructive interference between vortices (Liu *et al*., 2008). Chang *et al*. (2009) defined an absolute vorticity flux to relate intensity of the secondary flow to local heat transfer. Their numerical simulation revealed similar streamwise variations between the cross-sectional-averaged absolute vorticity flux and the span-averaged Nusselt number expect for the entrance region.

O'Brien *et al*. (2004) adopted a transient infrared technique to test various geometries (see Fig. 1.4) over a Reynolds number range based on duct height of 670-6300. Comparing to the oval-tube-only case (Fig. 1.4c), use of a single winglet pair (Fig. 1.4f) increased the average Nusselt number by 38% and the friction factor by less than 10%. Addition of a second pair (Fig. 1.4g), however, deteriorated heat transfer performance. Among all the test geometries, a round tube plus a winglet pair oriented at 45º in common-flow-down (Fig. 1.4e) achieved best heat transfer performance.

Chu *et al*. (2009b) performed numerical simulation in a fin-and-oval-tube geometry to assess the effects of VG placement (common-flow-down and common-flow-up), angle of attack (15°, 30°, 45°, and 60°), and number of tube rows (2, 3, 4, and 5). Two or three tube rows with common-flow-down VGs deployed at 30° were recommended in practical heat-exchanger design. For Reynolds numbers based on hydraulic diameter between 500-2500, implementation of delta winglets in a three-row fin-and-oval-tube heat exchanger increased the average Nusslet number by 13.6-32.9% and pressure loss by 29.2-40.6%.

1.2.4 Flow in Prototype Heat Exchangers

Due to the complexity of underlying physics, most work in vortex generation has employed highly idealized geometries and flow conditions. Reports on full-scale testing of VGs in prototype heat exchangers under realistic operating conditions are relatively sparse in the open literature.

Elsherbini and Jacobi (2002) evaluated the impact of leading-edge delta-wing VGs on a plain-fin-and-tube heat exchanger typically used as refrigerating evaporators under dry-surface conditions. They obtained 31% heat transfer enhancement over the baseline, with a modest pressure drop penalty of 10%.

Wang *et al.* (2004) compared air-side performance between delta-winglet VGs and a wavy-fin surface in fin-and-tube heat exchangers under dry- and wet-surface conditions. According to their experiments, performance of the winglet surface relative to the wavy-fin surface improved with the number of tube rows. For a four-row tube element, the winglet surface exhibited superiority in both heat transfer and pressure drop. The authors attributed lower pressure drop under wet conditions to better condensate drainage caused by the swirl motion of vortices.

Joardar and Jacobi (2005) assessed the thermal-hydraulic performance of a flat-tube, louvered-fin compact heat exchanger enhanced by leading-edge delta wings. An average heat transfer augmentation of 21% and 23.4% was achieved for dry and wet conditions, respectively, accompanied by an additional pressure drop of less than 7%. Preferred wing geometries were also determined from flow visualization. The authors later (2008) implemented common-flow-up delta winglets in a plain-fin-and-tube heat exchanger to explore tube-wake management and ran full-scale wind-tunnel experiments over a Reynolds number range based on hydraulic diameter of 220-960. They found that when VGs were attached to the leading tube row only, the air-side heat transfer coefficient increased by 16.5-44% with the pressure drop penalty below 12%; when VGs were attached to three tube rows, heat transfer enhancement increased from 29.9% at Re=220 to 68.8% at Re=960, but the pressure drop penalty decreased from 87.5% to 26%. Their work indicated the usefulness of multiple VG rows in improving the performance of fin-tube heat exchangers typically used in air-cooling and refrigeration applications.

The potential of VG-enhanced flat-tube, louvered-fin heat exchangers was also evaluated by Thole and coworkers (2006, 2008). Instead of attaching delta wings to the leading edge of the test heat exchanger (Joardar and Jacobi, 2005), Sanders and Thole (2006) placed delta or rectangular winglets on the louvers. Using a design of experiments, they identified the trends for parameters including attack angle/aspect ratio/shape/orientation of winglet and distance between winglet and the tube wall. Thermal performance improved with increasing attack angle and winglet size and decreasing winglet distance from tube wall. A maximum enhancement of 38% was achieved at the highest Reynolds number of 1016 using rectangular winglets. The friction factor also increased with attack angle and winglet size as expected, but no strong generalization could be made about winglet distance from tube wall. Lawson and Thole (2008) punched delta winglets out of the louvered fins as part of an actual manufacturing process. Piercings were found to diminish heat transfer augmentation by disrupting the vortex formation but exhibit the desirable effect of lowering pressure loss. Without piercings, increases of 47% in heat transfer and 19% in pressure loss were reported at Re=955. The former value was halved in the presence of piercings. The authors concluded vortex generation as a viable method for performance improvement in practical production of louvered-fin heat exchangers.

The experimental investigation by Wu *et al*. (2012) was among the few that showed simultaneous heat transfer enhancement and pressure drop reduction after applying longitudinal VGs. Delta-winglet pairs, in either common-flow-up or common-flow-down orientation, were punched out of the first tube row in a staggered plain-fin-and-tube heat exchanger. At a frontal air velocity of 4.0 m/s, they reported 16.5% enhancement in air-side heat transfer coefficient and 10% reduction in pressure drop for the common-flow-up pairs. The common-flow-down pairs increased air-side heat transfer coefficient by 28.2% with approximately the same pressure drop as the baseline.

Sommers and Jacobi (2005) estimated the efficacy of longitudinal vortices as an air-side enhancement technique under frosting conditions. The delta-wing VGs were attached in an alternating single-row, double-row arrangement in a plain-fin-and-tube heat exchanger. For Reynolds numbers between 500-1300, the convective heat transfer coefficient increased by 60-93% with nearly identical core pressure drop. The enhanced

frost density suggested that vortex-induced flow suppressed dendritic frost growth and hence produced a frost layer with higher thermal conductivity.

1.2.5 Comparison between Fin Interruption and Vortex Generation

There have been a number of studies comparing the effectiveness of fin interruption and vortex generation. Due to the tremendous diversity in fin patterns, VG geometries, and flow conditions, it is not feasible to make a definitive judgment on the two techniques (Lozza and Merlo, 2001). However, to the author's knowledge, the potential of vortex generation has been recognized in the following aspects:

- *Relatively modest pressure drop penalty.* For example, the winglet fin tested by Lozza and Merlo (2001) exhibited lower friction factor than all standard louvered fins with the sole exception of a best coil having the smallest louver height. In comparison between louvered-fin surface and plain-fin surface with punched delta winglets, Allison and Dally (2007) measured 30% reduction in *j*-factor and 47% reduction in *f*-factor by the winglet surface over a Reynolds number range based on hydraulic diameter of 660-1360. This amounted to a 46% saving in the pumping power for the same heat transfer capacity. In the presence of tubes, it is even possible achieve pressure drop reduction through tube-wake management as reported by Torii *et al*. (2002), Wu and Tao (2007), and Wu *et al*. (2012).
- *Improved thermal-hydraulic performance under wet-surface conditions* (Wang *et al*., 2004). For fin-tube heat exchangers under dehumidifying conditions, the swirl motion induced by VGs assists in removing condensate, thereby reducing blockage in the flow passage and lowering pressure drop. With better condensate drainage, heat transfer performance is also improved.
- *Further enhancement possible through careful design and deployment of VGs*. Tang *et al*. (2009) demonstrated that a VG-enhanced plain-fin heat exchanger, after optimization with respect to winglet dimensions and attack angle, could offer higher heat transfer and lower pressure drop than a conventional slit-fin heat exchanger. Note that the essence of the current study is also to propose a

VG array that may create constructive interference between vortices and therefore improve VG performance.

- *Ease of manufacture and maintenance*. Vortex-enhanced heat exchangers with punched delta-winglet pairs were manufactured and tested by Wu *et al*. (2012). The authors believed that comparing to slotted or louvered fin, the fin with punched VGs has the advantages of simple die-making, slow dust deposition and easy cleaning. The design complexity, tooling change, and raw material scrap reduction remain similar.

1.3 Objectives

1.3.1 Novelty of the Proposed Research

Prior research on vortex generation has addressed appropriate arrangement for a single winglet pair or a row of winglet pairs placed at the leading edge. The key conclusions were summarized by Fiebig (1998). Prior research has also explored tube-wake management (see Fig. 1.2a for common-flow-down and Fig. 1.2b for common-flow-up) and multirow pairs in either aligned or staggered configuration (Fig. 1.5a). However, prior research has never considered VGs deployed in an array (e.g. Fig. 1.5b) that may generate stronger vortices through constructive interference.

The array structure proposed in this study is inspired by the "V" formation of migrating birds (Fig. 1.6a). Group movement of animals in nature provides a variety of benefits, among which hydrodynamic efficiency plays an important and sometimes dominant role. Lissaman and Shollenberger (1970) applied aerodynamic theory to predict that 25 birds in a "V" could have a flight range increase of about 70% over a solo bird, with the posterior birds "riding" on the upwash of tip vortices generated from the upstream members. It is interesting to note such a V-like or echelon (i.e. half V) configuration in fish schooling (Fig. 1.6b) and arthropod queues (Fig. 1.6c) as well. Fish swimming in a "V" pattern were found to exploit vortices shed by others in the school, thus achieving a significant decrease of consumed energy (Weihs, 1973). Chainlike aggregation of spiny lobsters, as observed in a recently discovered fossil (Hou *et al*.,

2008), takes advantage of the fact that an object placed closely downstream of another usually results in a lower total drag than that when the two objects are separated far apart (Saleh, 2002). These shape adaptations have evolved for lowered power demands and improved energy efficiency, thereby promoting survival of the species in the Darwinian sense (Bushnell and Moore, 1991). Although the inherent enhancement mechanisms may be different, the essential idea of grouping individuals in advantageous positions for favorable interaction could be utilized in human fluid-flow technology. The present work aims to fulfill one such realization.

1.3.2 Objectives and Outline

There are at least two challenges in the design of VG-enhanced heat exchangers. First, because vortex strength is proportional to Reynolds number based on VG size, maintaining strong vortices at low-*Re* applications, as encountered in compact geometries and/or low frontal air velocities, is a challenge. The second challenge is to identify an optimal array spacing that allows vortices to affect as much heat transfer area as possible while avoiding destructive interaction between them. Both challenges are expected to be surmounted through the use of a novel V-formation VG array. The objectives of this research are to:

- demonstrate constructive interference promoted by the V-array;
- develop design guidelines for array geometry and propose an appropriate array for plain-fin heat exchangers;
- analyze vortex interaction and flow structure using CFD simulation;
- assess the performance impact of the proposed array in application.

The content of the remaining chapters is briefly summarized below:

- Chapter 2 describes measurement of vortex circulation in a closed-circuit water tunnel using the ink visualization technique. The experiment serves as a preliminary screening of potential optimal geometries due to its ease of implementation and reasonable accuracy.

- Chapter 3 presents experimental and numerical investigations in a developing channel flow, aiming to refine the design obtained from the vortex measurement. A high-aspect-ratio duct was built to simulate a single passage of plain-fin heat exchangers, with an opaque, uniformly heated wall on the bottom and a transparent wall on the top. Temperature distributions on the heated surface were first measured in a plain channel using infrared thermography and compared to numerical predictions by a fully conjugate heat transfer model. The test VG candidates were then embedded into the channel to quantify heat transfer enhancement. CFD analysis was also conducted to reveal flow structure and provide pressure drop data. Finally, an appropriate array was proposed based on the overall performance.
- Chapter 4 discusses the effectiveness of the proposed array in a prototype plain-fin-and-tube heat exchanger by running full-scale wind-tunnel testing over a Reynolds number range representative of many HVAC&R applications.
- Chapter 5 summarizes the conclusions from all the investigations and recommends future work in the area of vortex-enhanced heat transfer.

1.4 Figures

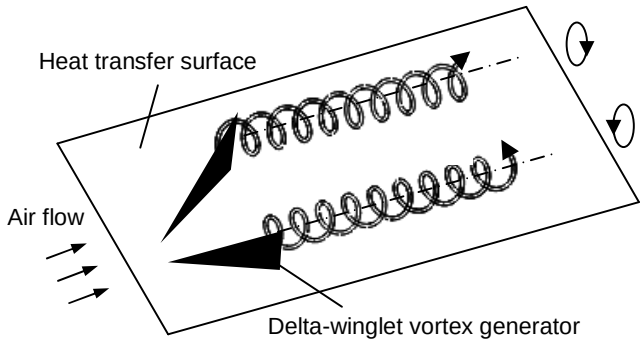

Figure 1.1 Schematic of longitudinal vortices generated by a pair of delta-winglet vortex generators.

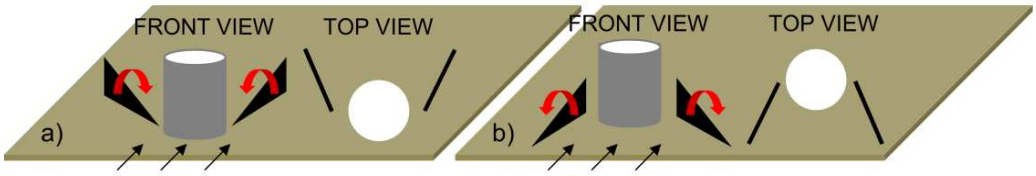

Figure 1.2 Configuration of winglet-type VGs on a fin surface: a) common-flow-down and b) common-flow-up.

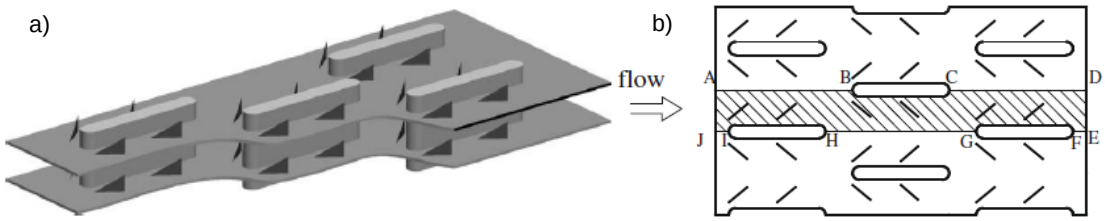

Figure 1.3 a) Isometric and b) cross-sectional view of a staggered three-row fin-and-flat-tube heat exchanger (adapted from Chang *et al*., 2009).

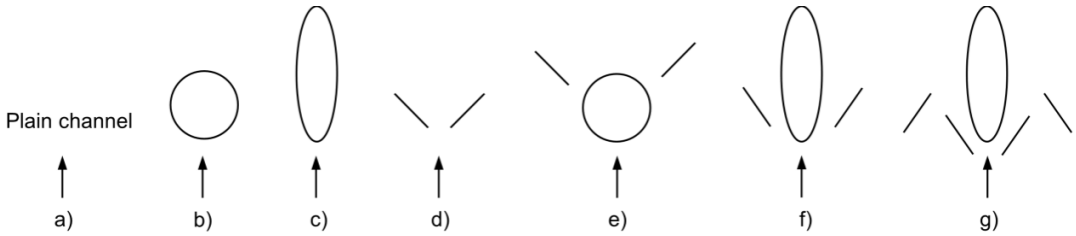

Figure 1.4 Test geometries in O'Brien *et al*. (2004).

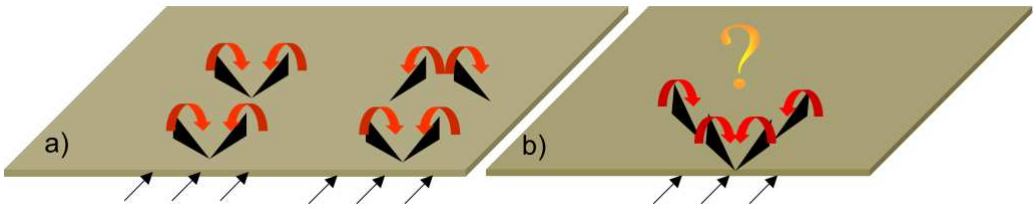

Figure 1.5 a) Multirow winglet pairs in aligned or staggered configuration and b) V-formation winglet array.

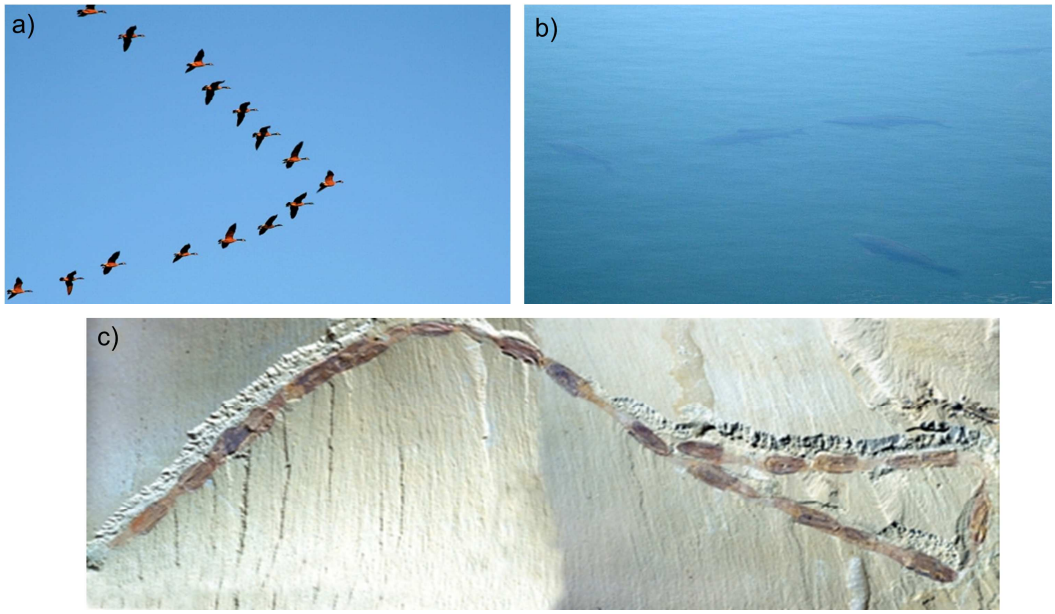

Figure 1.6 a) Migrating birds in V-formation (reproduced by courtesy of Tom Samoden), b) fish in a V-patterned school (photo courtesy of http://www.emma-o.net/photography_critters.htm), and c) fossilized collective behavior of shrimplike arthropods in a conga line (reproduced with permission from Hou *et al*., 2008).

CHAPTER 2

VORTEX MEASUREMENT IN A WATER TUNNEL

Vortex strength in terms of the rotation rate was measured in a closed-circuit water tunnel using ink visualization and a vane-type vortex meter. Due to its ease of implementation and reasonable accuracy, the experiment serves as a preliminary screening of potential optimal geometries. This chapter describes briefly the experimental facility, the method of vortex measurement, and the results[†].

2.1 Experimental Facility

2.1.1 Water Tunnel

The closed-circuit water tunnel for flow visualization and vortex measurement is schematically shown in Fig. 2.1. It was equipped with a single-stage, axial-flow, impeller pump powered by a 0.37 kW/230V, single-phase, AC induction motor. Water was pumped to the delivery plenum which contained two wire-mesh screens and honeycomb flow straightener to reduce unsteadiness and turbulence level, and then passed to the test section and discharge plenum. The discharge plenum was configured such that no flow disturbance could propagate upstream. The water finally returned to pump inlet from the bottom of the discharge plenum to complete the loop. The interior of the tunnel was constructed of sheet metal and coated with gel epoxy resin spray to form smooth finished surface. The test section was nominally 300 mm wide, 300 mm high, 450 mm long, and its side walls were made of acrylic Plexiglas to enable visual access.

[†] This part of work was accomplished through an ACRC undergraduate research program. The experiment followed the procedure by Gentry (1998). The full experimental data have been published in ACRC Research Highlights, Issue of May 2007, and only selected data are presented here.

The ink supply system consisted of a reservoir and 0.5 mm diameter micro-injection tube whose end was bent into the flow direction. The ink was fed by gravity, and its volume flow rate was regulated by a needle valve in the tubing. The average velocity in the water tunnel was determined by recording the time elapsed for a marker drop of ink in the water to traverse a known distance. The current facility is capable of generating water velocities from approximately 1.5 cm/s up to 25 cm/s.

2.1.2 Vortex Meter

A vane-type vortex meter depicted in Fig. 2.2 was used to quantify vortex strength in terms of the rotation rate. The body of the vortex meter was a stainless steel tube with 0.36 mm ID and 0.61 mm OD bent to 90°. Two pieces of aluminum foils, each 2 mm by 2 mm by 0.035 mm, were glued together. A 0.2 mm diameter shaft was sandwiched in the center and inserted into the short tube at a depth of approximately 3 mm. The wire inside the long tube was used to prevent the shaft from contacting the end of the long tube. In order to minimize the friction effects, a TEFLON spray (Super Lube®) has been applied to the shaft and the interior of the 90° bend. This product carried TEFLON lubricant in an aerosol that would evaporate leaving a TEFLON layer behind. One side of the vane was silver and the other was painted black to allow an unambiguous detection of the rotational speed by a stroboscopic lighting system.

2.2 Experimental Method and Results

2.2.1 Procedure

Flow visualization and vortex measurement were performed on a flat plate placed symmetrically at the bottom of the test section. The plate was made of thin plastic with a magnetic sheet of identical size attached underneath. The delta winglets were cut off from carbon steel to allow easy adjustment of VG configuration on the plate. The ink was introduced from the windward side near the tip of the leading winglet as shown in Fig. 2.3. Its flow rate was carefully monitored to provide best visualization while avoiding noticeable disturbance to the main flow. The vortex meter was adjusted to be within the

vortex tube immediately downstream the generators where vortices were strongest and most coherent. After circulating the water flow for at least 20 minutes to assure steady state conditions, the flow field was recorded using a digital camera (Nikon coolpix 4500) for post processing, with lighting provided from a photographic floodlight (Smith-Victor, PL-8) and a 500 W incandescent bulb.

2.2.2 Parametric Range and Experimental Uncertainty

The test VG geometries included half-V arrays with zero spacing (Fig. 2.4a), with a spacing of 1 cm between winglets (Fig. 2.4b), and an offset deployment (Fig. 2.4c). Each winglet had a height of 1.5 cm, a chord length of 3.5 cm, and was deployed at an attack angle of 20° or 30°. Up to three rows of winglets were investigated. The water velocity was maintained constant throughout the experiments that corresponded to a Reynolds number based on the chord length of 4420. Although this value is higher than those encountered in many HVAC&R applications, it may be justified in that the constructive interference persists over a wide range of Reynolds numbers, and the optimal geometry obtained from a high-Re investigation still applies to low-Re scenarios.

The experimental uncertainty in circulation measurement is mainly due to uncertainties in locating vortex core and friction on the vane shaft. A conservative estimate based on the experience in using the vortex meter suggested an uncertainty of ±15% (Gentry, 1998).

2.2.3 Results

Vortex strength in terms of the circulation rate is presented in Fig. 2.5. Vortical rotation is boosted as the attack angle increases from 20° to 30°, which is consistent with established findings (Fiebig, 1998). The results indicate that a V-formation array is superior to an offset arrangement, and vortex strength of V-array decreases with spacing between winglets. It is interesting to note that the maximum drag saving for a V-formation bird flight also occurs when the wing tip spacing is zero (Lissaman and Shollenberger, 1970). For the zero-spacing V-array, the boost effect is manifest at a

winglet number of two. Addition of a third winglet, however, does not further accelerate the circulation. Among all investigated configurations, the two-row zero-spacing V-array deployed at 30° produces the strongest vortex.

2.3 Figures

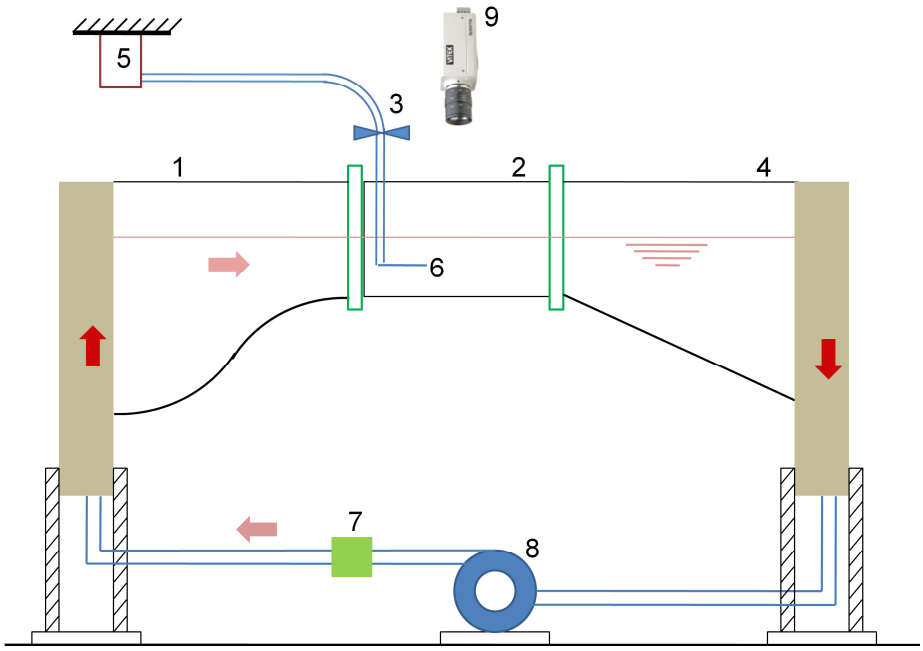

Figure 2.1 Schematic of water tunnel: 1) delivery plenum, 2) test section, 3) needle valve, 4) discharge plenum, 5) ink reservoir, 6) dye nozzle, 7) flow meter, 8) pump, and 9) digital camera.

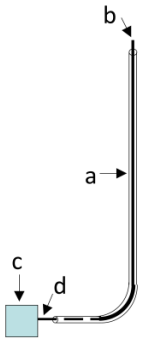

Figure 2.2 Vane-type vortex meter: a) 0.36 mm ID by 0.61 mm OD stainless steel tube bent to 90°, b) wire to ensure correct positioning of the shaft, c) 2 mm by 2 mm by 0.07 mm aluminum foil, and d) stainless steel shaft.

Figure 2.3 Ink visualization for a single winglet on a flat plate.

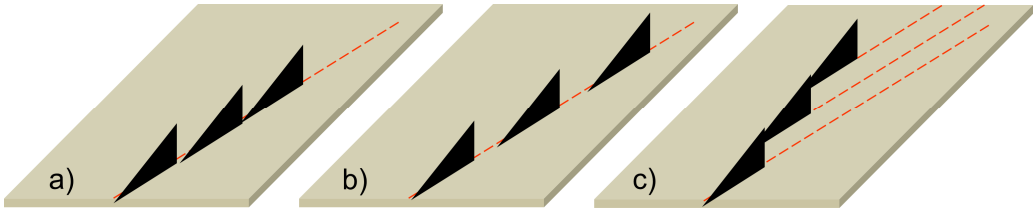

Figure 2.4 Test VG geometries: a) half-V array with zero spacing between winglets, b) half-V array with a spacing of 1 cm between winglets, and c) offset deployment.

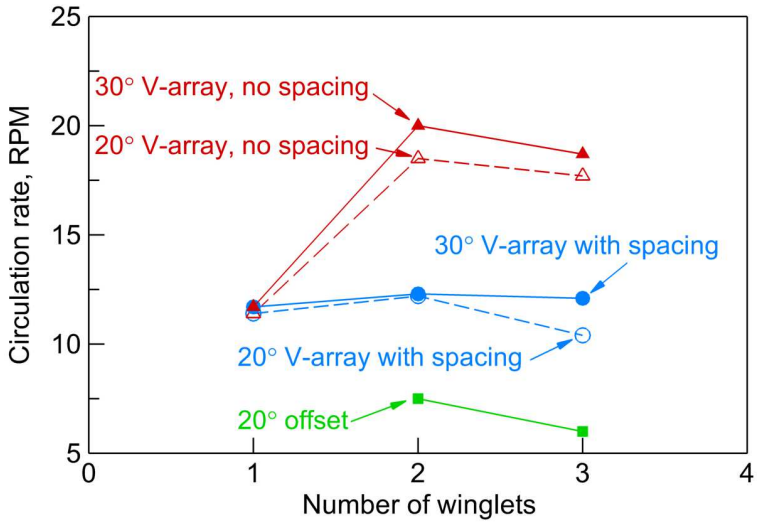

Figure 2.5 Vortex circulation rate (round per minute) for various VG geometries.

CHAPTER 3

EXPERIMENTAL AND NUMERICAL INVESTIGATIONS IN A WIND TUNNEL

In order to refine the design suggested by the vortex measurements presented in the previous chapter, experimental and numerical investigations were undertaken in a developing channel flow. A high-aspect-ratio channel was built to simulate a single passage of plain-fin heat exchangers, with an opaque, uniformly heated wall on the bottom and a transparent wall on the top. Temperature distributions on the heated surface were first measured in a plain channel using infrared thermography and compared to numerical predictions by a conjugate heat transfer model. The test VG candidates were then embedded into the channel to quantify heat transfer enhancement. CFD analysis was also conducted to reveal flow structure and provide pressure drop data. Finally, a candidate array was proposed based on the overall performance.

3.1 Experimental Method

3.1.1 Wind Tunnel

The experiments were conducted in an open-loop, induction wind tunnel shown schematically in Fig. 3.1. The flow was driven by an axial fan and frequency-controlled 1.5 kW AC motor. Air entered the wind tunnel through a square, bell-mouth inlet and then passed through a series of hexagonal-cell, aluminum honeycomb and stainless steel screens to achieve uniform velocity profile. A 9:1 contraction was used to reduce free-stream turbulence and provide a smooth transition into the test section (152 mm × 152 mm). Using a 20-μm hot-wire anemometer, the velocity profile at the entrance of the test section was determined to be flat to within 3%, with a turbulence intensity less than 2% (as reported by Gentry and Jacobi, 2002).

3.1.2 Test Section

The test section, with reference to Fig. 3.2, consisted of a 25.3:1 contraction and the test channel. The contraction profile followed a recommended polynomial curve (Brassard and Ferchichi, 2005), which was designed to achieve flow uniformity and thin boundary layers. The air velocity was measured at the entrance using an 8355 TSI hot-wire anemometer with an accuracy of ±0.01 m/s. The channel measured 6 mm high, 152 mm wide, and was composed of a 170 mm heated section and a 135 mm extended section (not shown in Fig. 3.2). Due to the position of the infrared camera, mounting surface, etc., only the portion between x=5 and 150 mm was in the field of view of the thermal imager. The channel floor was constructed by attaching a 25 μm thick Inconel 625 alloy foil to 3 mm thick Plexiglas that had a thermal conductivity of 0.25 W/m-K. The exterior of the Plexiglas was covered with polyvinyl chloride (PVC) foam to minimize heat leakage. The channel ceiling was made of a 0.46 mm thick polyethylene sheet which allowed minimal absorption loss in the 8-14 μm region according to the manufacturer (Edmund Optics, Barrington, NJ). The total emissivity, reflectivity, and transmissivity were estimated to be 0.45 (Fujikura *et al*., 1982), 0.07 (Il'yasov and Krasnikov, 1973), and 0.48 (Tsilingiris, 2003), respectively. Electric power was supplied from a Mastech HY3030E DC power, imposing an isoflux condition by Joule heating. In order to reduce reflected energy and enhance thermal-image detection, the foil surface facing the camera was painted black to raise its emissivity to 0.98.

Infrared thermography has been widely used in convective heat transfer research due to its noninvasive, full-field data acquisition characteristics and the ability to resolve temporal and spatial temperature distributions. The infrared technique, along with the effective heated-thin-foil method (Astarita *et al*., 2006), was employed in this work for temperature measurement. The infrared system included a computer-controlled Mikron MIDAS thermal imager and the processing software MikroView^{TM}. The sensing system was an uncooled microbolometer detector of 320×240 pixels. During operation, IR radiation emitted from the channel floor was captured, converted into an electrical signal, and displayed as a color or monochrome image. The camera was capable of recording 30 frames per second and digitally storing 16 bit images. The instantaneous field of view

was 1.6 mrad and the minimal focal distance was 305 mm. The measurement resolution was ±2 K, with a thermal sensitivity of 0.08 ºC at 30 ºC. The camera was placed 356 mm away from the heating surface throughout the calibration and measurement process. Using a closer viewing distance to achieve higher spatial resolution was not possible due to geometric constraints of the apparatus.

3.1.3 VG Geometries

The test VG geometries included a single winglet pair (Fig. 3.3a), a two-pair V-array (Fig. 3.3b), conventional two-row winglet pairs (Fig. 3.3c), and a three-pair V-array (Fig. 3.3d). Each winglet was 5.4 mm in height and 16.2 mm in chord, translating to an aspect ratio of 3. The leading pair had zero tip spacing (following the recommendation by Fiebig (1998)) and was placed 17.5 mm away from the entrance. For a V-formation array, the vortex measurement suggested positioning the trailing winglet immediately adjacent to the preceding one. The conventional two-row design had also zero longitudinal displacement between pairs and was selected for comparison. Note that addition of VGs resulted in less than 3% increase in the total heat transfer area. Therefore surface convection enhancement can be predominantly ascribed to the generation of longitudinal vortices.

3.1.4 Experimental Procedure

The infrared system was first calibrated over the desired temperature range by comparing direct measurement of the heated surface without the transparent sheet in place to that obtained by viewing through the sheet. The correlation between the two measurements was found to be almost linear. Air entered the channel at the room temperature (~294 K) and its transport properties were evaluated at 300 K (approximate average temperature). The temperature distribution on the heated surface was measured at three velocities, 0.9, 1.5, and 2.5 m/s, corresponding to Reynolds numbers based on channel height of 340, 570, and 940, respectively. An experiment was initiated by adjusting the fan speed to the desired flow rate, as indicated by the anemometer. The

metallic foil was continuously supplied a current of 12 A (±2.0%), generating a constant heat flux of 257 W/m^2. After a transient period of around 20 minutes, a steady state was deemed to prevail when all temperature readings varied within the experimental uncertainty over at least three minutes. The thermal image and temperature data of the heated surface were then recorded for post analysis. The experiment started in a plain channel without VGs to establish baseline results. The temperature measurement was also compared to numerical predictions by a fully conjugate heat transfer model. Next, a single winglet pair was embedded at 15°, 30° and 45° (Fig. 3.3a), respectively, aiming to identify an appropriate deployment with respect to the angle of attack. The investigation ended with multipair tests fixed at the optimum angle (Figs. 3.3b-3.3d).

3.2 Numerical Method

3.2.1 2D Conjugate Model

A fully conjugate heat transfer model that incorporated mixed convection, radiative exchange, as well as two-dimensional conduction in the substrate, was developed for parallel-plate geometry with transparent walls, as encountered in many thermal energy systems such as solar collectors, glass-melting tanks, and double-pane windows. One purpose of the numerical method is to facilitate heat transfer data reduction in the present channel flow. The model has also been used in a parametric study to assess the impact of channel height, thermal conductivity and thickness of substrate (He *et al*., 2011a), providing further insight and quantitative information for the design of similar thermal equipment.

3.2.1.1 Governing Equations. The test section shown in Fig. 3.2 is modeled as a 2D channel and depicted schematically in Fig. 3.4. 2D simulation is justified for a channel of high aspect ratio and insignificant buoyancy effects (Gr/Re^2 small) (Chiu *et al*., 2001). A thin heat source is located on the channel floor (the 'substrate') to provide a uniform heat flux of q_s. The other sides of the substrate are insulated. The top wall is comprised of a thin transparent sheet with a small opaque, adiabatic portion to mimic the mounting surface for the sheet present in the experiment. Air enters the channel with

uniform velocity and temperature profiles. The nondimensional variables are defined as follows:

$$X=\frac{x}{H};\quad Y=\frac{y}{H};\quad U=\frac{u}{u_0};\quad V=\frac{v}{u_0};\quad \theta=\frac{T}{\Delta T_{ref}}$$

$$\mathrm{Re}=\frac{u_0 H}{\nu_f};\quad P=\frac{p}{\rho_f u_0^2};\quad Gr=\frac{g\beta H^3\Delta T_{ref}}{\nu_f^2} \tag{3.1}$$

The reference temperature difference $\Delta T_{ref}=q_s H/k_f$, and q_s has been used to normalize the heat flux in all dimensionless equations. Assuming steady-state, laminar, Newtonian flow with constant properties, negligible viscous dissipation and pressure work, and accounting for buoyancy effects with the Boussinesq approximation (Bergman *et al*., 2011), the full elliptic governing equations for continuity, momentum and energy are written in a general form of

$$\frac{\partial(U\phi)}{\partial X}+\frac{\partial(V\phi)}{\partial Y}=\Gamma\left(\frac{\partial^2\phi}{\partial X^2}+\frac{\partial^2\phi}{\partial Y^2}\right)+S \tag{3.2a}$$

where the dependent variable ϕ, the effective diffusion coefficient Γ, and the source term S, are expressed as

$$\phi=\begin{bmatrix}1\\U\\V\\\theta\end{bmatrix};\quad \Gamma=\begin{bmatrix}0\\\frac{1}{\mathrm{Re}}\\\frac{1}{\mathrm{Re}}\\\frac{1}{\mathrm{Re\,Pr}}\end{bmatrix};\quad S=\begin{bmatrix}0\\-\frac{\partial P}{\partial X}\\-\frac{\partial P}{\partial Y}+\frac{Gr}{\mathrm{Re}^2}(\theta-\theta_0)\\0\end{bmatrix} \tag{3.2b}$$

3.2.1.2 Conjugate Modeling. The numerical method accounts for mixed convection in the fluid, heat conduction in the substrate, and radiation exchange between the channel surfaces and with ambient. By using a computational domain that includes both the fluid and solid regions, the conjugate problem is solved simultaneously, with a proper matching of temperature and heat flux at the fluid-solid interfaces (Patankar, 1980). In effect, a pure-conduction calculation is carried out in the solid region

$$\frac{\partial^2\theta}{\partial X^2}+\frac{\partial^2\theta}{\partial Y^2}=0 \tag{3.3}$$

The treatment of surface radiation followed the approach by Liu and Sparrow (1980) for parallel-plate configuration, using a net-radiation analysis based on finite areas (Siegel and Howell, 2002). Consider a diffuse, gray enclosure with a transparent wall shown in Fig. 3.5. The inlet aperture is assumed black and isothermal at the inlet air temperature, θ_0, and the exit aperture is assumed black and isothermal at the exit bulk air temperature, θ_m. Radiation exchange occurs between the discrete areas on the wall surfaces, and with the inlet and exit apertures. The net radiative flux at the *k*th area is the radiosity minus the irradiation. For the opaque surface,

$$Q_{k,opq}^{rad} = J_{k,i} - G_{k,i} \tag{3.4a}$$

and for the transparent wall

$$Q_{k,trs}^{rad} = J_{k,i} - G_{k,i} + J_{k,e} - G_{k,e} \tag{3.4b}$$

The radiosity is composed of emitted and reflected energy in Eq. (3.4a). A third component of transmitted energy is also included for $J_{k,i}$ and $J_{k,e}$ in Eq. (3.4b). After applying the reciprocity rule, $G_{k,i}$ in Eq. (3.4) is written as

$$G_{k,i} = \sum_l F_{k\to l} J_{l,i} \tag{3.5}$$

where $F_{k\to l}$ denotes the view factor from element *k* to element *l*, evaluated by Hottel's crossed-string method (Siegel and Howell, 2002). For irradiation from environment, $G_{k,e}$, only blackbody radiation emitted at the incoming air temperature, $\theta_{0,}$ is considered (solar radiation is not included, but the model can be readily modified to do so). Introducing $c_1 = \sigma T_0^3 \cdot H / k_f$ and $c_2 = q_s / \sigma T_0^4$ (Liu and Sparrow, 1980), the radiosity equations for the opaque surface and the transparent wall can be expressed in dimensionless forms as

$$J_{k,i} - \rho_k \sum_l F_{k\to l} J_{l,i} = \frac{\varepsilon_k}{c_2}\left(\frac{\theta_k}{\theta_0}\right)^4 \tag{3.6a}$$

and

$$J_{k,i} - \rho_k \sum_l F_{k\to l} J_{l,i} = \frac{\varepsilon_k}{c_2}\left(\frac{\theta_k}{\theta_0}\right)^4 + \frac{\tau_k}{c_2} \tag{3.6b}$$

respectively. Given the temperature distribution on all discrete areas (for example at each iteration step), Eq. (3.6) forms a complete set of linear equations which is solved by Gaussian elimination (Press *et al.*, 1996).

3.2.1.3 Boundary and Interface Conditions. Air enters the channel with uniform velocity and temperature profiles

$$U = 1, \quad V = 0, \quad \theta = \theta_0 \text{ at } X = 0, \quad \frac{H_s}{H} < Y < 1 + \frac{H_s}{H} \tag{3.7}$$

No-slip and impermeability are imposed on all solid surfaces. The channel modeled in this study is sufficiently long to assume that the streamwise velocity and temperature gradients vanish at its exit

$$\frac{\partial U}{\partial X} = \frac{\partial V}{\partial X} = \frac{\partial \theta}{\partial X} = 0 \text{ at } X = \frac{L_1 + L_2}{H}, \frac{H_s}{H} < Y < 1 + \frac{H_s}{H} \tag{3.8}$$

The unheated sides of the substrate remain insulated

$$\frac{\partial \theta}{\partial X} = 0 \text{ at } X = 0 \text{ or } \frac{L_1 + L_2}{H}, \ 0 \le Y \le \frac{H_s}{H} \tag{3.9a}$$

$$\frac{\partial \theta}{\partial Y} = 0 \text{ at } 0 \le X \le \frac{L_1 + L_2}{H}, Y = 0 \tag{3.9b}$$

The transparent wall is assumed to be very thin such that temperature variation in the Y direction and heat conduction in the X direction are negligible. Thus, an energy balance for the transparent portion $\left(L_1 / H < X \le (L_1 + L_2) / H\right)$ yields

$$\frac{\partial \theta}{\partial Y} + \left(\frac{h_0 H}{k_f} \right) \cdot \left(\theta - \theta_0 \right) + Q_{trs}^{rad} = 0 \tag{3.10}$$

The natural convection coefficient between the outer surface and the environment, h_0, is approximated to be 4.0 W/(m^2·K) (Bergman *et al*., 2011). The small leading portion of the upper wall $\left(0 < X \le L_1 / H\right)$ is opaque and assumed to be adiabatic. Thus, the appropriate boundary condition is

$$\frac{\partial \theta}{\partial Y} + Q_{opq}^{rad} = 0 \tag{3.11}$$

Lastly, for the fluid-solid interface,

$$\frac{k_s}{k_f} \left(\frac{\partial \theta}{\partial Y} \right)_s - \left(\frac{\partial \theta}{\partial Y} \right)_f + Q_{opq}^{rad} = 1 \tag{3.12}$$

3.2.1.4 Solution Method. The governing equations were solved using the SIMPLER scheme (Patankar, 1980) in a staggered grid arrangement, and a tridiagonal matrix algorithm (TDMA) (Press *et al*., 1996) was employed to solve the resulting simultaneous equations. The calculation was deemed converged when two consecutive iterations for dimensionless velocity, temperature, and radiosity differed by less than 10^{-8}. A uniform grid size of 0.05 in the *X*-coordinate, 0.025 for the fluid domain and 0.01 for the solid domain in the *Y*-coordinate were selected which provided good compromise between accuracy and computational expense. As a sample calculation to verify grid independence, the maximum temperature and the average Nusselt number were computed for H=6 mm, L_1=5 mm, L_2=165 mm, Re=150, and k_s/k_f=9.5, and the change in both parameters was less than 1% when the number of grid points in the *X*-coordinate or *Y*-coordinate was doubled. In all computational cases, mass and energy conservation have been confirmed to be within 0.2%.

3.2.2 CFD Simulation

A commercial finite-volume-based computational fluid dynamics (CFD) code, FLUENT, was employed to simulate the vortex flow field and obtain pressure drop data for different VG geometries. Assuming incompressible, steady-state, laminar, Newtonian flow with constant properties, negligible viscous dissipation, pressure work and buoyancy effects, the conservation equations of mass, momentum and energy are written as

$$\frac{\partial}{\partial x_i}\left(\rho u_i\right) = 0 \tag{3.13}$$

$$\frac{\partial}{\partial x_i}\left(\rho u_i u_j\right) = \frac{\partial}{\partial x_i}\left(\mu \frac{\partial u_j}{\partial x_i}\right) - \frac{\partial p}{\partial x_j} \tag{3.14}$$

$$\frac{\partial}{\partial x_i}\left(\rho u_i T\right) = \frac{\partial}{\partial x_i}\left(\frac{k}{c_p}\frac{\partial T}{\partial x_i}\right) \tag{3.15}$$

Temperature and velocity profiles were uniform at the channel entrance and the outlet boundary condition was fully developed. No slip and adiabatic conditions were imposed on all solid surfaces except the bottom wall which is iso-flux. The computational

meshes were generated using Gambit software with a multi-block hybrid approach. A fully implicit second-order upwind scheme was used to discretize the governing equations. The momentum equations were first solved with an estimated pressure field. A pressure-velocity correction based on the SIMPLEC algorithm was then performed until the residuals of all governing equations were less than 10^{-8}.

3.3 Data Reduction

Two criteria are commonly used in the assessment of VG performance, one based on a fixed area (Tiggelbeck *et al*., 1993) and the other based on an affected area (Gentry and Jacobi, 2002). The former appears intuitive in which the selected area for data analysis remains constant. The width of the area must be large enough to incorporate all the spanwise effects of longitudinal vortices yet sufficiently small to avoid edge effects. The latter, on the other hand, recognizes the fact that different-sized VGs affect different heat transfer area. To enable comparison on an equal basis, the results are scaled to the affected span by partitioning the fin surface into enhanced and unenhanced regions. Facilitated by the full-field data acquisition feature of infrared thermography, this work adopted the affected-area-based criterion because it overcomes VG-size and area ambiguity and allows more general representation of enhancement. The affected width (ΔW) was determined from the spanwise Nusselt number (Nu) distributions (see later in Fig. 3.11). The local Nu is defined as

$$Nu = \frac{q_{conv} H}{(T_s - T_0) k_f} \tag{3.16}$$

where the convective flux, q_{conv}, is the total heating flux, q_{s}, less the conductive flux to the substrate, q_{cond}, and the radiation loss in the channel, q_{rad}

$$q_{conv} = q_s - q_{cond} - q_{rad} \tag{3.17}$$

The subsequent numerical investigation will show that conduction to the substrate can be neglected over the data analysis region. Also, due to a significant loss of radiant energy to ambient via the transparent sheet, temperature of the top wall does not rise appreciably (below 6 K). Evaluation of q_{rad} is then justified as exchange between a small unit at the local temperature and ambient, i.e.

$$q_{rad} = \varepsilon\sigma(T_s^4 - T_0^4) \tag{3.18}$$

Using a 95% confidence interval and the standard error-propagation method (Taylor and Kuyatt, 1994), the average uncertainties in *Re* and *Nu* were estimated to be 2.5% and 8.0%, respectively.

3.4 Results and Discussion

3.4.1 Baseline Data

3.4.1.1 Thermal Pattern in the Plain Channel. 2D and 3D false-color images of the steady-state temperature distribution of the heated surface at *Re*=340 are presented in Fig. 3.6. In order to avoid edge effects, only the central portion of the original image (102 pixels out of 160 in the *z*-direction) was taken for analysis. At a focal distance of 356 mm, the 102×248 pixel image corresponded to an area of 60×145 mm^2. Thus, each pixel represented a 0.59 mm^2 unit on the heated surface. Fig. 3.6 clearly illustrates the thermal development effects, with a gradual increase of surface temperature in the streamwise direction. The spanwise temperature variation has a maximum of ±0.8 $^{\circ}$C, indicating a highly 2D flow. A critical Rayleigh number of 1708 has been identified for the onset of 3D Bénard convection (Bergman *et al*., 2011). In the present experiments, the Rayleigh number never exceeded 1160; thus Poiseuille flow prevailed throughout the channel.

3.4.1.2 Span-Averaged Temperature Distribution. Measurements of the span-averaged temperature distribution across the heated surface are plotted in Fig. 3.7 and compared to numerical predictions by the conjugate model. The two results agree very well, particularly in the downstream region (x>30 mm). The differences fall into the experimental uncertainty range over the entire measured section. In prior relevant research (Bougeard, 2007; Yang, 2001), relatively large deviation between numerical and experimental results was also reported near the leading edge, associated with the difficulty of IR thermometry in measuring temperatures close to the ambient temperature (Yang, 2001). In addition, an uncooled microbolometer detector is recognized to be

insensitive as compared to a cooled one such that it might not capture the rapid temperature variation in the entrance region. Other possible sources for discrepancy include uncertainty in material properties, the diffuse-gray treatment of the radiant exchange, and modeling the channel inlet and outlet as black, isothermal apertures.

There is a somewhat striking systematic difference between the measured and computed temperatures. While the numerical predictions are monotonic in x, the experimental data exhibit a "wave-like" behavior. Such a behavior is almost certainly an experimental artifact, due to nonuniformity in the black paint which leads to unevenness in surface emissivity and thermal resistance. A numerical study performed on a 50 μm black paint layer by Mori *et al*. (2007) revealed that the shape of isotherms can be noticeably altered by the paint thermal conductivity. Again, it is worth noting that, although systematic, these differences are within the experimental uncertainty.

3.4.1.3 Temperature Field at Varying Reynolds Numbers. Predictions on the normalized temperature field, θ/θ_0, are shown in Fig. 3.8 at varying Reynolds numbers. A thinner thermal boundary layer on the floor is evident for higher Re, resulting in reduced surface temperatures and a strengthened role of convection. The maximum normalized temperature decreases from 1.061 at Re=340 to 1.046 at Re=940. The percentage of heat transfer by convection rises from 70% to 79% of the total input heat, and accordingly, the radiative flux is reduced from 30% to 21%. Temperature distributions across the substrate thickness are virtually constant except for in a limited region near the leading edge where heat conducted from downstream the substrate is conducted upward to the airflow. The numeric data show that q_{cond} contributes around 5% of the total flux between x=5 and 12 mm, and drops rapidly to less than 1% downstream. Note that the overall contribution by conduction (integral of q_{cond} along the entire floor) is zero, as the substrate is insulated on the exterior surfaces.

3.4.2 VG-Enhanced Channel Flow

3.4.2.1 Local Enhancement Characteristics. Thermal images of the steady-state temperature distributions on the heated surface at *Re*=340 are presented in Fig. 3.9 for various VG arrangements. Addition of VGs induces areas of increased and decreased heat transfer, resulting from the secondary flow toward and away from the surface, respectively. The thermal boundary layer is thinned by the downwash and thickened by the upwash. Gentry (1998) modeled the vortex motion as boundary layer suction and blowing. He proved that for the same magnitude of velocity, suction had a greater impact on heat transfer than blowing. Therefore despite the symmetry, the net effect of vortex interaction with the boundary layer is improved heat transfer.

Local *Nu* distributions are presented in Fig. 3.10 for multipair VGs at *Re*=570. By comparing Figs. 3.9b-3.9d to Fig. 3.10, it is evident that areas of increased and decreased heat transfer correspond to lowered and elevated temperature regions, respectively. The enhancement is most pronounced immediately after the VGs where the vortices are strongest and most coherent. Similar to the finding in the naphthalene sublimation experiment for laminar developing channel flow (Gentry and Jacobi, 2002), the trail of enhancement exhibits nearly parallel patterns.

Fig. 3.11 provides a sample evaluation of the affected width, where the spanwise *Nu* distributions at various streamwise locations are presented for the two-pair V-array at *Re*=940. The affected span in this case is estimated to be within (-18, 18) mm. For a V-formation array, the affected region expands with the number of winglet pairs. The conventional two-row pairs possess a smaller affected region than the two-pair V-array. It should be noted that determination of ΔW in this manner is assured by the fact that variation in ΔW by 20% leads to a maximum 3% change in the overall *Nu* for all investigated VG geometries.

3.4.2.2 Span-Averaged *Nu*. The affected-span-averaged *Nu* distributions for a single winglet pair are presented in Fig. 3.12 at varying *Re* and angles of attack. As expected, the existence of VGs hardly influences the flow upstream. The baseline *Nu*, by observation of Fig. 3.12a whose condition is closest to fully developed (the inverse

Graetz number being 0.03), approaches a value of approximately 1.9. Note that the fully developed *Nu* for a flat duct with one wall uniformly heated and the other maintained at constant temperature was reported to be 2.0 (Shah and Bhatti, 1987). The good agreement validates the experimental results to some extent. In accordance with the behavior shown in Fig. 3.10, the peak appears immediately after the winglets, with the one for 45º coming first and 15º coming last. The vortex strength increases with *Re*, and as the attack angle rises from 15º to 30º. Further augment of the angle to 45º might cause vortex breaking-down since the peak magnitude is seen to be highest at 30º. A maximum local enhancement of 57% occurs at *Re*=940 and β=30º. For the current channel geometry, 30º is considered an appropriate angle of attack and thus adopted in the deployment of multipair VGs.

The affected-span-averaged *Nu* distributions for multipair VGs at varying *Re* are presented in Fig. 3.13. The multiple peaks associated with the series of winglet pairs are clearly illustrated. For a V-formation array, the magnitude of each peak is fairly comparable. The lower peaks appearing in the three-pair array, though somewhat counterintuitive, are explicable by a larger affected span over which *Nu* is averaged. The conventional two-row pairs are less effective in two aspects. First, the second peak in this configuration is smaller than the preceding one throughout the *Re* range, indicating no boost effect by the trailing pair. Furthermore, the enhancement is noted to be significantly lower than the V-array along a large portion downstream the generators, which might suggest occurrence of destructive interference between vortices. A maximum local enhancement of 55%, very close to the value in the single-pair case, is found for the two-pair V-array, again at the highest *Re* of 940.

3.4.2.3 Overall Heat Transfer Enhancement. The overall heat transfer performance is evaluated in terms of *Nu* averaged over the affected area. Since the upstream influence is negligible, length of the affected area is taken from the winglet tip till the end of the measured section, i.e. *x*=17.9 to 150 mm. The enhancement ratio, defined as VG-enhanced *Nu* over the baseline *Nu*, is presented in Fig. 3.14 for the test VG geometries. The overall enhancement increases with *Re*, and as the attack angle rises from 15º to 30º. Under the affected-area-based criterion, the two-pair V-array yields 14-

32% augmentation in the total heat transfer for the current channel flow, as compared to 7-19% and 15-27% for the conventional two-row pairs and the three-pair V-array, respectively. Taking other factors such as manufacturing cost and spatial constraints into consideration, this study recommends the two-pair V-array deployed at 30º as an appropriate design for implementation in prototype plain-fin heat exchangers.

3.4.3 CFD Results

3.4.3.1 Vortex Flow Structure. To illustrate the evolving process of counter-rotating longitudinal vortices, cross-stream velocity vectors behind one-pair and two-pair V-formation arrays deployed at 30º are presented in Fig. 3.15. First of all, although decaying as advected by the main flow due to viscous dissipation, the vortex structure persists over a length of at least 10 times the VG height. The vortex cores exhibit a skewed, rather than circular, shape, which is validated by the dye visualization experiment (Leweke and Williamson, 1998). Using a method of images together with a potential flow model, Jacobi and Shah (1995) explained the skewing as a result of the interaction of the vortex with its image reflected in the wall. Such interaction mutually induces a spanwise velocity and causes the vortex to be skewed with respect to the main flow. The distance between the cores of the vortex pair gradually increases in the streamwise direction, which is also explicable by the method of images (Jacobi and Shah, 1995). For a counter-rotating pair, the vortices induce each other toward the wall. Upon approaching the surface, the vortex will eventually interact more strongly with the wall than with the other vortex, resulting in one vortex moving away from the other. The vortex intensity for the two-pair array is seen to be larger than that for the single pair at the same streamwise location.

3.4.3.2 Streamline Patterns. Streamline patterns for various VG arrangements at *Re*=340 are plotted in Fig. 3.16. The figures clearly show how the flow separates along the leading edge of the generators to form the longitudinal vortex system. For a multipair V-formation array (Figs. 3.16b and 3.16d), careful inspection reveals that the flow field

passing the trailing pairs is boosted, which, in contrast, is not so noticeable for the multirow pairs (Fig. 3.16c). The existence of affected and unaffected regions is also distinct, upholding the use of the affected-area-based criterion. Again, the trajectories of vortex pairs are seen to be nearly parallel.

3.4.3.3 Pressure Drop and Overall Performance. Another purpose of CFD simulation is to provide pressure drop data over the affected cross section along the entire channel. The values for the single pair, two-pair V-array, two-row pairs, and three-pair V-array at *Re*=340 are computed to be 0.449, 0.487, 0.475, and 0.512 Pa, respectively. The Colburn *j* factor and fanning friction faction for channel flow are expressed as

$$j = \frac{Nu_a}{\mathrm{Re}_{dh}\,\mathrm{Pr}_a^{1/3}} \tag{3.19}$$

$$f = \frac{\Delta P}{\rho u^2} \cdot \frac{H}{L} \tag{3.20}$$

Using an overall performance criterion of the modified London area goodness factor ($j/f^{1/3}$ *vs*. *Re*)† and assuming $j/f^{1/3}$ for the single pair to be unity (since only relative performance matters), the normalized $j/f^{1/3}$ for the two-pair V-array, two-row pairs, and three-pair V-array are found to be 1.012, 0.956, and 0.999, respectively. The two-pair V-array demonstrates the best overall performance among all investigated designs.

† Derivation and physical interpretation of the modified London area goodness factor are elaborated in section 4.3.4.

3.4.4 Appropriate Array Design

Based on the heat transfer and pressure drop performance and taking other factors such as manufacturing cost and spatial constraints into consideration, this study recommends the two-pair V-array deployed at 30º as an appropriate design for implementation in prototype plain-fin heat exchangers. Note that pressure drop across a heat exchanger is usually small relative to the overall loss in typical air-handling units and heat transfer behavior should weigh more in design evaluation. For example, Joardar and Jacobi (2008) reported an incremental fan power as little as 0.8 W when attaching three-row winglet pairs to a plain-fin-and-tube heat exchanger typically used for air-conditioning and refrigeration applications.

3.5 Figures

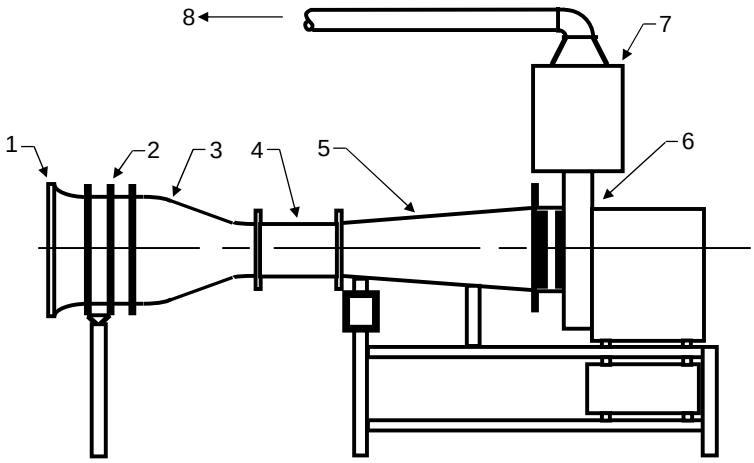

Figure 3.1 Schematic of the wind tunnel: 1) inlet, 2) flow conditioning, 3) contraction, 4) test section, 5) diffuser, 6) blower, 7) exit plenum, and 8) discharge to outside of lab (adopted from Gentry and Jacobi (2002) with modification).

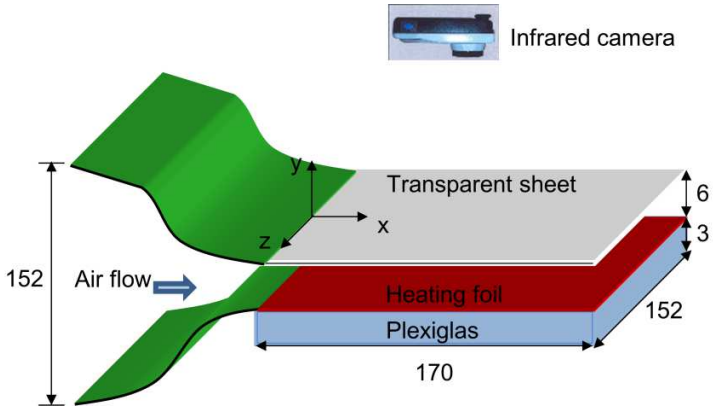

Figure 3.2 Diagram of the test section (all dimensions in millimeters); only the portion from x=5 to 150 mm is in the field of view of the infrared camera.

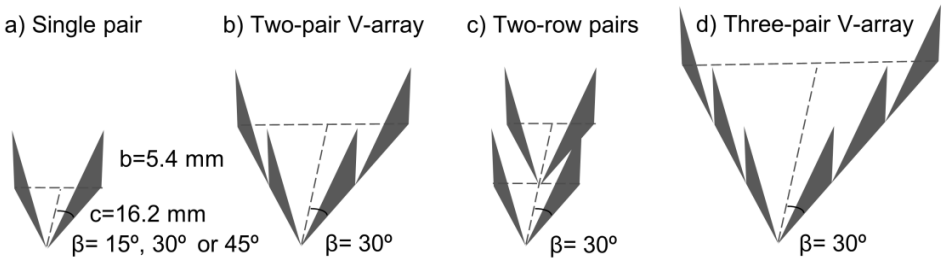

Figure 3.3 Test VG geometries.

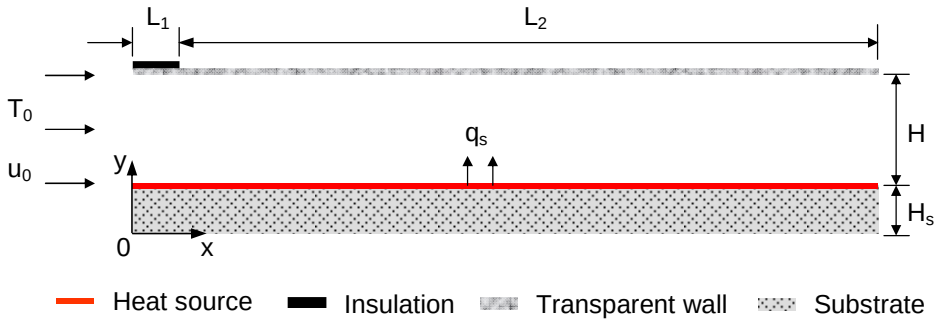

Figure 3.4 Computational model for the test section.

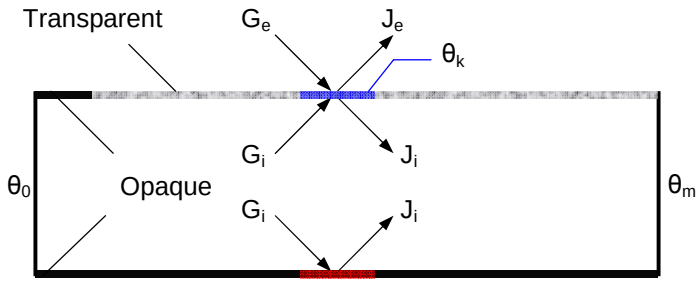

Figure 3.5 Radiative exchange in an enclosure with transparent and opaque surfaces.

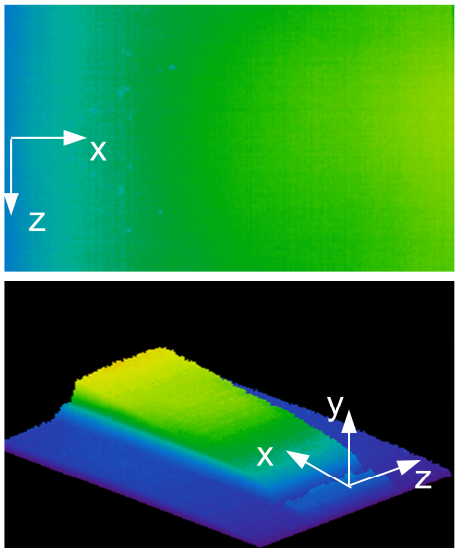

Figure 3.6 2D (top) and 3D (bottom) thermal images for the steady-state temperature distribution at *Re*=340.

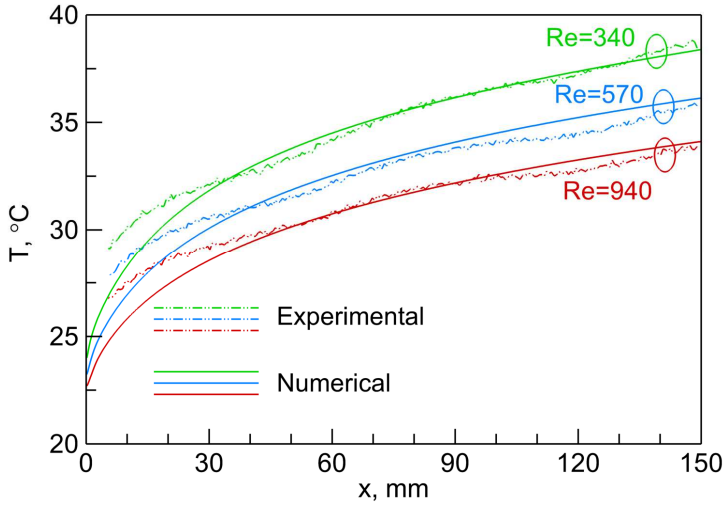

Figure 3.7 Comparison of the span-averaged temperature distribution on the heated surface between the experimental and numerical results.

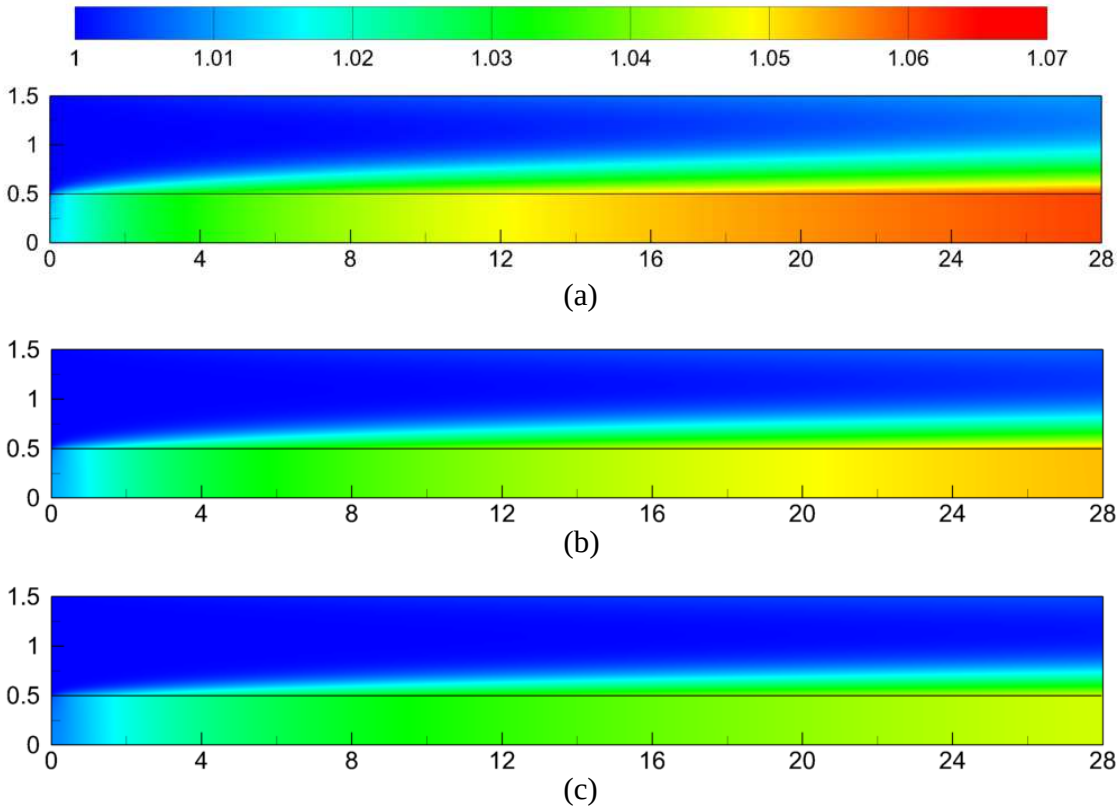

Figure 3.8 Normalized temperature field, θ/θ_0, at a) Re=340, b) Re=570, and c) Re=940. The black line in the graph represents the fluid-solid interface.

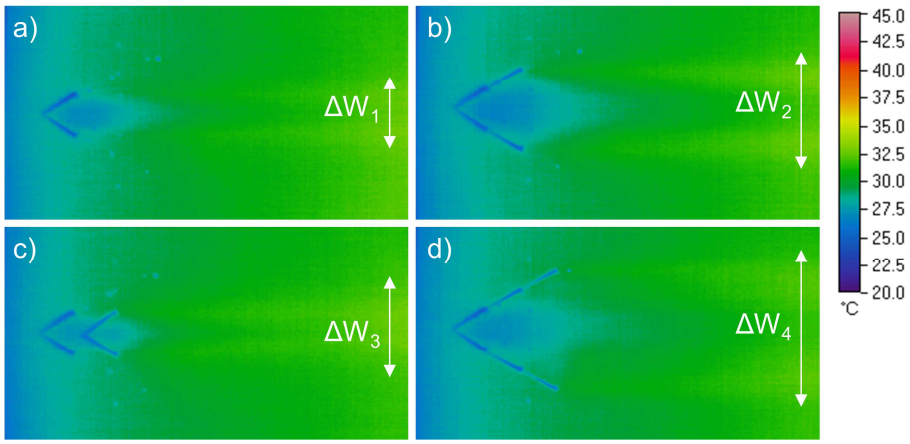

Figure 3.9 Thermal images of the steady-state temperature distribution at *Re*=340 for: a) single pair, b) two-pair V-array, c) two-row pairs, and d) three-pair V-array. ΔW_1 -ΔW_4 represent the affected width of VG-enhanced flows.

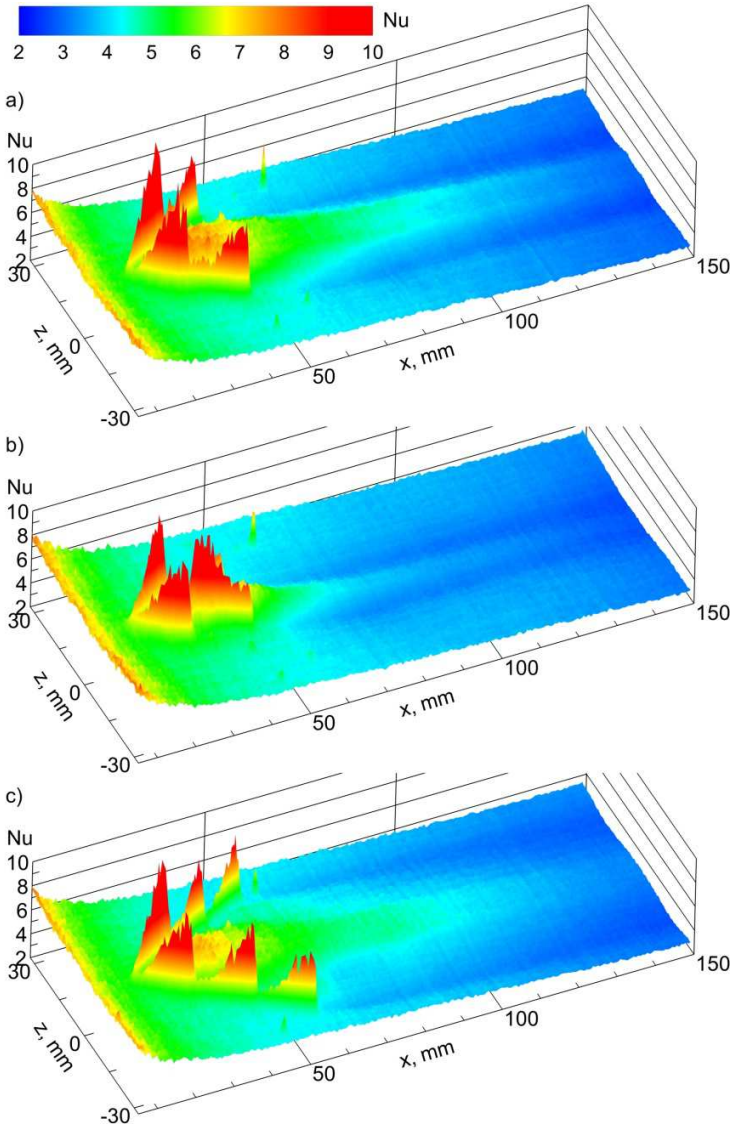

Figure 3.10 Local *Nu* distributions for a) two-pair V-array, b) two-row pairs, and c) three-pair V-array at *Re*=570.

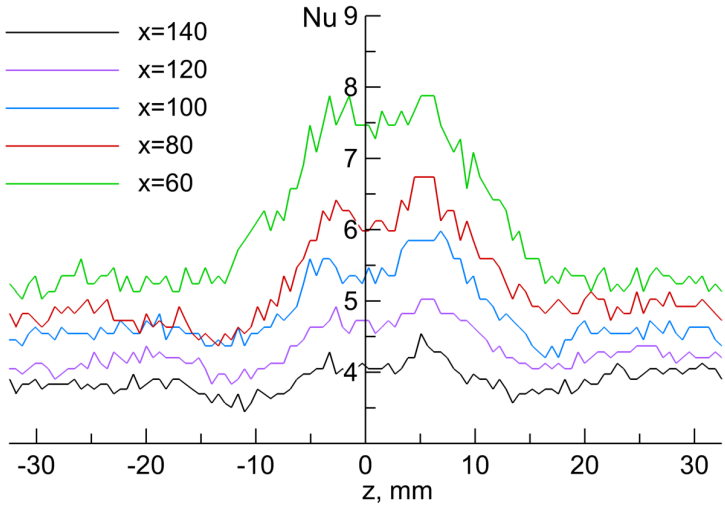

Figure 3.11 Spanwise *Nu* distributions for the two-pair V-array at *x*=60, 80, 100, 120, 140 mm and *Re*=940. The affected span in this case is estimated to be within (-18, 18) mm.

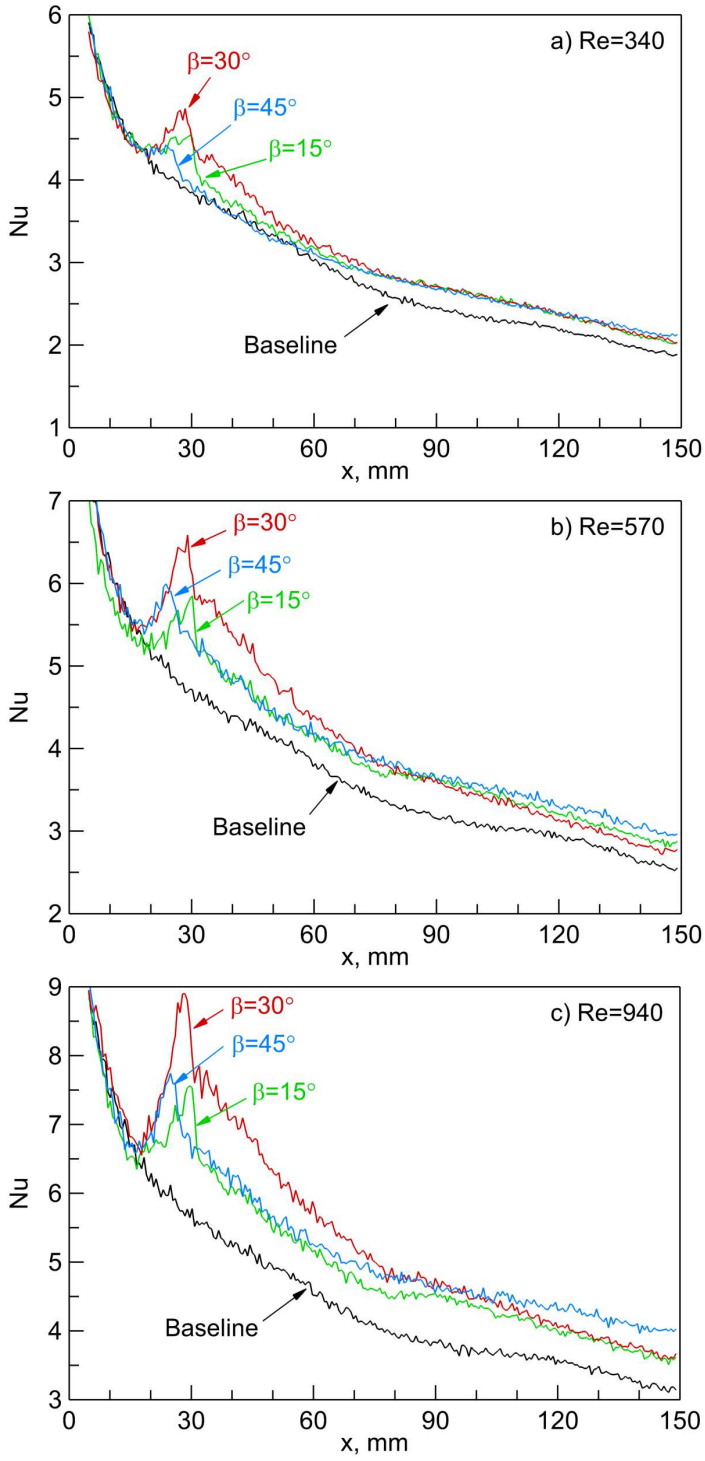

Figure 3.12 Affected-span-averaged *Nu* distributions for a single winglet pair at *Re*=340, 570, 940 and β=15º, 30º and 45º.

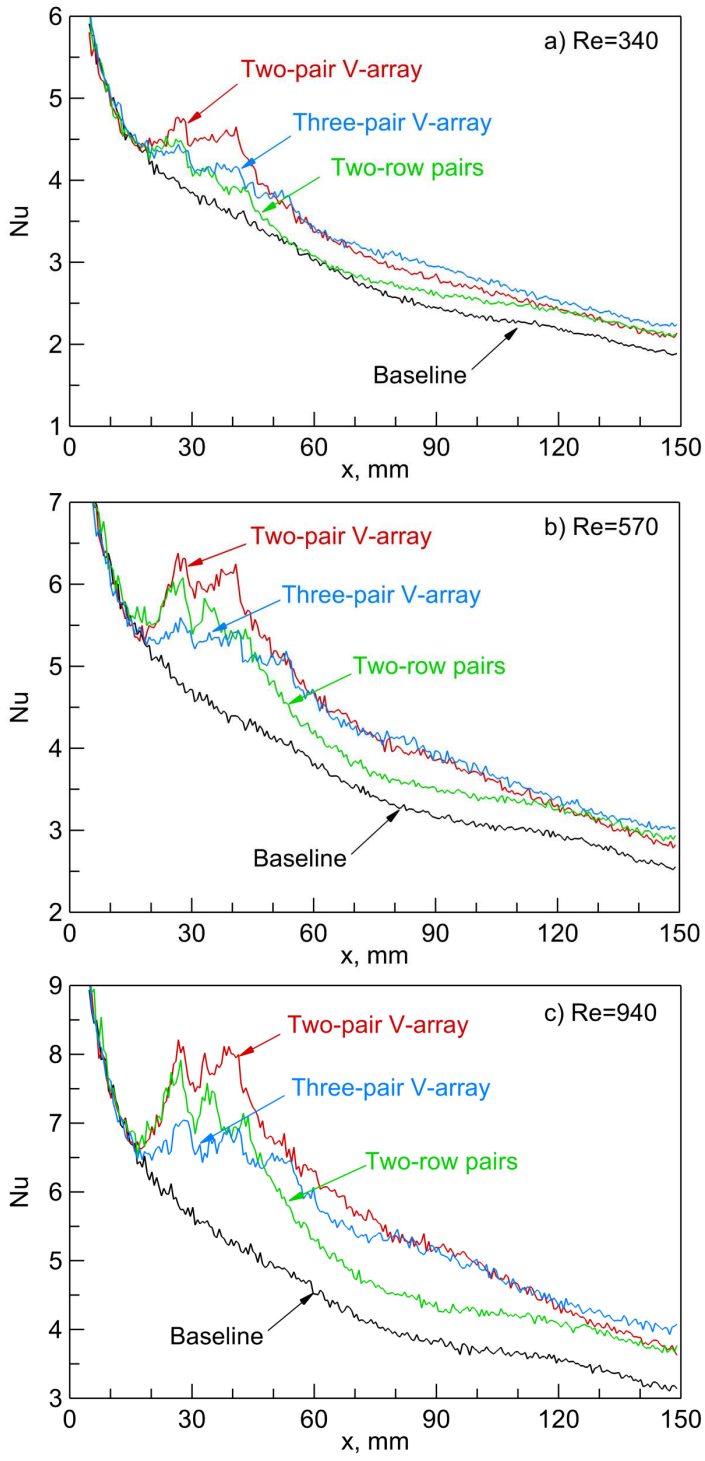

Figure 3.13 Affected-span-averaged *Nu* distributions for multipair VGs at *Re*=340, 570, 940 and β=30º.

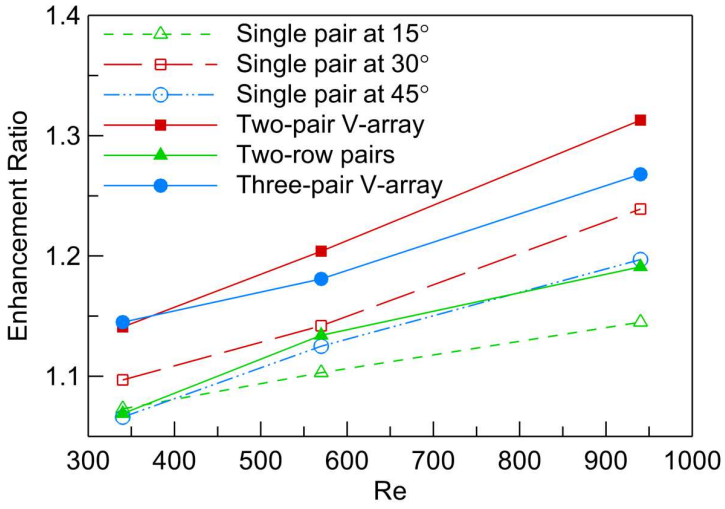

Figure 3.14 Enhancement ratio of the overall Nusselt number, $\overline{Nu} / \overline{Nu}_0$.

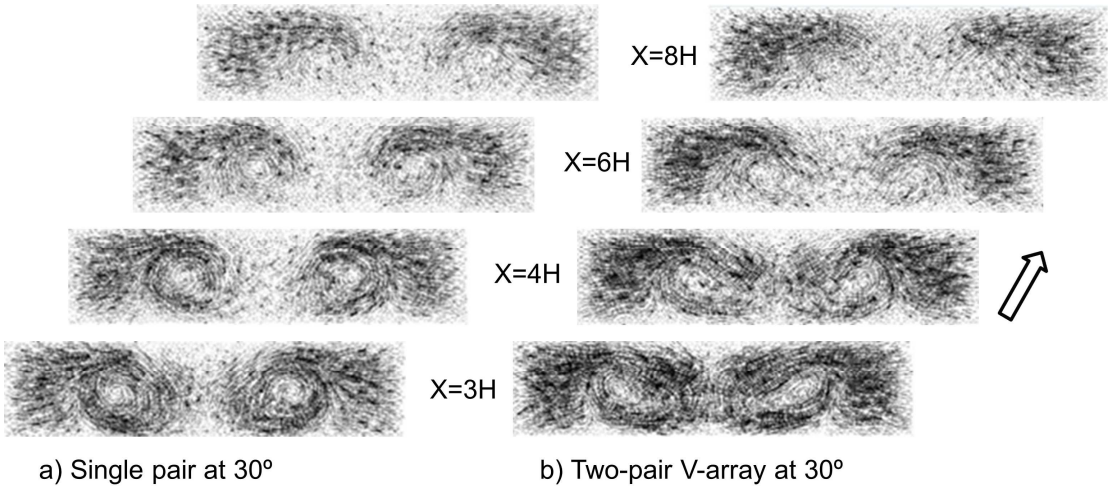

Figure 3.15 Cross-stream velocity vectors behind one-pair and two-pair V-formation arrays deployed at 30º.

a)

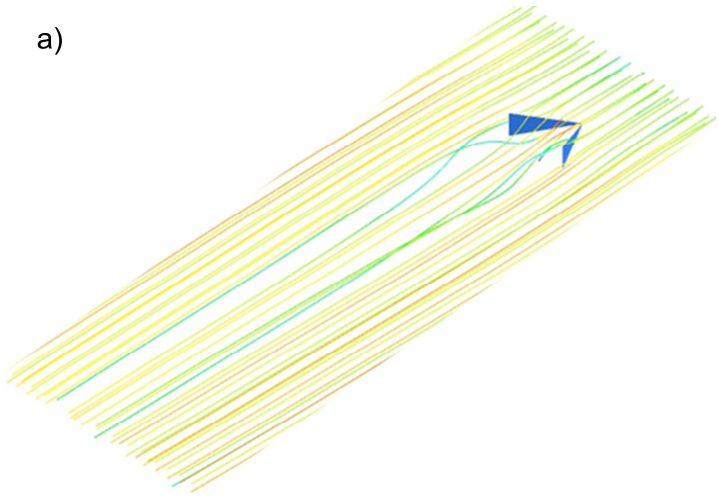

b)

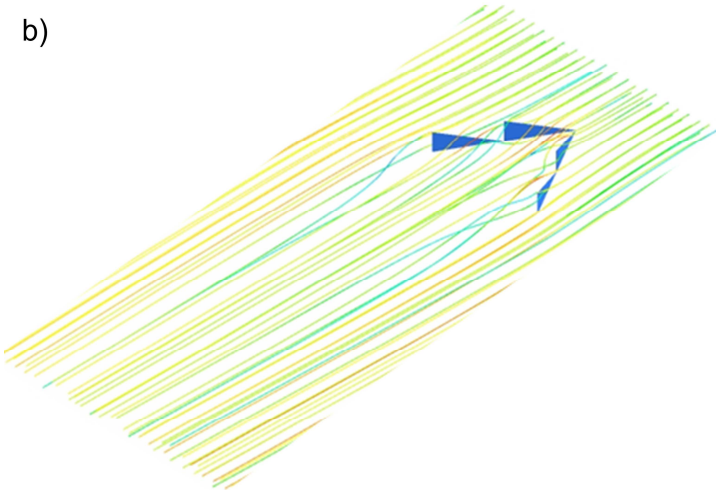

c)

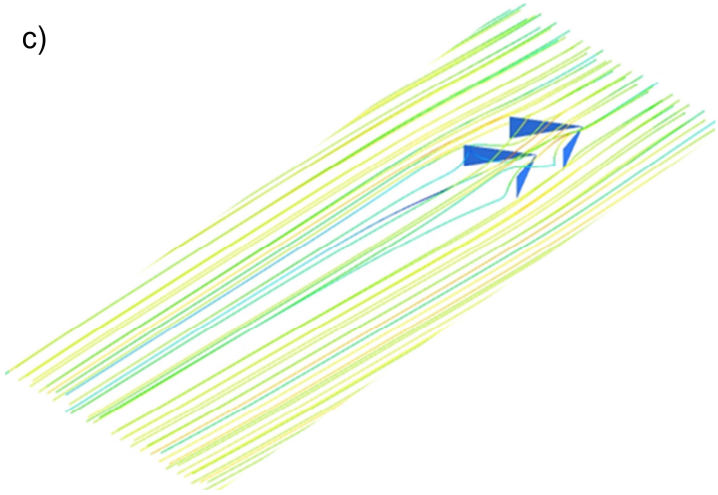

(Continued on next page)

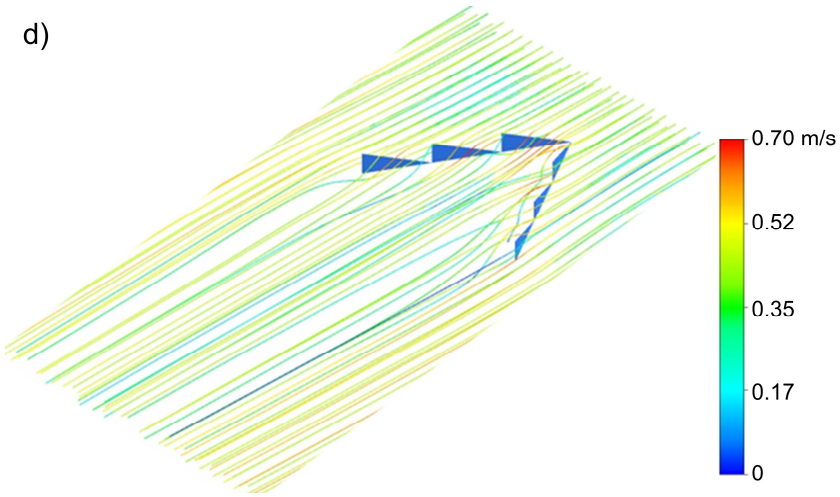

Figure 3.16 Streamline plots at *Re*=340 for: a) single pair, b) two-pair V-array, c) two-row pairs, and d) three-pair V-array.

CHAPTER 4

IMPLEMENTATION IN A PROTOTYPE PLAIN-FIN ROUND-TUBE HEAT EXCHANGER

To assess performance impact in application, the proposed V-array was implemented in a prototype plain-fin round-tube heat exchanger and tested in a full-scale wind tunnel under dry-surface conditions. In addition to 30º, another attack angle of 10º was also examined for the two-pair V-array. The baseline configuration without VGs and two conventional single-pair designs, all deployed at 30º, were included for comparison. The frontal air velocity ranged from 2.3 to 5.5 m/s, corresponding to a Reynolds number range based on the hydraulic diameter of 1400 to 3400. This work aims to provide new and more complete experimental data on VG-enhanced heat exchangers. Such data are useful to evaluate the true potential of the vortex-enhancement strategy and reports in this area are limited in extant literature.

4.1 Experimental Method

The baseline heat exchanger depicted in Fig. 4.1 has a collared fin-tube configuration with an inline tube arrangement. The fin spacing and thickness are 5.5 mm and 0.2 mm, respectively. The test VG geometries and their positioning on the fin surface are shown in Fig. 4.2. For each winglet, the height b=3 mm and the chord c=6 mm, which translates to an aspect ratio of 2. More winglet pairs and higher attack angles are prohibited by the geometric confinement of the current specimen. Two single-pair VGs placed at 30º are included for performance comparison. The small pair is identical to the leading pair of the V-array. The chord of the large pair is twice the length of the single pair; thus the large pair has the same winglet area as the V-array. The experiment started with the baseline heat exchanger. Then a total of 150 VGs (a V-array or either single pair referred as one VG), in an order of 10º V-array, 30º V-array, small pair, and large pair, were attached into the heat exchanger and tested respectively. Note that addition of these

VGs resulted in less than 1% increase in the air-side heat transfer area, so the enhancement can be predominantly ascribed to the generation of longitudinal vortices.

A closed-loop wind tunnel (Liu and Jacobi, 2009) as illustrated in Fig. 4.3 was used to measure the heat transfer and pressure drop performance of the heat exchangers. The air flow was driven by an axial blower and passed through resistance heaters (to condition the air temperature), a flow nozzle (to measure air mass flow rate), a mixing chamber, honeycomb flow straighteners, screens, and a 9:1 area contraction before it reached the test section. A mixture of ethylene glycol (54.6% volume concentration) and water was supplied by a gear pump to cool the heat exchanger during the experiments. The coolant temperature was controlled using a chiller system, and a Coriolis-effect flow meter was used to measure its mass flow rate. A six-junction, equally spaced thermocouple grid (±0.1ºC) and another twelve-junction grid were used to detect the air temperatures at the inlet and downstream of the specimen, respectively. Immersion RTDs (±0.03ºC) were positioned at the inlet and exit of the heat exchanger to record the coolant inlet and exit temperature. Air-side pressure drop across the heat exchanger was acquired with an electronic pressure transducer (±0.2Pa).

The experimental conditions are provided in Table 4.1. Low relative humidity air and high-temperature coolant were introduced to ensure no condensation on the air-side surface. An experiment was initiated by circulating the airflow while bringing it to the desired temperature and frontal velocity. The coolant flow preconditioned to the desired temperature was then brought in to cool the heat exchanger. After a brief transient period of around 15 minutes, a steady state was considered to prevail when all temperatures varied by less than the experimental uncertainty for at least three minutes. Data were sampled using LabView at a rate of 1.0 Hz and averaged for post analysis.

4.2 Data Reduction

The sampled temperature and flow-rate data are first used to determine the air-side heat transfer coefficient. For the air and coolant flow, the heat transfer rates at each side are calculated based on the mass flow rate and temperature change

$$Q_a = \dot{m}_a c_{p,a} \left(T_{a,i} - T_{a,o} \right) \tag{4.1a}$$

$$Q_c = \dot{m}_c c_{p,c} \left(T_{c,o} - T_{c,i} \right) \tag{4.1b}$$

The log-mean-temperature-difference (LMTD) method is employed to analyze the heat transfer performance

$$UA_{tot} = \frac{Q_{ave}}{F \cdot LMTD} \tag{4.2}$$

U is the overall heat transfer coefficient and A_{tot} denotes the total air-side heat transfer area (fin and tube). LMTD for counter flow is given by

$$LMTD = \frac{\left(T_{a,i} - T_{c,o} \right) - \left(T_{a,o} - T_{c,i} \right)}{\ln\left(\frac{T_{a,i} - T_{c,o}}{T_{a,o} - T_{c,i}} \right)} \tag{4.3}$$

and the correction factor F is very close to unity under the current operating conditions. For the purpose of combined uncertainty minimization (Park *et al*., 2010), Q_{ave} is estimated as the weighted average of the air-side and coolant-side heat transfer rates

$$Q_{ave} = \omega_a Q_a + \omega_c Q_c \tag{4.4a}$$

where ω_a and ω_c are the weighting factors that depend on the uncertainties in the heat transfer rates of the air side, ξ_a, and of the coolant side, ξ_c

$$\omega_a = \frac{1/\xi_a^2}{1/\xi_a^2 + 1/\xi_c^2}; \quad \omega_c = \frac{1/\xi_c^2}{1/\xi_a^2 + 1/\xi_c^2} \tag{4.4b}$$

For all the presented data, the relative discrepancy between the air and coolant heat transfer rates, $|Q_a - Q_c|/Q_{ave}$, had an average value of 5% or less.

Neglecting the fouling and contact resistance, the overall thermal conductance (UA_{tot}) of the heat exchanger can be expressed as

$$UA_{tot} = \left(R_c + R_{cond} + R_a \right)^{-1} \tag{4.5}$$

where R_c, R_{cond}, R_a are the coolant-side convective resistance, tube wall conduction resistance, and air-side heat transfer resistance, respectively

$$R_c = \frac{D_i}{Nu_c k_c A_c} \tag{4.6}$$

$$R_{cond} = \frac{\ln\left(\frac{D_o}{D_i}\right) \cdot D_i}{2k_{Cu}A_c} \tag{4.7}$$

$$R_a = \frac{1}{\eta_0 h_a A_{tot}} \tag{4.8}$$

R_{cond} for the test heat exchanger was found to be less than 0.1% of the total resistance. Conduction resistance of the soldered collar was also negligible.

Because the coolant flow was divided into six circuits, the tube-side Reynolds number was always below 1000. Therefore, laminar flow prevailed and the following correlations (Bergman *et al*., 2011) were adopted to evaluate the coolant-side convective *Nu*

$$Nu_c = 1.86 \cdot \left(\frac{\mathrm{Re}_D \,\mathrm{Pr}_c}{L/D_i}\right)^{1/3} \cdot \left(\frac{\mu}{\mu_w}\right)^{0.14} \tag{4.9a}$$

for combined entry length, and

$$Nu_c = 3.66 + \frac{0.0668(D_i/L)\,\mathrm{Re}_D\,\mathrm{Pr}_c}{1+0.04[(D_i/L)\,\mathrm{Re}_D\,\mathrm{Pr}_c]^{2/3}} \tag{4.9b}$$

for thermal entry length, where μ and μ_w are the coolant dynamic viscosity evaluated at the average fluid temperature and wall temperature, respectively. Eq. (9a) was applied for the portion of the tube over which simultaneous hydrodynamic and thermal development occurred and Eq. (9b) for the rest of the tube. The final Nu_c plugged into Eq. (4.6) was the weighted average. Thermophysical properties of the coolant were calculated using the manufacturer's correlations, based on the measured coolant temperature and specific gravity.

The air-side resistance, R_a, in Eq. (4.8), is a combination of the resistance due to air-side convection from the tube and the fin surface. η_o is the overall surface efficiency defined as

$$\eta_o = 1 - \left(\frac{A_{fin}}{A_{tot}}\right) \cdot \left(1 - \eta_f\right) \tag{4.10}$$

The fin efficiency, η_f, is determined using the modified equations for plane fins, as suggested by Wang *et al*. (2000)

$$\eta_f = \frac{\tanh(mr\phi)}{mr\phi} \tag{4.11a}$$

$$m = \sqrt{\frac{2h_a}{k_f \delta_f}} \tag{4.11b}$$

$$\phi = \left(\frac{R_{eq}}{r} - 1\right) \cdot \left[1 + 0.35 \ln\left(\frac{R_{eq}}{r}\right)\right] \tag{4.11c}$$

For inline tube layout,

$$\frac{R_{eq}}{r} = 1.28 \cdot \frac{X_M}{r} \cdot \left(\frac{X_L}{X_M} - 0.2\right)^{1/2} \tag{4.11d}$$

Eqs. (4.1-4.11) were programmed using commercial software Engineering Equation Solver (EES) to determine the air-side heat transfer coefficient h_a in an iterative manner.

Data interpretation followed the methods by the ARI Standard for fin-and-tube heat exchangers. Given the results of h_a, the Colburn j-factor is obtained from

$$j = \frac{Nu_a}{\mathrm{Re}_{dh}\,\mathrm{Pr}_a^{1/3}} = \frac{h_a}{Gc_{p,a}} \cdot \mathrm{Pr}_a^{2/3} \tag{4.12}$$

where the mass flux $G = \dot{m}_a / A_{\min}$ corresponds to the minimum free flow area. All the fluid properties were evaluated at the average values of inlet and outlet temperatures under the steady-state conditions. The fanning friction factor of the heat exchanger, f, is calculated as (excluding the negligible entrance and exit losses)

$$f = \frac{2\Delta P \rho_a}{G^2} \cdot \left(\frac{A_{\min}}{A_{tot}}\right) - \left(1 + \sigma^2\right) \cdot \left(\frac{\rho_{up}}{\rho_{down}} - 1\right) \cdot \left(\frac{A_{\min}}{A_{tot}}\right) \cdot \left(\frac{\rho_a}{\rho_{up}}\right) \tag{4.13a}$$

with

$$\sigma = \frac{A_{\min}}{A_{front}} \tag{4.13b}$$

and

$$\rho_a = \frac{\rho_{up} + \rho_{down}}{2} \tag{4.13c}$$

Two evaluation criteria were employed to assess the overall performance of the heat exchanger with and without VGs, i.e. the modified London area goodness factor

($j/f^{1/3}$ *vs. Re*) and the volume goodness factor (heat transfer coefficient *vs.* pumping power per unit heat transfer area). The pumping power, *PW*, required in the system is proportional to the core pressure drop across the heat exchanger

$$PW = \frac{\dot{m}_a \Delta P}{\rho_a} \tag{4.14}$$

Estimation of the uncertainties for all the calculated quantities followed the error-propagation methodology described in NIST Technical Note 1297 (1994), also utilizing the EES software.

4.3 Results and Discussion

4.3.1 Air-Side Thermal Performance

Enhanced thermal performance of the heat exchanger after attaching the VGs is compared to the baseline performance in Fig. 4.4, where the air-side heat transfer coefficient, h_a, and the thermal resistance, R_a, versus the frontal air velocity, are presented. The uncertainty in all figures is hereafter provided at representative points only for better readability. Using a 95% confidence interval and standard error-propagation analysis, the average uncertainties in h_a and R_a over the entire air velocity range were estimated to be 9.1% and 8.2%, respectively. The 10º VG array induces essentially no thermal improvement, as the differences in h_a and R_a from the baseline results are well within the experimental uncertainties. Such behavior indicates the ineffectiveness of the vortex-generation method at a relatively small attack angle due to the weak vortices produced. The small pair brings about a moderate heat transfer augmentation of up to 32%. In contrast, both the 30º array and the large pair yield a 25-55% increase in the heat transfer coefficient, and concurrently, a 22-35% reduction in the thermal resistance over the experimental range. The similar heat transfer performance is consistent with established understanding of VG enhancement: because of the same height, chord length and attack angle, the vortex strength and affected areas for the two designs are expected to be close. The maximum enhancement is seen to occur in the low velocity region. Through enhancing bulk mixing, modifying the boundary layer, and potentially causing flow

destabilization, the vortices result in a net effect of decreased air-side thermal resistance (and increased convective heat transfer coefficient). The first two mechanisms are simply induced by the swirl and downwash motion of longitudinal vortices. Evidence for the third mechanism was provided in an experimental study (Fiebig, 1995) which showed that the turbulence level increased from 0.8% of the incoming flow to above 10% four channel heights downstream of the winglet tips for Re>2200 in a developing channel flow.

4.3.2 Core Pressure Drop

The core pressure drop ΔP across the heat exchanger is presented in Fig. 4.5. The uncertainty in measured ΔP never exceeded 1.5% over the entire experimental range and thus is not shown in the plot. The pressure drop increases monotonically with the frontal air velocity, and the deviation from the baseline data after the addition of VGs becomes progressively more apparent for increasing velocities. This behavior confirms that the extra pressure loss associated with the use of VGs is predominately due to the form drag, which is proportional to the velocity square. The 10º array and the small pair exhibit similar additional pressure drop of 20-40%. By comparison, the 30º array causes a relatively severe pressure drop penalty of 80-110%. Nevertheless, the magnitude is still 40% lower than that of the large pair, even though the designs have the same attack angle and projected area. With reference to the streamlines in the wake behind a single pair and two-pair array as shown in Figs. 3.16a and 3.16b, it is revealed that if a trailing pair is placed downstream in a "V", the generated vortices by the leading pair will transport high-momentum fluid towards the fin surface behind the trailing pair, thus narrowing the wake zone and mitigating the pressure difference. The vortex strength produced by the trailing pair is accordingly diminished. However, based on the heat transfer results, this undesired effect may have been compensated by the simultaneously improved heat transfer in the wake, without impairing the overall thermal performance.

Note that the magnitude of extra pressure loss for the 30º array and the large pair is considerably larger than that reported by Joardar and Jacobi (2008) (26-88% for delta-winglet pairs deployed in three rows). In addition to a higher Reynolds number range

(1400-3400 *vs.* 220-960), a larger attack angle (30º *vs.* 15º) and a smaller flow depth (51 mm *vs.* 178 mm) in this work, another cause could be the difference in the VG location relative to the tubes. The current array was placed at the leading edge mainly due to the short flow passage of the test heat exchanger; whereas, a further downstream placement was adopted by Joardar and Jacobi (2008) to take advantage of tube-wake management. In particular cases (Torii *et al*., 2002; Wu and Tao, 2007), if the VGs are carefully designed and oriented such that reduction in the tube form drag outweighs the drag introduced by the VGs themselves, it is even possible to reduce the pressure drop as compared to the smooth heat exchanger. However, such a favorable configuration, if it exists, is definitely case dependent. Its determination is complicated by the numerous design parameters for a specific heat exchanger and VG type. The concern about the pressure drop penalty in the presence of VGs may be alleviated by noting that the additional pressure drop is small relative to the overall losses in typical air-handling equipment for most HVAC&R systems. In point of fact, the incremental fan power required to overcome the pressure drop penalty for the 30º array was always below 5.0 W (calculated from Eq. (4.14)).

4.3.3 j and f Factors

The conventional representation of thermal-hydraulic performance in terms of the Colburn *j*-factor and *f*-factor is presented in Fig. 4.6, where similar enhancement characteristics as shown in h_a and ΔP are observed. The average increase in *j*-factor is roughly 15% for the small pair, and 45% for the large pair and the 30º array. The latter two designs achieve heat transfer augmentation far beyond the experimental uncertainty of 9.2% in *j*-factor. The heat transfer improvement is at the cost of a 25% increase in *f*-factor for the small pair, 90% for the 30º array and as high as 140% for the large pair. The uncertainty in *f*-factor is about 4.0%.

4.3.4 Overall Performance Evaluation

The overall performance of VG-enhanced heat exchangers is evaluated using the modified London area goodness factor ($j/f^{1/3}$ *vs*. *Re*) and compared to the baseline heat exchanger in Fig. 4.7a. Nearly all the data for the 10º array fall below the baseline points due to a similar heat transfer performance and a larger pressure drop - the heat exchanger performance is degraded. Results for the pair designs (small and large) are seen to be close for $Re \gtrsim 2000$. Both yield mild enhancement within the experimental uncertainty (9.1%). In contrast, the 30º array increases $j/f^{1/3}$ by approximately 15-25% and demonstrates the best performance among all VG designs considered. The improvement is more prominent at low Reynolds numbers. By neglecting the density variation of air between upstream and downstream of the heat exchanger in Eq. (4.13a), and combining Eqs. (4.12), (4.13a) and (4.14) with the elimination of the mass flux *G*, a relation in the following form results (see also Webb and Kim, 2005)

$$\frac{\dfrac{j}{f^{1/3}}}{\left(\dfrac{j}{f^{1/3}}\right)_0} = \frac{\dfrac{hA_{tot}}{(hA_{tot})_0}}{\left(\dfrac{PW}{PW_0}\right)^{1/3} \cdot \left(\dfrac{A_{tot}}{A_{tot,0}}\right)^{2/3}} \tag{4.15}$$

where the subscript "0" refers to the baseline quantities. Since the air-side resistance is the dominant part in Eq. (4.5), Eq. (4.15) may be approximated as

$$\frac{\dfrac{j}{f^{1/3}}}{\left(\dfrac{j}{f^{1/3}}\right)_0} \simeq \frac{\dfrac{Q}{Q_0}}{\left(\dfrac{PW}{PW_0}\right)^{1/3} \cdot \left(\dfrac{A_{tot}}{A_{tot,0}}\right)^{2/3} \cdot \dfrac{LMTD}{LMTD_0}} \tag{4.16}$$

Significance of the enhancement in $j/f^{1/3}$ is then elucidated. By selecting one of the operational variables in the RHS of Eq. (4.16) as the desired objective subject to design constraints on the remaining variables, any of the four kinds of performance improvements as described by Webb and Kim (2005) can be realized. From the viewpoint of "area goodness", the enhanced heat exchanger would require a smaller heat transfer area to accomplish a given heat duty at the fixed pumping power if LMTD maintains constant. For the 30º array case, specifically, the average enhancement ratio of 1.21 was calculated to bring about 25% reduction in A_{tot}. As a result, the heat exchanger

can be manufactured with less material, which allows more compactness and hopefully reduces cost. The size reduction also means a smaller volume of refrigerant to be used. This reduction could be a significant saving in the manufacture of refrigeration equipment.

Another commonly used evaluation criterion is the volume goodness factor, i.e. the air-side heat transfer coefficient versus the pumping power per unit heat transfer area. Comparison among the five configurations in terms of the volume goodness factor is presented in Fig. 4.7b, where the 30º array exhibits the highest performance again. A higher volume goodness factor for a given heat exchanger may be interpreted as either larger heat duty under the operation of fixed pumping power or smaller pumping power required to fulfill fixed heat duty. The former enhancement can also be considered as reduction of the condensing pressure in a vapor-compression machine, with attendant compressor power savings. The latter enhancement can be considered as a direct savings of fan power, although as pointed out earlier, core pressure drop is typically not large relative to the overall air-handling losses.

4.4 Figures and Tables

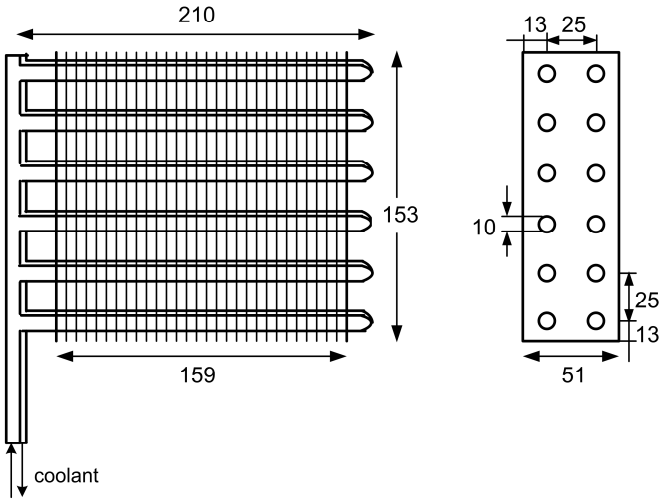

Figure 4.1 Schematic of heat exchanger configuration; all dimensions in millimeters.

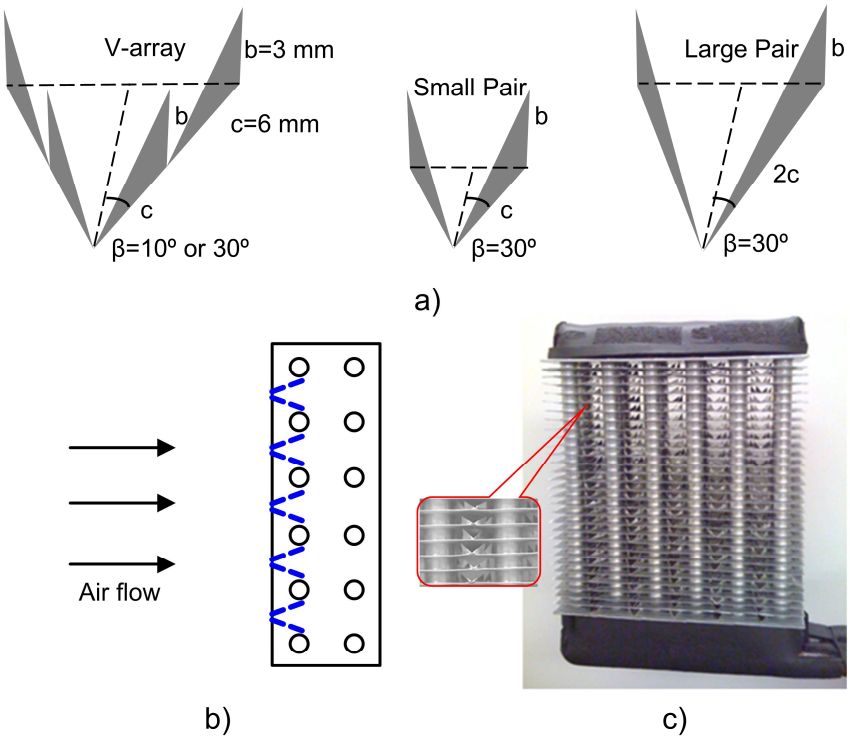

Figure 4.2 a) Geometry of the test V-array and single pairs; b) cross-sectional view and c) photograph of the heat exchanger with attached VGs at the leading edge.

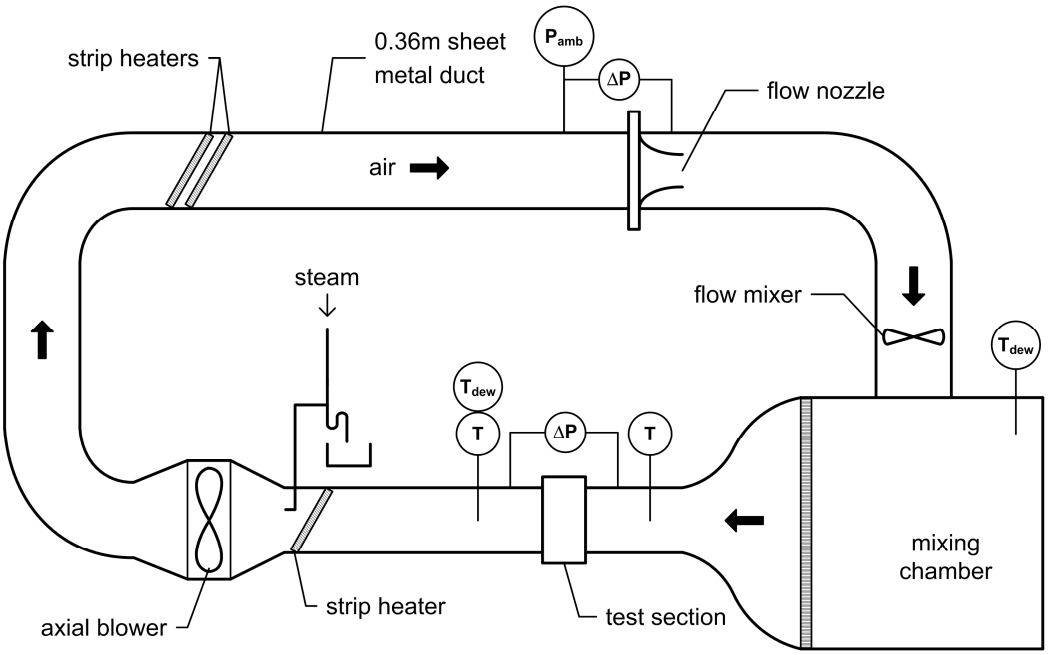

Figure 4.3 Schematic of the wind tunnel (adapted from Liu and Jacobi, 2009).

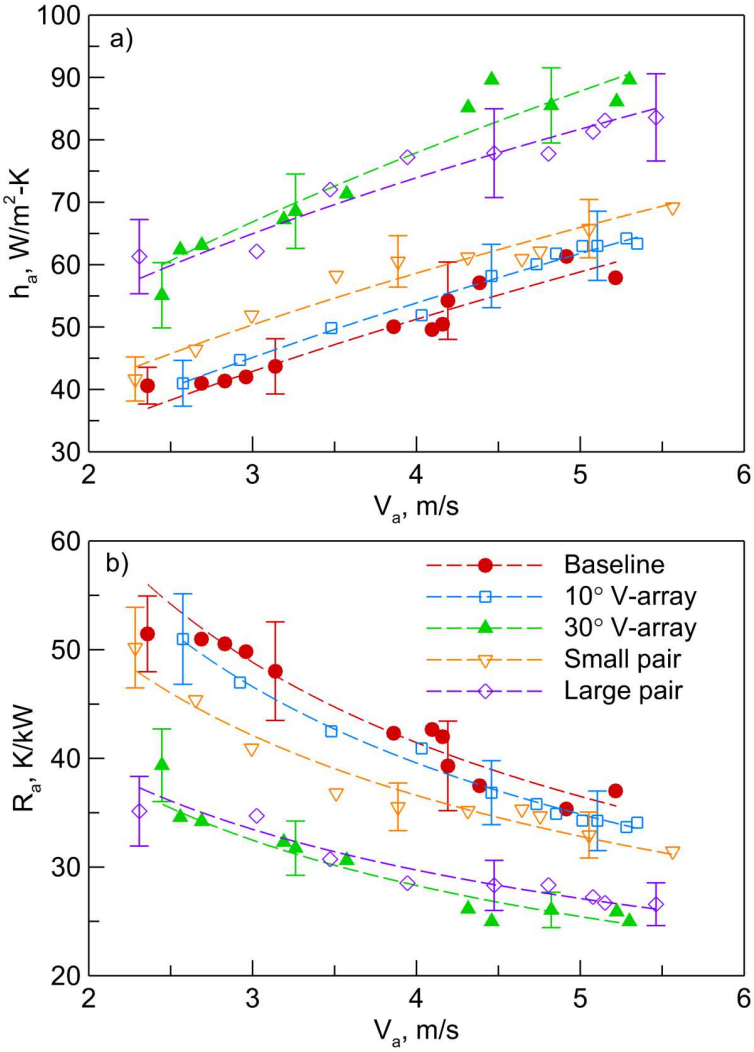

Figure 4.4 Baseline and VG-enhanced thermal performance as a function of frontal air velocity: a) air-side heat transfer coefficient and b) air-side thermal resistance. Curve-fitting is used for enhancing readability only.

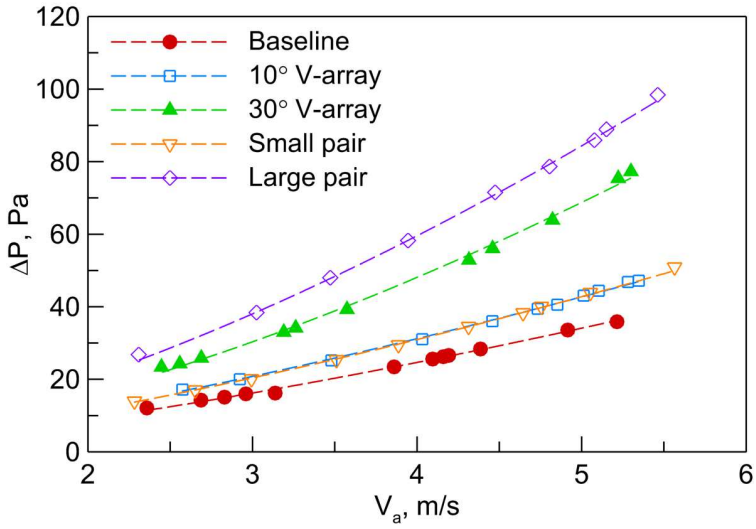

Figure 4.5 Core pressure drop across the heat exchanger. Curve-fitting is used for enhancing readability only.

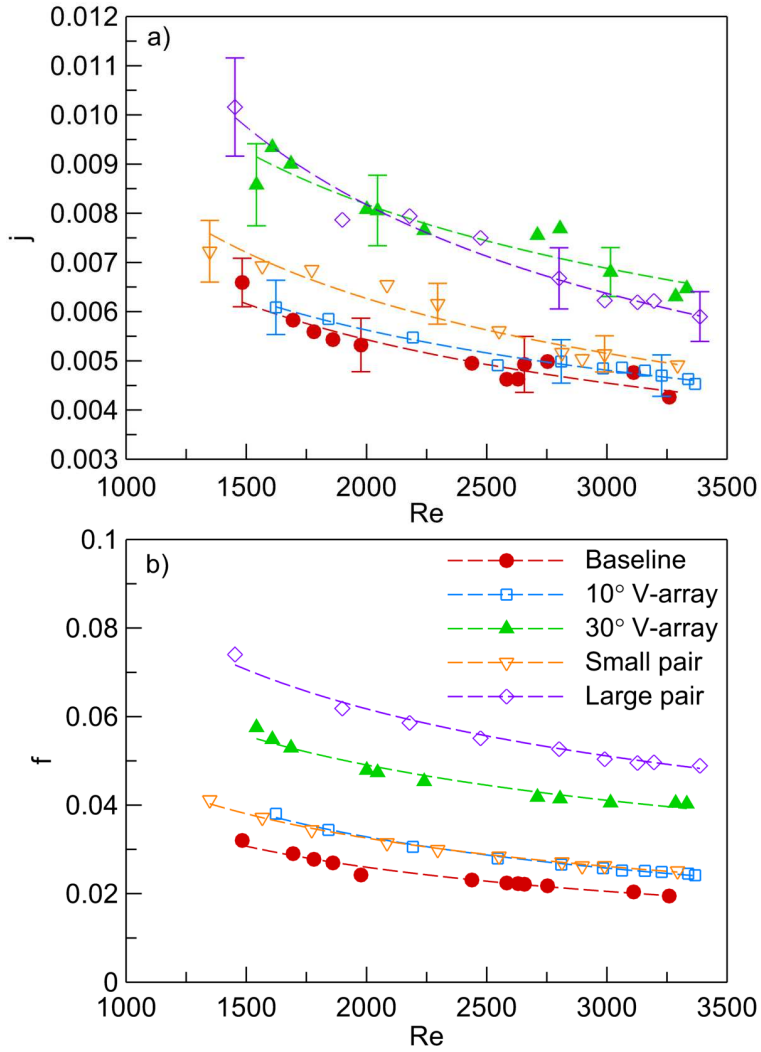

Figure 4.6 a) Colburn *j*-factor and b) fanning friction factor versus air-side Reynolds number. Curve-fitting is used for enhancing readability only.

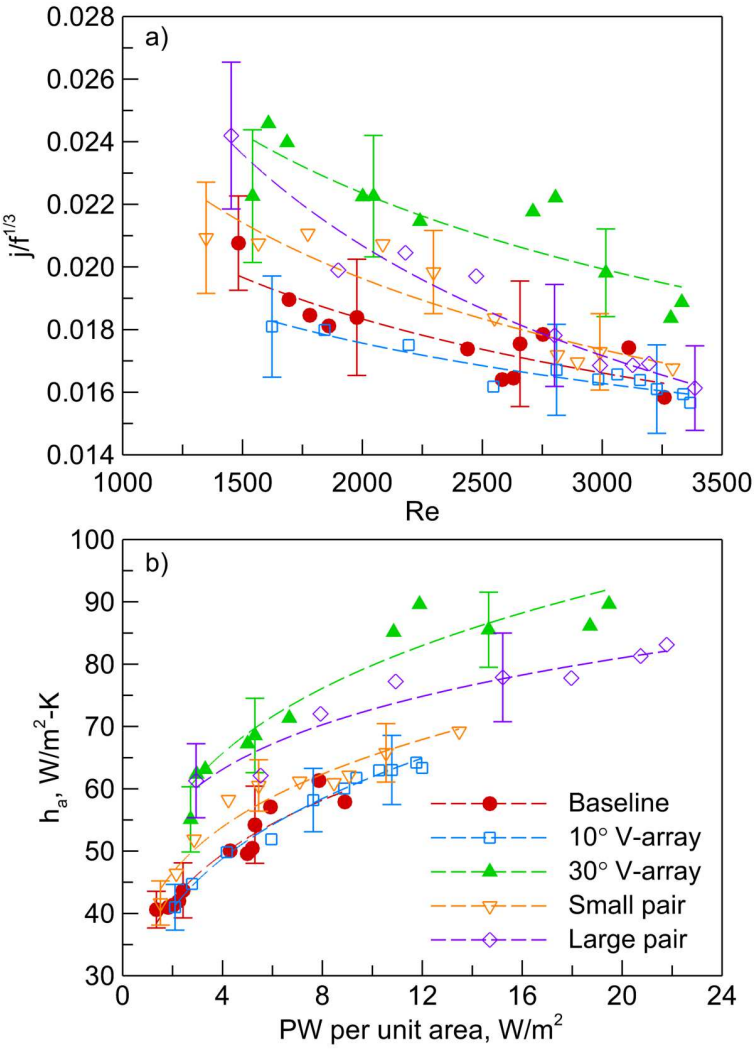

Figure 4.7 Overall performance evaluation criteria: a) modified London area goodness factor versus air-side Reynolds number and b) volume goodness factor, i.e. air-side heat transfer coefficient versus pumping power per unit heat transfer area. Curve-fitting is used for enhancing readability only.

Table 4.1 Test conditions

		Dry operation
Air	Inlet dry bulb temperature (ºC)	23.9
	Inlet relative humidity	32%
	Frontal air velocity (m/s)	2.3~5.5
Coolant	Inlet temperature (ºC)	8.9
	Flow rate (kg/h)	196~492

CHAPTER 5

CONCLUSIONS

5.1 Summary of Results

This work was motivated by existing challenges in the design of VG-enhanced heat exchangers. First of all, strong vortices are required at low-*Re* applications as encountered in compact configuration and/or low frontal air velocities. Secondly, an optimal array spacing needs to be identified that allows vortices to affect as much area as possible while avoiding destructive interference between them. Suggested from group movement of migrating birds, a new vortex-generator array deployed in a "V" was proposed, aiming to utilize favorable interaction between vortices and surmount the challenges. A series of investigations, both experimental and numerical, have been undertaken to demonstrate the existence of constructive interference, to develop a design guideline and propose an appropriate array, and finally, to quantify performance impact in a scale model and a prototype plain-fin heat exchanger.

- *Vortex Measurement – A Preliminary Screening*. The investigation started with vortex measurement in a water tunnel using ink visualization and a vane-type vortex meter, due to its ease of implementation and reasonable accuracy. By measuring the circulation rate downstream V-arrays with and without spacing between winglets and an offset deployment, it showed that the V-formation array was superior in that it produced stronger vortices. Vortex strength of V-array decreased with spacing between winglets. For the zero-spacing V-array, the boost effect was manifest at a winglet number of two. Addition of a third winglet, however, did not further accelerate the circulation. The strongest vortex was measured for the two-row zero-spacing V-array deployed at 30º. This part of work provided qualitative evidence of favorable interaction by grouping winglets in a "V". It also served as a preliminary screening of potential optimal geometries.

- *Heat Transfer Measurement – Further Refinement.* To refine the design obtained from vortex measurement and quantify heat transfer behavior, the impact of V-formation arrays was experimentally assessed in a developing channel flow using infrared thermography and compared to a conventional multirow configuration. A rectangular channel of 6 mm high and 152 mm wide was built to simulate a single passage of plain-fin heat exchangers, with an opaque, uniformly heated wall on the bottom and a transparent wall on the top. The incoming air velocity varied from 0.9 to 2.5 m/s, corresponding to a Reynolds number range based on channel height of 340 to 940. Temperature distributions on the heated surface were first measured in a plain channel to establish baseline results. A fully conjugate numerical model was also developed to facilitate data reduction. The accuracy of the model was validated by comparing numerical predictions on the span-averaged temperature distribution along the heated surface to the measurements.

  Investigation on vortex-enhanced flows started from a single winglet pair deployed at 15º, 30º and 45º, respectively. The attack angle of 30º was found to yield the best heat transfer performance and thus adopted for multipair VGs, which included a two-pair V-array, inline two-row pairs, and a three-pair V-array. The proposed V-array demonstrated superiority in heat transfer to the conventional multirow design and the boost effect by the trailing pair was consistent throughout the entire Reynolds number range. Under the affected-area-based criterion, the two-pair V-array yields 14-32% heat transfer augmentation for the current channel flow, as compared to 7-19% and 15-27% obtained from the conventional two-row pairs and the three-pair V-array, respectively.

- *CFD Simulation.* 3D CFD analysis was conducted to illustrate the evolving process of counter-rotating longitudinal vortices. The simulated core shape agreed qualitatively with the dye visualization experiment (Leweke and Williamson, 1998). The skewed structure, as well as increasing distance between the cores of the pair along the streamwise direction, was well

explained by the method of images (Jacobi and Shah, 1995). The existence of affected and unaffected regions as shown in the streamline patterns upheld the use of the affected-area-based method. The CFD simulation also provided pressure drop data over the affected cross section along the entire channel for *Re*=340. The values for the single pair, two-pair V-array, two-row pairs, and three-pair V-array were computed to be 0.449, 0.487, 0.475, and 0.512 Pa, respectively. Using an overall performance evaluation criterion of the modified London area goodness factor ($j/f^{1/3}$) and assuming $j/f^{1/3}$ for the single pair to be unity, the normalized $j/f^{1/3}$ for the two-pair V-array, two-row pairs, and three-pair V-array were found to be 1.012, 0.956, and 0.999, respectively.

Based on the heat transfer and pressure drop performance and taking other factors such as manufacturing cost and spatial constraints into consideration, this study recommends the two-pair V-array deployed at 30º as an appropriate design for implementation in prototype plain-fin heat exchangers. Note that pressure drop across a heat exchanger is usually small relative to the overall loss in typical air-handling units.

- *Implementation in a Prototype Heat Exchanger – Performance Impact in Application*. The V-array design was finally investigated in a prototype plain-fin-and-tube heat exchanger through full-scale wind-tunnel testing under dry surface conditions. This work provided new and thus more complete experimental data on the performance of VG-enhanced heat exchangers where the tube and end effects may be important. Therefore it was useful to assess the true potential of the vortex-enhancement strategy.

  Two angles of attack, 10º and 30º, were examined for the two-pair V-array. The baseline configuration without VGs and two conventional single-pair designs, all deployed at 30º, were included for comparison. The frontal air velocity ranged from 2.3 to 5.5 m/s, corresponding to a Reynolds number range based on the hydraulic diameter of 1400 to 3400. The experimental results showed little impact of the 10º V-array and a moderate heat transfer

improvement of up to 32% for the small pair, both introducing additional pressure loss of approximately 20-40%. For the 30º array and the large pair, similar augmentation of 25-55% in air-side heat transfer coefficients was obtained, accompanied by an average pressure drop penalty of 90% and 140%, respectively. The incremental fan power required to overcome the pressure drop penalty for the 30º V-array was calculated to be less than 5.0 W. Overall performance evaluation using the criteria of the modified area goodness factor and the volume goodness factor indicated superiority of the heat exchanger enhanced by the 30º V-array. Specifically, the average enhancement ratio of 1.21 in $j/f^{1/3}$ over the Reynolds number range considered amounted to 25% reduction in A_{tot}. As a result, the heat exchanger can be manufactured with less material, which allows more compactness and hopefully reduces cost. The size reduction also means a smaller volume of refrigerant to be used. This reduction could be a significant saving in the manufacture of refrigeration equipment. The VG array was found more effective at comparatively low Reynolds numbers, representative of many HVAC&R applications and compact heat exchanger designs.

5.2 Future Work

The proposed array design may be further improved through optimization of winglet geometry (most likely by judiciously increasing the aspect ratio of winglet and ratio of winglet height to fin pitch) and deployment relative to the tube. A computational analysis, for example using the commercial CFD solver FLUENT, has been proven a powerful tool in determining a placement strategy that makes the best use of tube-wake management. In a practical manufacturing process, the winglets will probably be punched out of the fin surface. The effects of holes should be addressed as well in this case[†].

With demonstrated effectiveness under dry-surface conditions, the potential of V-array under wet and frosting conditions needs to be examined in future work. Particularly, high enhancement is expected in wet-surface conditions because the swirl motion induced by longitudinal vortices assists in condensate drainage and reduces blockage in the flow passage. Further research should be directed at full understanding of the relationship between vortex flow, condensate retention, heat transfer enhancement, and sensible heat ratio. In addition, the vortex-generation technique has been found useful in improving heat transfer and the overall performance in a microchannel (Liu *et al*., 2011). Application of the V-array to microscale geometries may be promising and is worth future investigations.

[†] A most recent numerical study by He *et al*. (2012) modeled similar heat exchanger geometry to the present prototype testing and assessed the impact of V-array with respect to the attack angle and placement, where the punched holes on the fin were considered. The authors compared the performance between V-arrays with and without spacing and a large pair of the same area. In the presence of holes, similar findings were drawn in that the zero-spacing V-array caused the least pressure drop penalty and was most effective in relatively low Reynolds number range.

BIBLIOGRAPHY

Allison, C. B., and Dally, B. B., 2007, "Effect of a Delta-Winglet Vortex Pair on the Performance of a Tube-Fin Heat Exchanger," *International Journal of Heat and Mass Transfer*, Vol. 50, pp. 5065-5072.

Astarita, T., Gardone, G., and Carlomagno, G. M., 2006, "Infrared Thermography: An Optical Method in Heat Transfer and Fluid Flow Visualzation," *Optics and Lasers in Engineering*, Vol. 44, pp. 261-281.

Bergman, T. L., Lavine, A. S., Incropera, F. P., and DeWitt, D. P., 2011, *Fundamentals of Heat and Mass Transfer*, 7th ed., John Wiley & Sons, Inc., New York.

Biswas, G., Deb, P., and Biswas, P., 1994, "Generation of Longitudinal Streamwise Vortices – A Device for Improving Heat Exchanger Design," *ASME Journal of Heat Transfer*, Vol. 116, pp. 588-597.

Bougeard, D., 2007, "Infrared Thermography Investigation of Local Heat Transfer in a Plate Fin and Two-Tube Rows Assembly," International Journal of Heat and Fluid Flow, Vol. 28, pp. 988-1002.

Brassard, D., and Ferchichi, M., 2005, "Transformation of a Polynomial for a Contraction Wall Profile," *ASME Journal of Fluids Engineering*, Vol. 127, pp. 183-185.

Bushnell, D. M., and Moore, K. J., 1991, "Drag Reduction in Nature," *Annual Review of Fluid Mechanics*, Vol. 23, pp. 65-79.

Chang, L.-M., Wang, L.-B., Song, K.-W., Sun, D.-L., and Fan, J.-F., 2009, "Numerical Study of the Relationship between Heat Transfer Enhancement and Absolute Vorticity Flux along Main Flow Direction in a Channel Formed by a Flat Tube Bank Fin with Vortex Generators," *International Journal of Heat and Mass Transfer*, Vol. 52, pp. 1794-1801.

Chen, Y., Fiebig, M., and Mitra, N. K., 1998a, "Conjugate Heat Transfer of a Finned Oval Tube with a Punched Longitudinal Vortex Generator in Form of a Delta Winglet – Parametric Investigation of the Winglet," *International Journal of Heat and Mass Transfer*, Vol. 41, pp. 3961-3978.

Chen, Y., Fiebig, M., and Mitra, N. K., 1998b, "Heat Transfer Enhancement of a Finned Oval Tube with Punched Longitudinal Vortex Generators In-Line," *International Journal of Heat and Mass Transfer*, Vol. 41, pp. 4151-4166.

Chen, Y., Fiebig, M., and Mitra, N. K., 2000, "Heat Transfer Enhancement of Finned Oval Tubes with Staggered Punched Longitudinal Vortex Generators," *International Journal of Heat and Mass Transfer*, Vol. 43, pp. 417-435.

Chiu, W. K. S., Richards, C. J., and Jaluria, Y., 2001, "Experimental and Numerical Study of Conjugate Heat Transfer in a Horizontal Channel Heated from Below," *ASME Journal of Heat Transfer*, Vol. 123, pp. 688-697.

Chu, P., He, Y. L., and Tao, W. Q., 2009a, "Three-Dimensional Numerical Study of Flow and Heat Transfer Enhancement Using Vortex Generators in Fin-and-Tube Heat Exchangers," *ASME Journal of Heat Transfer*, Vol. 131, pp. 091903.

Chu, P., He, Y. L., Lei, Y. G., Tian, L. T., and Li, R., 2009b, "Three-Dimensional Numerical Study on Fin-and-Oval-Tube Heat Exchanger with Longitudinal Vortex Generators," *Applied Thermal Engineering*, Vol. 29, pp. 859-876.

DeJong, N. C., and Jacobi, A. M., 1997, "An Experimental Study of Flow and Heat Transfer in Parallel-Plate Arrays: Local, Row-by-Row and Surface Average Behavior," *International Journal of Heat and Mass Transfer*, Vol. 40, pp. 1365-1378.

Dietz, C. F., Henze, M., Neumann, S. O., Wolfersdorf, J. von, and Weigand, B., 2006, "The Effects of Vortex Structures on Heat Transfer and Flow Field Behind Multielement Arrays of Vortex Generators," *Proceedings of the 13th International Heat Transfer Conference*, Paper No. HTE-12.

Elsherbini, A., and Jacobi, A. M., 2002, "The Thermal-Hydraulic Impact of Delta-Wing Vortex Generators on the Performance of a Plain-Fin-and-Tube Heat Exchanger," *HVAC&R Research*, Vol. 8, pp. 357–370.

Fiebig, M., Valencia, A., and Mitra, N. K., 1993, "Wing-Type Vortex Generators for Fin-and-Tube Heat Exchangers," *Experimental Thermal and Fluid Science*, Vol. 7, pp. 287-295.

Fiebig, M., Valencia, A., and Mitra, N. K., 1994, "Local Heat Transfer and Flow Losses in Fin-and-Tube Heat Exchangers with Vortex Generators: A Comparison of Round and Flat Tubes," *Experimental Thermal and Fluid Science*, Vol. 8, pp. 35-45.

Fiebig, M., 1995, "Embedded Vortices in Internal Flow: Heat Transfer and Pressure Loss Enhancement," *International Journal of Heat and Fluid Flow*, Vol. 16, pp. 376-388.

Fiebig, M., 1998, "Vortices, Generators and Heat Transfer," *Chemical Engineering Research and Design*, Vol. 76(2), pp. 108-123.

Fujikura, Y., Suzuki, T., and Matsumoto, M., 1982, "Emissivity of Chlorinated Polyethylene," *Journal of Applied Polymer Science*, Vol. 27, pp. 1293-1300.

Gao, S. D., Wang, L. B., Zhang, Y. H., and Ke, F., 2003, "The Optimum Height of Winglet Vortex Generators Mounted on Three-Row Flat Tube Bank Fin," *ASME Journal of Heat Transfer*, Vol. 125, pp. 1007-1016.

Gentry, M. C., 1998, “Heat Transfer Enhancement Using Tip and Junction Vortices,” Ph.D. dissertation, University of Illinois, Urbana, IL.

Gentry, M. C., and Jacobi, A. M., 2002, “Heat Transfer Enhancement by Delta-Wing-Generated Tip Vortices in Flat-Plate and Developing Channel Flows,” *ASME Journal of Heat Transfer*, Vol. 124, pp. 1158-1168.

He, Y. L., Han, H., Tao, W. Q., and Zhang, Y. W., 2012, “Numerical Study of Heat-Transfer Enhancement by Punched Winglet-Type Vortex Generator Arrays in Fin-and-Tube Heat Exchangers,” *International Journal of Heat and Mass Transfer*, Vol. 55, pp. 5449–5458.

He, J., Liu, L., and Jacobi, A. M., 2011a, “Numerical and Experimental Investigation of Laminar Channel Flow With a Transparent Wall,” *ASME Journal of Heat Transfer*, Vol. 133, pp. 061701.

He, J., Liu, L., and Jacobi, A. M., 2011b, “Conjugate Thermal Analysis of Air-Cooled Discrete Flush-Mounted Heat Sources in a Horizontal Channel,” *ASME Journal of Electronic Packaging*, Vol. 133, pp. 041001.

Hou, X. G., Siveter, D. J., Aldridge, R. J., and Siveter, D. J., 2008, “Collective Behavior in an Early Cambrian Arthropod,” *Science*, Vol. 322, p. 224.

Il’yasov, S. G., and Krasnikov, V. V., 1973, “Indirect Methods for Determining Optical Characteristics of Radiation Scattering Materials,” *Journal of Engineering Physics*, Vol. 19(5), pp. 1424-1428.

Jacobi, A. M., and Shah, R. K., 1995, “Heat Transfer Surface Enhancement through the Use of Longitudinal Vortices: A Review of Recent Progress,” *Experimental Thermal and Fluid Science*, Vol. 11, pp. 295-309.

Joardar, A., and Jacobi, A. M., 2005, “Impact of Leading Edge Delta-Wing Vortex Generators on the Thermal Performance of a Flat Tube, Louvered-Fin Compact Heat Exchanger,” *International Journal of Heat and Mass Transfer*, Vol. 48, pp. 1480–1493.

Joardar, A., and Jacobi, A. M., 2007, “A Numerical Study of Flow and Heat Transfer Enhancement Using an Array of Delta-Winglet Vortex Generators in a Fin-and-Tube Heat Exchanger,” *ASME Journal of Heat Transfer*, Vol. 129, pp. 1156-1167.

Joardar, A., and Jacobi, A. M., 2008, “Heat Transfer Enhancement by Winglet-Type Vortex Generator Arrays in Compact Plain-Fin-and-Tube Heat Exchangers,” *International Journal of Refrigeration*, Vol. 31, pp. 87–97.

Kays, W. M., and London, A. L., 1998, *Compact Heat Exchangers*, 3rd ed., McGraw-Hill, New York.

Kwak, K. M., Torii, K., and Nishino, K., 2005, "Simultaneous Heat Transfer Enhancement and Pressure Loss Reduction for Finned-Tube Bundles with the First or Two Transverse Rows of Built-In Winglets," *Experimental Thermal and Fluid Science*, Vol. 29, pp. 625-632.

Lawson, M. J., and Thole, K. A., 2008, "Heat Transfer Augmentation along the Tube Wall of a Louvered Fin Heat Exchanger Using Practical Delta Winglets," *International Journal of Heat and Mass Transfer*, Vol. 51, pp. 2346-2360.

Leu, J. S., Wu, Y. H., and Jang, J. Y., 2004, "Heat Transfer and Fluid Flow Analysis in Plate-Fin and Tube Heat Exchangers with a Pair of Block Shape Vortex Generators," *International Journal of Heat and Mass Transfer*, Vol. 47, pp. 4327-4338.

Leweke, T., and Williamson, C. H. K., 1998, "Three-Dimensional Dynamics of a Counterrotating Vortex Pair," 8th International Symposium on Flow Visualization, pp. 271.1-271.9.

Lin, C.-N., and Jang, J.-Y., 2002, "Conjugate Heat Transfer and Fluid Flow Analysis in Fin-Tube Heat Exchangers with Wave-Type Vortex Generators," *Journal of Enhanced Heat Transfer*, Vol. 9, pp. 123-136.

Lissaman, P. B. S., and Shollenberger, C. A., 1970, "Formation Flight of Birds," *Science*, Vol. 168, pp. 1003–1005.

Liu, L., and Jacobi, A. M., 2009, "Air-Side Surface Wettability Effects on the Performance of Slit-Fin-and-Tube Heat Exchangers Operating Under Wet-Surface Conditions," *ASME Journal of Heat Transfer*, Vol. 131, pp. 051802.

Liu, C. H., and Sparrow, E. M., 1980, "Convective-Radiative Interaction in a Parallel Plate Channel – Application to Air-Operated Solar Collectors," *International Journal of Heat and Mass Transfer*, Vol. 23, pp. 1137-1146.

Liu, C., Teng, J.-T., Chu, J.-C., Chiu, Y.-L., Huang, S., Jin, S., Dang, T., Greif, R., Pan, H.-H., 2011, "Experimental Investigations on Liquid Flow and Heat Transfer in Rectangular Microchannel with Longitudinal Vortex Generators," *International Journal of Heat and Mass Transfer*, Vol. 54, pp. 3069-3080.

Liu, S., Wang, L. B., Fan, J. F., Zhang, Y. H., Dong, Y. X., and Song, K. W., 2008, "Tube Transverse Pitch Effect on Heat/Mass Transfer Characteristics of Flat Tube Bank Fin Mounted with Vortex Generators," *ASME Journal of Heat Transfer*, Vol. 130, pp. 064502.

Lozza, G., and Merlo, U., 2001, "An Experimental Investigation of Heat Transfer and Friction Losses of Interrupted and Wavy Fins for Fin-and-Tube Heat Exchangers," *International Journal of Refrigeration*, Vol. 24, pp. 409–416.

Min, C., Qi, C., Kong, X., and Dong, J., 2010, "Experimental Study of Rectangular Channel with Modified Rectangular Longitudinal Vortex Generators," *International Journal of Heat and Mass Transfer*, Vol. 53, pp. 3023-3029.

Mori, M., Novak, L., and Sekavĉnik, M., 2007, "Measurements on Rotating Blades Using IR Thermography," *Experimental Thermal and Fluid Science*, Vol. 32, pp. 387-396.

O'Brien, J. E., Sohal, M. S., and Wallstedt, P. C., 2004, "Local Heat Transfer and Pressure Drop for Finned-Tube Heat Exchangers Using Oval Tubes and Vortex Generators," *ASME Journal of Heat Transfer*, Vol. 126, pp. 826-835.

O'Brien, J. E., and Sohal, M. S., 2005, "Heat Transfer Enhancement for Finned-Tube Heat Exchangers with Winglets," *ASME Journal of Heat Transfer*, Vol. 127, pp. 171-178.

Park, Y.-G., Liu, L., and Jacobi, A. M., 2010, "Rational Approaches for Combining Redundant, Independent Measurements to Minimize Combined Experimental Uncertainty," *Experimental Thermal and Fluid Science*, Vol. 34, pp. 720-724.

Patankar, S. V., 1980, *Numerical Heat Transfer and Fluid Flow*, Hemisphere, New York.

Press, W. H., Teukolsky, S. A., Vetterling, W. T., and Flannery, B. P., 1996, *Numerical Recipes in Fortran*, 2nd ed., Cambridge University, New York.

Saleh, J., 2002, *Fluid Flow Handbook*, 1st ed., McGraw-Hill, New York.

Sanders, P. A., and Thole, K. A., 2006, "Effects of Winglets to Augment Tube Wall Heat Transfer in Louvered Fin Heat Exchangers," *International Journal of Heat and Mass Transfer*, Vol. 49, pp. 4058-4069.

Shah, R. K., and Bhatti, M. S., 1987, "Laminar Convective Heat Transfer in Ducts," *Handbook of Single-Phase Convective Heat Transfer*, Chap. 3, John Wiley & Sons, New York.

Shi, B. Z., Wang, L. B., Gen, F., and Zhang, Y. H., 2006, "The Optimal Fin Spacing for Three-Row Flat Tube Bank Fin Mounted with Vortex Generators," *Heat and Mass Transfer*, Vol. 43, pp. 91-101.

Siegel, R., and Howell, J., 2002, *Thermal Radiation Heat Transfer*, 4th ed., Taylor & Francis, New York.

Sommers, A. D., and Jacobi, A. M., 2005, "Air-Side Heat Transfer Enhancement of a Refrigeration Evaporator Using Vortex Generation," *International Journal of Refrigeration*, Vol. 28, pp. 1006–1017.

Storey, B. D., and Jacobi, A. M., 1999, "The Effect of Streamwise Vortices on the Frost Growth Rate in Developing Laminar Channel Flows," *International Journal of Heat and Mass Transfer*, Vol. 42, pp. 3877-3802.

Tang, L. H., Zeng, M., and Wang, Q. W., 2009, "Experimental and Numerical Investigation on Air-Side Performance of Fin-and-Tube Heat Exchangers with Various Fin Patterns," *Experimental Thermal and Fluid Science,* Vol. 33, pp. 818-827.

Taylor, B. N., and Kuyatt, C. E., 1994, "Guideline for Evaluating and Expressing the Uncertainty of NIST Measurement Results," *National Institute of Standards and Technology Technical Note* 1297.

Tiggelbeck, St., Mitra, N. K., and Fiebig, M., 1993, "Experimental Investigations of Heat Transfer Enhancement and Flow Losses in a Channel with Double Rows of Longitudinal Vortex Generators," *International Journal of Heat and Mass Transfer,* Vol. 36, pp. 2327-2337.

Torii, K., Kwak, K. M., and Nishino, K., 2002, "Heat Transfer Enhancement Accompanying Pressure-Loss Reduction with Winglet-Type Vortex Generators for Fin-Tube Heat Exchangers," *International Journal of Heat and Mass Transfer,* Vol. 45, pp. 3795-3801.

Tsilingiris, P. T., 2003, "Comparative Evaluation of the Infrared Transmission of Polymer Films," *Energy Conversation and Management,* Vol. 44, pp. 2839-2856.

Wang, C. C., Chang, Y. J., Wei, C. S., and Yang, B. C., 2004, "A Comparative Study of the Airside Performance of Winglet Vortex Generator and Wavy Fin-and-Tube Heat Exchangers," *ASHRAE Transactions,* Vol. 110, pp. 53–57.

Wang, L. B., Ke, F., Gao, S. D., and Mei, Y. G., 2002, "Local and Average Characteristics of Heat/Mass Transfer Over Flat Tube Bank Fin with Four Vortex Generators Per Tube," *ASME Journal of Heat Transfer,* Vol. 124, pp. 546-552.

Wang, C.-C., Lo, J., Lin, Y.-T., and Wei, C.-S., 2002, "Flow Visualization of Annular and Delta Winglet Vortex Generators in Fin-and-Tube Heat Exchanger Application," *International Journal of Heat and Mass Transfer,* Vol. 45, pp. 3803-3815.

Wang, C. C., Webb, R. L., and Chi, K. Y., 2000, "Data Reduction for Air-Side Performance of Fin-and-Tube Heat Exchangers," *Experimental Thermal and Fluid Science,* Vol. 21, pp. 218-226.

Webb, R. L., and Kim, N.-H., 2005, *Principles of Enhanced Heat Transfer,* 2nd ed., Taylor & Francis, New York.

Weihs, D., 1973, "Hydromechanics of Fish Schooling," *Nature,* Vol. 241, pp. 290–291.

Wu, J. M., and Tao, W. Q., 2007, "Investigation on Laminar Convection Heat Transfer in Fin-and-Tube Heat Exchanger in Aligned Arrangement with Longitudinal Vortex Generator from the Viewpoint of Field Synergy Principle," *Applied Thermal Engineering*, Vol. 27, pp. 2609-2617.

Wu, J. M., and Tao, W. Q., 2008, "Numerical Study on Laminar Convection Heat Transfer in a Channel with Longitudinal Vortex Generator. Part B: Parametric Study of Major Influence Factors," *International Journal of Heat and Mass Transfer*, Vol. 51, pp. 3683-3692.

Wu, J. M., Zhang, H., Yan, C. H., and Wang, Y., 2012, "Experimental Study on the Performance of a Novel Fin-Tube Air Heat Exchanger with Punched Longitudinal Vortex Generator," *Energy Conversion and Management*, Vol. 57, pp. 42-48.

Yang, W.-J., 2001, *Handbook of Flow Visualization*, 2nd ed., Taylor & Francis, New York.

Yuan, Z.-X., Tao, W.-Q., and Yan, X. T., 2003, "Experimental Study on Heat Transfer in Ducts with Winglet Disturbanes," *Heat Transfer Engineering*, Vol. 24(2), pp. 76-84.

Zhang, Y. H., Wang, L. B., Ke, F., Su, Y. X., and Gao, S. D., 2004a, "The Effects of Span Position of Winglet Vortex Generators on Local Heat/Mass Transfer over a Three-Row Flat Tube Bank Fin," *Heat and Mass Transfer*, Vol. 40, pp. 881-891.

Zhang, Y. H., Wang, L. B., Su, Y. X., and Gao, S. D., 2004b, "Effects of the Pitch of In-Line Delta Winglet Vortex Generators on Heat Transfer of a Finned Three-Row Flat Tube Bank," *Experimental Heat Transfer*, Vol. 17, pp. 69-90.

APPENDIX A

COMPUTER CODE FOR THE CONJUGATE MODEL

The computer code describes a 2D numerical model that solves the full elliptic governing equations with the SIMPLER scheme (Patankar, 1980) and accounts for all possible participating heat transfer modes including mixed convection, radiative exchange, and conduction in the substrate. The model has been validated by experiments and successfully used for thermal analysis in laminar channel flows with transparent or opaque boundaries (He *et al*., 2011a, 2011b). The inputs includes: geometries of the 2D domain, transport properties of working fluid, radiative properties of solid surfaces, inlet temperature/velocity profiles, and thermal boundary conditions. The outputs are: 2D temperature distributions in the whole domain, Nusselt number distributions, solid-fluid interface conditions, the stream function, and CPU time consumed. The program also checks mass and energy conversation.

```
C**********************************************************************
C THIS IS MAIN PROGRAM                                                 *
C**********************************************************************
      PROGRAM CONJUGATE_MODEL
      INCLUDE 'COMN.FOR'
      REAL(4) TIME,TA(2)
      OPEN(UNIT=1,FILE='TEMP2D.DAT')
      OPEN(UNIT=2,FILE='ITFACE.DAT')
      OPEN(UNIT=3,FILE='VELCTY.DAT')
      OPEN(UNIT=4,FILE='NUSSET.DAT')
      OPEN(UNIT=5,FILE='STREAM.DAT')
      OPEN(UNIT=6,FILE='OUTPUT.DAT')
      OPEN(UNIT=7,FILE='RADLOS.DAT')
C---------------------------------------------------------------
C TRANSPORT & GEOMETRIC PARAMETERS
C---------------------------------------------------------------
      XL=16.       !CHANNEL LENGTH
      DX=0.05      !GRID SIZE IN X-COORDINATE (UNIFORM)
      DY=0.025     !AVERAGE GRID SIZE IN FLUID REGIME (NONUNIFORM)
      RE=1000.     !REYNOLDS NUMBER BASED ON CHANNEL HEIGHT
      PR=0.707     !PRANDTL NUMBER OF FLUID
      GR=5.E5      !GRASHOF NUMBER BASED ON HEAT FLUX
```

```
      R1=1.4552       !RADIATIVE NUSSELT NUMBER
      R2=0.5666       !INDEX OF HEATING POWER
      HW=0.           !RATIO OF WALL THICKNESS TO CHANNEL HEIGHT
      DW=0.01         !GRID SIZE IN WALL REGIME
      NW=ANINT(HW/DW)   !NUMER OF GRIDS IN WALL REGIME
      RK=1.E-6          !RATIO OF THERMAL CONDUCTIVITY,KS/KF
      REX=1.            !UNDERRELAXATION PARAMETER FOR QRAD
      EI=0.             !EMISSIVITY OF INLET ENVIRONMENT
      EO=0.             !EMISSIVITY OF OUTLET ENVRIONMENT
      EWALL=0.          !EMISSIVITY OF WALL SUBSTRATE
      ESRCE=0.          !EMISSIVITY OF HEAT SOURCES
      STRX=SMALL        !STRETCHING FACTOR IN X-COORDINATE
      STRY=SMALL        !STRETCHING FACTOR IN Y-COORDINATE
      TREF=1./(R1*R2)   !REFERENCE TEMPERATURE
      CALL XUYV
      CALL GRID
      CALL ZERO
      NI1=ANINT(1./DX)*2+2
      NO1=ANINT(1./DX)*3+1
      NI2=ANINT(1./DX)*4+2
      NO2=ANINT(1./DX)*5+1
      NI3=ANINT(1./DX)*6+2
      NO3=ANINT(1./DX)*7+1
      NI4=ANINT(1./DX)*8+2
      NO4=ANINT(1./DX)*9+1
      DO 10 I=1,L1
      IF((I.GE.NI1.AND.I.LE.NO1).OR.(I.GE.NI2.AND.I.LE.NO2).OR.
     .(I.GE.NI3.AND.I.LE.NO3).OR.(I.GE.NI4.AND.I.LE.NO4))THEN
      EB(I)=ESRCE     !EMISSIVITY OF BOTTOM WALL SURFACE
      ELSE
      EB(I)=EWALL
      ENDIF
      ET(I)=EWALL     !EMISSIVITY OF TOP WALL SURFACE
      RB(I)=1.-EB(I)  !REFLECTIVITY OF BOTTOM WALL SURFACE
      RT(I)=1.-ET(I)  !REFLECTIVITY OF TOP WALL SURFACE
10    CONTINUE
C--- SYMMETRIC HEATING ---
C     DO 10 I=1,L1
C     IF((I.GE.NI1.AND.I.LE.NO1).OR.(I.GE.NI2.AND.I.LE.NO2).OR.
C    .(I.GE.NI3.AND.I.LE.NO3).OR.(I.GE.NI4.AND.I.LE.NO4))THEN
C     EB(I)=ESRCE     !EMISSIVITY OF BOTTOM WALL SURFACE
C     ET(I)=ESRCE
C     ELSE
C     EB(I)=EWALL
C     ET(I)=EWALL
C     ENDIF
```

```
C       RB(I)=1.-EB(I)   !REFLECTIVITY OF BOTTOM WALL SURFACE
C       RT(I)=1.-ET(I)   !REFLECTIVITY OF TOP WALL SURFACE
C10     CONTINUE
C-----------------------------------------------------------------
        LRAD=.FALSE.    !RADIATION IS INCLUDED IF LRAD=TRUE
        LOUT=.TRUE.     !EXIT T=T0 IF LOUT=TRUE; T=TM IF LOUT=FALSE
        LSTOP=.FALSE.   !ITERATION STOPS IF LSTOP=TRUE
C-----------------------------------------------------------------
        CF=YCV(1+NW)/(RK*YCV(2+NW)+YCV(1+NW))
        CS=RK*YCV(2+NW)/(RK*YCV(2+NW)+YCV(1+NW))
C--- VIEW FACTOR ----------------------------------------------------
        IF(LRAD)THEN
        DO 15 K=2,L2
        DO 15 L=2,L2
        XS=SQRT((XU(K+1)-XU(L))**2+1.)+SQRT((XU(K)-XU(L+1))**2+1.)
        UX=SQRT((XU(K)-XU(L))**2+1.)+SQRT((XU(K+1)-XU(L+1))**2+1.)
        VF(K-1,L-1)=0.5*(XS-UX)/XCV(K)
        A1(K-1,L-1)=VF(K-1,L-1)*RB(K)
15      A2(K-1,L-1)=VF(K-1,L-1)*RT(K)
        ENDIF
C-----------------------------------------------------------------
C--- NUMBER OF SWEEPS ---
        DO 20 I=1,NFMAX
20      NTIMES(I)=10
C
C--- RELAXATION FACTOR---
        RELAX(1)=0.6          !U
        RELAX(2)=0.6          !V
        RELAX(3)=1.           !P
        RELAX(4)=1.           !P'
        RELAX(5)=1.           !T
C
C--- VARIABLES TO BE SOLVED ---
        LSOLVE(1)=.TRUE.      !U
        LSOLVE(2)=.TRUE.      !V
        LSOLVE(3)=.TRUE.      !P
        LSOLVE(4)=.TRUE.      !P'
        LSOLVE(5)=.TRUE.      !T
C-----------------------------------------------------------------
C INITIAL CONDITIONS
C-----------------------------------------------------------------
        DO 35 I=1,L1
        IF((I.GE.NI1.AND.I.LE.NO1).OR.(I.GE.NI2.AND.I.LE.NO2).OR.
       .(I.GE.NI3.AND.I.LE.NO3).OR.(I.GE.NI4.AND.I.LE.NO4))THEN
        Q1(I)=1.
        ENDIF
```

```
35      CONTINUE
C
C       DO 36 I=1,L1
        DO 36 J=2+NW,M2
36      U(2,J)=1.                                !UNIFORM PROFILE
C36     U(I,J)=6.*(Y(J)-HW)*(1.+HW-Y(J))    !PARABOLIC PROFILE
C
        DO 45 I=1,L1
        DO 45 J=1,M1
45      T(I,J)=TREF
C---------------------------------------------------------------------
C CONJUGATE HEAT TRANSFER
C---------------------------------------------------------------------
1000    CONTINUE
        DO 50 I=1,L1
        C0(I)=(Q1(I)-QR1(I))*YCV(1+NW)*YCV(2+NW)/2./
       .(RK*YCV(2+NW)+YCV(1+NW))
        TW(I)=CS*T(I,1+NW)+CF*T(I,2+NW)+C0(I)
50      QD1(I)=2.*RK*(TW(I)-T(I,1+NW))/MAX(SMALL,YCV(1+NW))
C
        IF(LRAD)THEN
        DO 55 I=1,L3
        J10(I)=J1(I)
        J20(I)=J2(I)
        G10(I)=G1(I)
55      G20(I)=G2(I)
        CALL RAD
        ENDIF
        DO 56 I=1,L1
        QV1(I)=Q1(I)-QD1(I)-QR1(I)
56      QV2(I)=Q2(I)-QR2(I)
C
C--- UPDATE U,V,T ---
        DO 70 I=1,L1
        DO 70 J=1,M1
        IF(I.NE.1)U0(I,J)=U(I,J)
        IF(J.NE.1)V0(I,J)=V(I,J)
70      T0(I,J)=T(I,J)
C
        CALL EQN
C
C--- CHECK CONVERGENCE ---
        RMAX=0.
        RSUM=0.
        DO 80 J=1,M1
        DO 80 I=1,L1
```

```
      IF(I.NE.1)THEN
      RMAX=MAX(RMAX,ABS(U(I,J)-U0(I,J)))
      RSUM=RSUM+ABS(U(I,J)-U0(I,J))
      ENDIF
      IF(J.NE.1)THEN
      RMAX=MAX(RMAX,ABS(V(I,J)-V0(I,J)))
      RSUM=RSUM+ABS(V(I,J)-V0(I,J))
      ENDIF
      RMAX=MAX(RMAX,ABS(T(I,J)-T0(I,J)))
80    RSUM=RSUM+ABS(T(I,J)-T0(I,J))
      IF(LRAD)THEN
      DO 90 I=1,L3
      RMAX=MAX(RMAX,ABS(J1(I)-J10(I)),ABS(J2(I)-J20(I)))
90    RSUM=RSUM+ABS(J1(I)-J10(I))+ABS(J2(I)-J20(I))
      ENDIF
C
      WRITE(*,91)ICONT,'RESIDUAL MAX = ',RMAX,'RESIDUAL SUM =
      ',RSUM
91    FORMAT(I8,A18,E12.6,A18,E12.6)
      WRITE(*,*)
      WRITE(*,*)'TOUT = ',TOUT
      WRITE(*,*)
      IF(RMAX.LT.1.E-8)LSTOP=.TRUE.
      IF(ICONT.GT.ITMAX)LSTOP=.TRUE.
      IF(.NOT.LSTOP)GOTO 1000
C---------------------------------------------------------------------
C OUTPUT
C---------------------------------------------------------------------
C--- 2D TEMPERATURE DISTRIBUTION ---
      WRITE(1,*)'VARIABLES="X","Y","TEMPERATURE"'
      WRITE(1,109)'ZONE I=',L1,',J=',M1,',F=POINT'
      TMAX=0.
      DO 110 J=1,M1
      DO 110 I=1,L1
      WRITE(1,119)X(I),Y(J),T(I,J)/TREF
      IF(T(I,J).GT.TMAX)THEN
      TMAX=T(I,J)
      XTMAX=X(I)
      YTMAX=Y(J)
      ENDIF
110   CONTINUE
      WRITE(6,*)' TMAX = ',TMAX/TREF
      WRITE(6,*)' TMAX OCCURS AT X = ',XTMAX,' Y = ',YTMAX
      WRITE(6,*)
109   FORMAT(1X,A,I5,A,I5,A)
119   FORMAT(2F9.4,F12.6)
```

```
C
C--- INTERFACE QUANTITIES ---
      DO 120 I=2,L2
      WRITE(2,121)X(I),TW(I)/TREF,QV1(I),QD1(I),QR1(I),QV2(I),QR2(I)
120   CONTINUE
121   FORMAT(F9.4,6F12.6)
C
C--- NUSSELT NUMBER ---
      NUAVG=0.
      DO 140 I=2,L2
      TM=0.
      DO 141 J=2+NW,M2
141   TM=TM+T(I,J)*(U(I,J)+U(I+1,J))/2.*YCV(J)
      NUM(I)=QV1(I)/(TW(I)-TM)
      NU0(I)=QV1(I)/(TW(I)-TREF)
      NUAVG=NUAVG+NUM(I)*XCV(I)/XL
      WRITE(4,149)X(I),NUM(I),NU0(I)
140   CONTINUE
149   FORMAT(F9.4,2F13.6)
      WRITE(6,*)' AVERAGE NUSSELT = ',NUAVG
      WRITE(6,*)
C
C--- STREAM FUNCTION ---
      F(2,2,9)=0.
      DO 152 I=2,L1
      IF(I.NE.2) F(I,2,9)=F(I-1,2,9)-V(I-1,2)*XCV(I-1)
      DO 152 J=3+NW,M1
152   F(I,J,9)=F(I,J-1,9)+U(I,J-1)*YCV(J-1)
      WRITE(5,*)'VARIABLES="X","Y","STREAMFUNCTION"'
      WRITE(5,109)'ZONE I=',L2,',J=',M2-NW,',F=POINT'
      DO 155 J=2+NW,M1
      DO 155 I=2,L1
      WRITE(5,119)X(I),Y(J),F(I,J,9)
155   CONTINUE
C
C--- CONSERVATION CHECK ---
      XLS1=0.
      XLS2=0.
      DO 180 K=2,L2
      XI1=XCV(K)*FK(XU(K),XU(K+1))*(J1(K-1)-1./R2)
      XO1=XCV(K)*FK(XU(L1)-XU(K+1),XU(L1)-XU(K))
      LOSS1(K)=XI1+XO1*(J1(K-1)-(TOUT/TREF)**4/R2)
      XLS1=XLS1+LOSS1(K)
      XI2=XCV(K)*FK(XU(K),XU(K+1))*(J2(K-1)-1./R2)
      LOSS2(K)=XI2+XO1*(J2(K-1)-(TOUT/TREF)**4/R2)
      XLS2=XLS2+LOSS2(K)
```

```
      WRITE(7,181)X(K),LOSS1(K),LOSS2(K),G1(K-1),G2(K-1)
180   CONTINUE
181   FORMAT(F9.4,4E15.6)
C
      XMASS=0.
      XENEG=0.
      DO 185 J=2,M2
      XMASS=XMASS+U(L1,J)*YCV(J)
185   XENEG=XENEG+(U(L1,J)*T(L1,J)-U(2,J)*T(1,J))*YCV(J)*RE*PR
      XTOT=XLS1+XLS2+XENEG
      WRITE(6,*)'MASS AT THE EXIT IS =',XMASS
      WRITE(6,*)
      WRITE(6,*)'MASS CONSERVATIO IS =',(XMASS-1.)*100.,'%'
      WRITE(6,*)
      WRITE(6,*)'FLOW ENERGY INCREASE IS =',XENEG
      WRITE(6,*)
      WRITE(6,*)'RAD LOSS FROM BOTTOM IS =',XLS1
      WRITE(6,*)
      WRITE(6,*)'RAD LOSS FROM TOP IS =',XLS2
      WRITE(6,*)
      WRITE(6,*)'TOTAL ENERGY GAIN IS =',XTOT
      WRITE(6,*)
      WRITE(6,*)'ENERGY CONSERVATIO IS =',(XTOT-4.)/4.*100.,'%'
      WRITE(6,*)
C
    TIME=DTIME(TA)
      WRITE(*,*)
      WRITE(*,*)'THE CPU TIME IS',TIME,'SECONDS'
      WRITE(6,*)'THE CPU TIME IS',TIME,'SECONDS'
      END
C*********************************************************************
      SUBROUTINE XUYV
      INCLUDE 'COMN.FOR'
C*********************************************************************
      L3=ANINT(XL/DX)
      L2=L3+1
      L1=L3+2
      XU(1)=0.
      DO 1 I=2,L1
      TANH1=TANH(STRX*(REAL(I-2)/REAL(L3)-0.5))
1     XU(I)=(1.+TANH1/TANH(STRX/2.))*XL/2.
C
      M3=NW+ANINT(1./DY)
      M2=M3+1
      M1=M3+2
      YV(1)=0.
```

```
      DO 2 J=2,1+NW
2     YV(J)=REAL(J-2)*DW
      DO 5 J=2+NW,M1
      TANH1=TANH(STRY*(REAL(J-2-NW)/REAL(M3-NW)-0.5))
5     YV(J)=HW+0.5*(1.+TANH1/TANH(STRY/2.))
      RETURN
      END
C*********************************************************************
      SUBROUTINE GAMSOR
      INCLUDE 'COMN.FOR'
C     GAM - DIFFUSION COEFFICIENT
C     CON - SC*DV (DEFAULT ZERO)
C     AP  - SP    (DEFAULT ZERO)
C*********************************************************************
C U-MOMENTUM
      IF(NF.EQ.1)THEN
      IF(HW.GT.SMALL)THEN
      DO 2 I=1,L1
      DO 1 J=1,M1
      IF(J.LE.1+NW)THEN
      GAM(I,J)=LARGE
      ELSE
      GAM(I,J)=1./RE
      ENDIF
1     CONTINUE
2     CONTINUE
      ELSE
      DO 3 I=1,L1
      DO 3 J=1,M1
3     GAM(I,J)=1./RE
      ENDIF
C
C V-MOMENTUM
      ELSEIF(NF.EQ.2)THEN
      IF(HW.GT.SMALL)THEN
      DO 5 I=1,L1
      DO 4 J=1,M1
      IF(J.LE.1+NW)THEN
      GAM(I,J)=LARGE
      ELSE
      GAM(I,J)=1./RE
      ENDIF
4     CONTINUE
5     CONTINUE
      ELSE
      DO 6 I=1,L1
```

```
      DO 6 J=1,M1
6     GAM(I,J)=1./RE
      ENDIF
      DO 7 J=JST,M2
      DO 7 I=IST,L2
      CON(I,J)=(YCVJP(J-1)*(T(I,J-1)-TREF)+YCVJ(J)*(T(I,J)-TREF))*
     .XCV(I)*GR/RE**2
7     CONTINUE
C
C T-ENERGY
      ELSEIF(NF.EQ.5)THEN
      IF(HW.GT.SMALL)THEN
      DO 9 I=1,L1
      DO 8 J=1,M1
      IF(J.LE.1+NW)THEN
      GAM(I,J)=RK/(RE*PR)
      ELSE
      GAM(I,J)=1./(RE*PR)
      ENDIF
8     CONTINUE
9     CONTINUE
      ELSE
      DO 10 I=1,L1
      DO 10 J=1,M1
10    GAM(I,J)=1./(RE*PR)
      ENDIF
      ENDIF
      RETURN
      END
C*********************************************************************
      SUBROUTINE BCUV
      INCLUDE 'COMN.FOR'
C*********************************************************************
      DO 1 J=1,M1
      U(L1,J)=U(L2,J)
      IF(J.NE.1)V(L1,J)=V(L2,J)
1     CONTINUE
      RETURN
      END
C*********************************************************************
      SUBROUTINE BCT
      INCLUDE 'COMN.FOR'
C*********************************************************************
      DO 1 J=1,M1
1     T(L1,J)=T(L2,J)              !EXIT
      DO 2 I=2,L2
```

```
2       T(I,M1)=T(I,M2)+YDIF(M1)*QV2(I)  !TOP
C
        IF(HW.GT.SMALL)THEN
        DO 3 I=2,L2
3       T(I,1)=T(I,2)
        DO 4 J=1,1+NW
4       T(1,J)=T(2,J)
        ELSE
        DO 5 I=2,L2
5       T(I,1)=T(I,2)+YDIF(2)*QV1(I)
        ENDIF
        RETURN
        END
C*******************************************************************
        SUBROUTINE COEFFICIENT
        INCLUDE 'COMN.FOR'
C*******************************************************************
        DO 10 I=2,L2
        J=1+NW                  !INTERFACE - SOLID DOMAIN
        AN0=GAM(I,J)*XCV(I)/(0.5*YCV(J))
        SUM=AIP(I,J)+AIM(I,J)+AJM(I,J)+AN0
        AJP(I,J)=AN0*CF
        AP(I,J)=SUM/RELAX(NF)-AN0*CS
        CON(I,J)=AN0*C0(I)+(1.-RELAX(NF))*SUM/RELAX(NF)*F(I,J,NF)
C
        J=2+NW                  !INTERFACE - FLUID DOMAIN
        AS0=GAM(I,J)*XCV(I)/(0.5*YCV(J))
        SUM=AIP(I,J)+AIM(I,J)+AJP(I,J)+AS0
        AJM(I,J)=AS0*CS
        AP(I,J)=SUM/RELAX(NF)-AS0*CF
        CON(I,J)=AS0*C0(I)+(1.-RELAX(NF))*SUM/RELAX(NF)*F(I,J,NF)
10      CONTINUE
        RETURN
        END
C*******************************************************************
        SUBROUTINE GRID
        INCLUDE 'COMN.FOR'
C*******************************************************************
        X(1)=XU(2)
        DO 33 I=2,L2
33      X(I)=0.5*(XU(I+1)+XU(I))
        X(L1)=XU(L1)
        Y(1)=YV(2)
        DO 34 J=2,M2
34      Y(J)=0.5*(YV(J+1)+YV(J))
        Y(M1)=YV(M1)
```

```
      DO 35 I=2,L1
35    XDIF(I)=X(I)-X(I-1)
      DO 36 I=1,L2
36    XCV(I)=XU(I+1)-XU(I)
      DO 37 I=3,L2
37    XCVS(I)=XDIF(I)
      XCVS(3)=XCVS(3)+XDIF(2)
      XCVS(L2)=XCVS(L2)+XDIF(L1)
      DO 38 I=3,L3
      XCVI(I)=0.5*XCV(I)
38    XCVIP(I)=XCVI(I)
      XCVIP(2)=XCV(2)
      XCVI(L2)=XCV(L2)
      DO 39 J=2,M1
39    YDIF(J)=Y(J)-Y(J-1)
      DO 40 J=1,M2
40    YCV(J)=YV(J+1)-YV(J)
      DO 45 J=3,M2
45    YCVS(J)=YDIF(J)
      YCVS(3)=YCVS(3)+YDIF(2)
      YCVS(M2)=YCVS(M2)+YDIF(M1)
C-----------------------------------------------------------------
      DO 66 J=3,M3
      YCVJ(J)=0.5*YCV(J)
66    YCVJP(J)=YCVJ(J)
      YCVJP(2)=YCV(2)
      YCVJ(M2)=YCV(M2)
C-----------------------------------------------------------------
      RETURN
      END
C*****************************************************************
      SUBROUTINE ZERO
      INCLUDE 'COMN.FOR'
C*****************************************************************
      DO 2 I=1,NI
      DO 1 J=1,NJ
      PC(I,J)=0.
      U(I,J)=0.
      V(I,J)=0.
      CON(I,J)=0.
      AP(I,J)=0.
      P(I,J)=0.
      T(I,J)=0.
1     CONTINUE
      Q1(I)=0.
      Q2(I)=0.
```

```
      QD1(I)=0.
      QD2(I)=0.
      QR1(I)=0.
      QR2(I)=0.
      QV1(I)=0.
      QV2(I)=0.
      J1(I)=0.
      G1(I)=0.
      J2(I)=0.
      G2(I)=0.
2     CONTINUE
      RETURN
      END
C*****************************************************************
      SUBROUTINE RAD
      INCLUDE 'COMN.FOR'
      INTEGER JS(L3)
      REAL*8 B1(L3),B2(L3),X3(L3),CC(L3,L3),DD(L3)
C*****************************************************************
      IF(LOUT)THEN
      TOUT=TREF
      ELSE
      TOUT=0.
      DO 5 J=2+NW,M2
5     TOUT=TOUT+T(L1,J)*U(L1,J)*YCV(J)
      ENDIF
C
      TEP=R1**4*R2**3
      DO 10 K=2,L2
      WS=EB(K)*TEP*TW(K)**4
      WI=EI*RB(K)*FK(XU(K),XU(K+1))/R2
      WO=EO*RB(K)*FK(XU(L1)-XU(K+1),XU(L1)-XU(K))*TEP*TOUT**4
      B1(K-1)=WS+WI+WO
      WS=ET(K)*TEP*T(K,M1)**4
      WI=EI*RT(K)*FK(XU(K),XU(K+1))/R2
      WO=EO*RT(K)*FK(XU(L1)-XU(K+1),XU(L1)-XU(K))*TEP*TOUT**4
      B2(K-1)=WS+WI+WO
10    CONTINUE
C
      DO 25 K=1,L3
      DD(K)=0.
      DO 20 L=1,L3
      CC(K,L)=0.
      DO 15 J=1,L3
15    CC(K,L)=CC(K,L)+A1(K,J)*A2(J,L)
      IF(L.EQ.K)THEN
```

```
      CC(K,L)=1.-CC(K,L)
      ELSE
      CC(K,L)=-CC(K,L)
      ENDIF
      DD(K)=DD(K)+A1(K,L)*B2(L)
20    CONTINUE
      DD(K)=DD(K)+B1(K)
25    CONTINUE
C
      CALL GAUSS(CC,DD,L3,X3,LL,JS)
C
      DO 35 K=1,L3
      J1(K)=X3(K)
      J2(K)=0.
      DO 30 L=1,L3
30    J2(K)=J2(K)+A2(K,L)*X3(L)
35    J2(K)=J2(K)+B2(K)
C
      DO 45 K=1,L3
      G1(K)=0.
      G2(K)=0.
      DO 40 L=1,L3
      G1(K)=G1(K)+VF(K,L)*J2(L)
40    G2(K)=G2(K)+VF(K,L)*J1(L)
      WI=EI*FK(XU(K+1),XU(K+2))/R2
      WO=EO*FK(XU(L1)-XU(K+2),XU(L1)-XU(K+1))*TEP*TOUT**4
      G1(K)=G1(K)+WI+WO
45    G2(K)=G2(K)+WI+WO
C
      DO 50 K=2,L2
      QR1(K)=REX*(J1(K-1)-G1(K-1))+(1.-REX)*(J10(K-1)-G10(K-1))
50    QR2(K)=REX*(J2(K-1)-G2(K-1))+(1.-REX)*(J20(K-1)-G20(K-1))
      CONTINUE
      RETURN
      END
C
      REAL*8 FUNCTION FK(X1,X2)
      IMPLICIT REAL*8 (A-H,O-Z)
      IF(ABS(X1).LT.1.E-30) X1=1.E-30
      IF(ABS(X2).LT.1.E-30) X2=1.E-30
      F1=0.5*(1.+1./X1-SQRT(1.+1./X1**2))
      F2=0.5*(1.+1./X2-SQRT(1.+1./X2**2))
      FK=(X2*F2-X1*F1)/(X2-X1)
      RETURN
      END
```

```
C*****************************************************************
      SUBROUTINE GAUSS(A,B,N,X,L,JS)
      IMPLICIT REAL*8 (A-H,O-Z)
      INTEGER JS(N)
      REAL*8 A(N,N),X(N),B(N)
C*****************************************************************
      L=1
      DO 50 K=1,N-1
      D=0.
      DO 210 I=K,N
      DO 210 J=K,N
      IF(ABS(A(I,J)).GT.D)THEN
      D=ABS(A(I,J))
      JS(K)=J
      IS=I
      ENDIF
210   CONTINUE
      IF(ABS(D).LT.1.E-30)THEN
      L=0
      ELSE
      IF(JS(K).NE.K)THEN
      DO 220 I=1,N
      T=A(I,K)
      A(I,K)=A(I,JS(K))
      A(I,JS(K))=T
220   CONTINUE
      ENDIF
      IF(IS.NE.K)THEN
      DO 230 J=K,N
      T=A(K,J)
      A(K,J)=A(IS,J)
      A(IS,J)=T
230   CONTINUE
      T=B(K)
      B(K)=B(IS)
      B(IS)=T
      ENDIF
      ENDIF
      IF(L.EQ.0)THEN
      WRITE(*,100)
      RETURN
      ENDIF
      DO 10 J=K+1,N
10    A(K,J)=A(K,J)/A(K,K)
      B(K)=B(K)/A(K,K)
      DO 30 I=K+1,N
```

```
      DO 20 J=K+1,N
      A(I,J)=A(I,J)-A(I,K)*A(K,J)
20    CONTINUE
      B(I)=B(I)-A(I,K)*B(K)
30    CONTINUE
50    CONTINUE
C
      IF(ABS(A(N,N)).LT.1.E-30)THEN
      L=0
      WRITE(*,100)
      RETURN
      ENDIF
      X(N)=B(N)/A(N,N)
      DO 70 I=N-1,1,-1
      T=0.
      DO 60 J=I+1,N
      T=T+A(I,J)*X(J)
60    CONTINUE
      X(I)=B(I)-T
70    CONTINUE
C
100   FORMAT(1X,'FAIL')
      JS(N)=N
      DO 150 K=N,1,-1
      IF(JS(K).NE.K)THEN
      T=X(K)
      X(K)=X(JS(K))
      X(JS(K))=T
      ENDIF
150   CONTINUE
      RETURN
      END
C*********************************************************************
      SUBROUTINE EQN
      INCLUDE 'COMN.FOR'
C*********************************************************************
C U-EQUATION
C---------------------------------------------------------------
      NF=1
      IF(.NOT.LSOLVE(NF))GOTO 500
      IST=3
      JST=2
      CALL GAMSOR
C
      REL=1.-RELAX(NF)
      DO 102 I=3,L2
```

```
      FL=XCVI(I)*V(I,2)
      FLM=XCVIP(I-1)*V(I-1,2)
      FLOW=FL+FLM
      DIFF=(XCVI(I)*GAM(I,1)+XCVIP(I-1)*GAM(I-1,1))/YDIF(2)
      CALL DIFLOW
102   AJM(I,2)=ACOF+MAX(0.,FLOW)
      DO 103 J=2,M2
      FLOW=YCV(J)*U(2,J)
      DIFF=YCV(J)*GAM(1,J)/XCV(2)
      CALL DIFLOW
      AIM(3,J)=ACOF+MAX(0.,FLOW)
      DO 103 I=3,L2
      IF(I.EQ.L2)GOTO 104
      FLOW=YCV(J)*0.5*(U(I,J)+U(I+1,J))
      DIFF=YCV(J)*GAM(I,J)/XCV(I)
      GOTO 105
104   FLOW=YCV(J)*U(L1,J)
      DIFF=YCV(J)*GAM(L1,J)/XCV(L2)
105   CALL DIFLOW
      AIM(I+1,J)=ACOF+MAX(0.,FLOW)
      AIP(I,J)=AIM(I+1,J)-FLOW
      IF(J.EQ.M2)GOTO 106
      FL=XCVI(I)*V(I,J+1)
      FLM=XCVIP(I-1)*V(I-1,J+1)
      GM=GAM(I,J)*GAM(I,J+1)/(YCV(J)*GAM(I,J+1)+YCV(J+1)*GAM(I,J)+
     .SMALL)*XCVI(I)
      GMM=GAM(I-1,J)*GAM(I-1,J+1)/(YCV(J)*GAM(I-1,J+1)+YCV(J+1)*
     .GAM(I-1,J)+SMALL)*XCVIP(I-1)
      DIFF=2.*(GM+GMM)
      GOTO 107
106   FL=XCVI(I)*V(I,M1)
      FLM=XCVIP(I-1)*V(I-1,M1)
      DIFF=(XCVI(I)*GAM(I,M1)+XCVIP(I-1)*GAM(I-1,M1))/YDIF(M1)
107   FLOW=FL+FLM
      CALL DIFLOW
      AJM(I,J+1)=ACOF+MAX(0.,FLOW)
      AJP(I,J)=AJM(I,J+1)-FLOW
      VOL=YCV(J)*XCVS(I)
      AP(I,J)=(-AP(I,J)*VOL+AIP(I,J)+AIM(I,J)+AJP(I,J)+AJM(I,J))/
     .RELAX(NF)
      CON(I,J)=CON(I,J)*VOL+REL*AP(I,J)*U(I,J)
      DU(I,J)=VOL/XDIF(I)/AP(I,J)
103   CONTINUE
      DO 130 K=1,6
      DO 130 J=JST,M2
      DO 130 I=IST,L2
```

```
      COFU(I,J,K)=COF(I,J,K)
130   CONTINUE
C-------------------------------------------------------------------
C V-EQUATION
C-------------------------------------------------------------------
      CALL RESET
      NF=2
      IF(.NOT.LSOLVE(NF))GOTO 500
      IST=2
      JST=3
      CALL GAMSOR
C
      REL=1.-RELAX(NF)
      DO 202 I=2,L2
      FLOW=XCV(I)*V(I,2)
      DIFF=XCV(I)*GAM(I,1)/YCV(2)
      CALL DIFLOW
202   AJM(I,3)=ACOF+MAX(0.,FLOW)
      DO 203 J=3,M2
      FLOW=YCVJ(J)*U(2,J)+YCVJP(J-1)*U(2,J-1)
      DIFF=(YCVJ(J)*GAM(1,J)+YCVJP(J-1)*GAM(1,J-1))/XDIF(2)
      CALL DIFLOW
      AIM(2,J)=ACOF+MAX(0.,FLOW)
      DO 203 I=2,L2
      IF(I.EQ.L2)GOTO 204
      FL=YCVJ(J)*U(I+1,J)
      FLM=YCVJP(J-1)*U(I+1,J-1)
      GM=GAM(I,J)*GAM(I+1,J)/(XCV(I)*GAM(I+1,J)+XCV(I+1)*GAM(I,J)+
     .SMALL)*YCVJ(J)
      GMM=GAM(I,J-1)*GAM(I+1,J-1)/(XCV(I)*GAM(I+1,J-1)+XCV(I+1)*
     .GAM(I,J-1)+SMALL)*YCVJP(J-1)
      DIFF=2.*(GM+GMM)
      GOTO 205
204   FL=YCVJ(J)*U(L1,J)
      FLM=YCVJP(J-1)*U(L1,J-1)
      DIFF=(YCVJ(J)*GAM(L1,J)+YCVJP(J-1)*GAM(L1,J-1))/XDIF(L1)
205   FLOW=FL+FLM
      CALL DIFLOW
      AIM(I+1,J)=ACOF+MAX(0.,FLOW)
      AIP(I,J)=AIM(I+1,J)-FLOW
      IF(J.EQ.M2)GOTO 206
      FV=YCVJP(J)/YCV(J)
      FLOW=(FV*V(I,J)+(1.-FV)*V(I,J+1))*XCV(I)
      DIFF=XCV(I)*GAM(I,J)/YCV(J)
      GOTO 207
206   FLOW=XCV(I)*V(I,M1)
```

```
      DIFF=XCV(I)*GAM(I,M1)/YCV(M2)
207   CALL DIFLOW
      AJM(I,J+1)=ACOF+MAX(0.,FLOW)
      AJP(I,J)=AJM(I,J+1)-FLOW
      VOL=YCVS(J)*XCV(I)
      AP(I,J)=(-AP(I,J)*VOL+AIP(I,J)+AIM(I,J)+AJP(I,J)+AJM(I,J))/
     .RELAX(NF)
      CON(I,J)=CON(I,J)+REL*AP(I,J)*V(I,J)
      DV(I,J)=VOL/YDIF(J)/AP(I,J)
203   CONTINUE
C
      DO 230 K=1,6
      DO 230 J=JST,M2
      DO 230 I=IST,L2
230   COFV(I,J,K)=COF(I,J,K)
C---------------------------------------------------------------------
C CALCULATE U^ AND V^
C---------------------------------------------------------------------
      DO 150 J=2,M2
      DO 150 I=3,L2
150   UHAT(I,J)=(COFU(I,J,2)*U(I+1,J)+COFU(I,J,3)*U(I-1,J)+COFU(I,J,4)
     .*U(I,J+1)+COFU(I,J,5)*U(I,J-1)+COFU(I,J,1))/COFU(I,J,6)
      DO 250 J=3,M2
      DO 250 I=2,L2
250   VHAT(I,J)=(COFV(I,J,2)*V(I+1,J)+COFV(I,J,3)*V(I-1,J)+COFV(I,J,4)
     .*V(I,J+1)+COFV(I,J,5)*V(I,J-1)+COFV(I,J,1))/COFV(I,J,6)
C---------------------------------------------------------------------
C P EQUATION
C---------------------------------------------------------------------
      CALL RESET
      NF=3
      IST=2
      JST=2
C
      DO 402 I=2,L2
      CON(I,2)=CON(I,2)+XCV(I)*V(I,2)
402   AJM(I,2)=0.
      DO 403 J=2,M2
      CON(2,J)=CON(2,J)+YCV(J)*U(2,J)
      AIM(2,J)=0.
      DO 403 I=2,L2
      IF(I.EQ.L2)GOTO 404
      FLOW=YCV(J)*UHAT(I+1,J)
      CON(I,J)=CON(I,J)-FLOW
      CON(I+1,J)=CON(I+1,J)+FLOW
      AIP(I,J)=YCV(J)*DU(I+1,J)
```

```
      AIM(I+1,J)=AIP(I,J)
      GOTO 405
404   CON(I,J)=CON(I,J)-YCV(J)*U(L1,J)
      AIP(I,J)=0.
405   IF(J.EQ.M2)GOTO 406
      FLOW=XCV(I)*VHAT(I,J+1)
      CON(I,J)=CON(I,J)-FLOW
      CON(I,J+1)=CON(I,J+1)+FLOW
      AJP(I,J)=XCV(I)*DV(I,J+1)
      AJM(I,J+1)=AJP(I,J)
      GOTO 407
406   CON(I,J)=CON(I,J)-XCV(I)*V(I,M1)
      AJP(I,J)=0.
407   AP(I,J)=AIP(I,J)+AIM(I,J)+AJP(I,J)+AJM(I,J)
403   CONTINUE
      DO 421 J=2,M2
      DO 421 I=2,L2
      AP(I,J)=AP(I,J)/RELAX(NF)
421   CON(I,J)=CON(I,J)+(1.-RELAX(NF))*AP(I,J)*P(I,J)
C
      DO 350 K=2,5
      DO 350 J=JST,M2
      DO 350 I=IST,L2
350   COFP(I,J,K)=COF(I,J,K)
      CALL SOLVE
C---------------------------------------------------------------------
C COMPUTE U AND V
C---------------------------------------------------------------------
      NF=1
      IST=3
      JST=2
      DO 550 K=1,6
      DO 550 J=JST,M2
      DO 550 I=IST,L2
550   COF(I,J,K)=COFU(I,J,K)
      DO 551 J=JST,M2
      DO 551 I=IST,L2
551   CON(I,J)=CON(I,J)+DU(I,J)*AP(I,J)*(P(I-1,J)-P(I,J))
      CALL SOLVE
C
      NF=2
      IST=2
      JST=3
      DO 552 K=1,6
      DO 552 J=JST,M2
      DO 552 I=IST,L2
```

```
552     COF(I,J,K)=COFV(I,J,K)
        DO 553 J=JST,M2
        DO 553 I=IST,L2
553     CON(I,J)=CON(I,J)+DV(I,J)*AP(I,J)*(P(I,J-1)-P(I,J))
        CALL SOLVE
C-------------------------------------------------------------------
C P' EQUATION
C-------------------------------------------------------------------
        NF=4
        IST=2
        JST=2
        DO 554 K=2,5
        DO 554 J=JST,M2
        DO 554 I=IST,L2
554     COF(I,J,K)=COFP(I,J,K)
C
        SSUM=0.
        DO 502 I=2,L2
502     CON(I,2)=CON(I,2)+XCV(I)*V(I,2)
        DO 503 J=2,M2
        CON(2,J)=CON(2,J)+YCV(J)*U(2,J)
        DO 503 I=2,L2
        IF(I.EQ.L2)GOTO 504
        FLOW=YCV(J)*U(I+1,J)
        CON(I,J)=CON(I,J)-FLOW
        CON(I+1,J)=CON(I+1,J)+FLOW
        GOTO 505
504     CON(I,J)=CON(I,J)-YCV(J)*U(L1,J)
505     IF(J.EQ.M2)GOTO 506
        FLOW=XCV(I)*V(I,J+1)
        CON(I,J)=CON(I,J)-FLOW
        CON(I,J+1)=CON(I,J+1)+FLOW
        GOTO 507
506     CON(I,J)=CON(I,J)-XCV(I)*V(I,M1)
507     AP(I,J)=AIP(I,J)+AIM(I,J)+AJP(I,J)+AJM(I,J)
        PC(I,J)=0.
        SSUM=SSUM+CON(I,J)
503     CONTINUE
        CALL SOLVE
C-------------------------------------------------------------------
C CORRECT U,V AND APPLY B.C.'S
C-------------------------------------------------------------------
        DO 521 J=2,M2
        DO 521 I=2,L2
        IF(I.NE.2)U(I,J)=U(I,J)+DU(I,J)*(PC(I-1,J)-PC(I,J))
        IF(J.NE.2)V(I,J)=V(I,J)+DV(I,J)*(PC(I,J-1)-PC(I,J))
```

```
521     CONTINUE
        CALL BCUV
500     CONTINUE
C-------------------------------------------------------------------
C T EQUATION
C-------------------------------------------------------------------
        NF=5
        IF(.NOT.LSOLVE(NF))GOTO 600
        IST=2
        JST=2
        CALL GAMSOR
C
        REL=1.-RELAX(NF)
        DO 602 I=2,L2
        FLOW=XCV(I)*V(I,2)
        DIFF=XCV(I)*GAM(I,1)/YDIF(2)
        CALL DIFLOW
602     AJM(I,2)=ACOF+MAX(0.,FLOW)        !AS - SOUTHMOST
C-------------------------------------------------------------------
        DO 603 J=2,M2
        FLOW=YCV(J)*U(2,J)
        DIFF=YCV(J)*GAM(1,J)/XDIF(2)
        CALL DIFLOW
        AIM(2,J)=ACOF+MAX(0.,FLOW)        !AW - WESTMOST
C-------------------------------------------------------------------
        DO 603 I=2,L2
        IF(I.EQ.L2)GOTO 604
        FLOW=YCV(J)*U(I+1,J)
        DIFF=YCV(J)*2.*GAM(I,J)*GAM(I+1,J)/(XCV(I)*GAM(I+1,J)+
       .XCV(I+1)*GAM(I,J)+SMALL)
        GOTO 605
C-------------------------------------------------------------------
604     FLOW=YCV(J)*U(L1,J)
        DIFF=YCV(J)*GAM(L1,J)/XDIF(L1)     !AE - EASTMOST
C-------------------------------------------------------------------
605     CALL DIFLOW
        AIM(I+1,J)=ACOF+MAX(0.,FLOW)
        AIP(I,J)=AIM(I+1,J)-FLOW          !INTERIOR AW & AE
C-------------------------------------------------------------------
        IF(J.EQ.M2)GOTO 606
        FLOW=XCV(I)*V(I,J+1)
        DIFF=XCV(I)*2.*GAM(I,J)*GAM(I,J+1)/(YCV(J)*GAM(I,J+1)+
       .YCV(J+1)*GAM(I,J)+SMALL)
        GOTO 607
C-------------------------------------------------------------------
606     FLOW=XCV(I)*V(I,M1)
```

```
      DIFF=XCV(I)*GAM(I,M1)/YDIF(M1)     !AN - NORTHMOST
C-----------------------------------------------------------------
607   CALL DIFLOW
      AJM(I,J+1)=ACOF+MAX(0.,FLOW)
      AJP(I,J)=AJM(I,J+1)-FLOW                !INTERIOR AS & AN
C-----------------------------------------------------------------
      VOL=YCV(J)*XCV(I)
      AP(I,J)=(-AP(I,J)*VOL+AIP(I,J)+AIM(I,J)+AJP(I,J)+AJM(I,J))/
     .RELAX(NF)
      CON(I,J)=CON(I,J)*VOL+REL*AP(I,J)*F(I,J,NF)
603   CONTINUE
C-----------------------------------------------------------------
      IF(HW.GT.SMALL)CALL COEFFICIENT
      CALL SOLVE
      CALL BCT
600   CONTINUE
C
      ICONT=ICONT+1
      WRITE(*,630)ICONT,SSUM
630   FORMAT(I8,E16.6)
      RETURN
      END
C*****************************************************************
      SUBROUTINE SOLVE
      INCLUDE 'COMN.FOR'
C*****************************************************************
      ISTF=IST-1
      JSTF=JST-1
      IT1=L2+IST
      IT2=L3+IST
      JT1=M2+JST
      JT2=M3+JST
C-----------------------------------------------------------------
      DO 999 NT=1,NTIMES(NF)
      N=NF
C-----------------------------------------------------------------
      DO 90 J=JST,M2
      PT(ISTF)=0.
      QT(ISTF)=F(ISTF,J,N)
      DO 70 I=IST,L2
      DENOM=AP(I,J)-PT(I-1)*AIM(I,J)
      PT(I)=AIP(I,J)/DENOM
      TEMP=CON(I,J)+AJP(I,J)*F(I,J+1,N)+AJM(I,J)*F(I,J-1,N)
      QT(I)=(TEMP+AIM(I,J)*QT(I-1))/DENOM
70    CONTINUE
      DO 80 II=IST,L2
```

```
      I=IT1-II
80    F(I,J,N)=F(I+1,J,N)*PT(I)+QT(I)
90    CONTINUE
C-----------------------------------------------------------------
      DO 190 JJ=JST,M3
      J=JT2-JJ
      PT(ISTF)=0.
      QT(ISTF)=F(ISTF,J,N)
      DO 170 I=IST,L2
      DENOM=AP(I,J)-PT(I-1)*AIM(I,J)
      PT(I)=AIP(I,J)/DENOM
      TEMP=CON(I,J)+AJP(I,J)*F(I,J+1,N)+AJM(I,J)*F(I,J-1,N)
      QT(I)=(TEMP+AIM(I,J)*QT(I-1))/DENOM
170   CONTINUE
      DO 180 II=IST,L2
      I=IT1-II
180   F(I,J,N)=F(I+1,J,N)*PT(I)+QT(I)
190   CONTINUE
C-----------------------------------------------------------------
      DO 290 I=IST,L2
      PT(JSTF)=0.
      QT(JSTF)=F(I,JSTF,N)
      DO 270 J=JST,M2
      DENOM=AP(I,J)-PT(J-1)*AJM(I,J)
      PT(J)=AJP(I,J)/DENOM
      TEMP=CON(I,J)+AIP(I,J)*F(I+1,J,N)+AIM(I,J)*F(I-1,J,N)
      QT(J)=(TEMP+AJM(I,J)*QT(J-1))/DENOM
270   CONTINUE
      DO 280 JJ=JST,M2
      J=JT1-JJ
280   F(I,J,N)=F(I,J+1,N)*PT(J)+QT(J)
290   CONTINUE
C-----------------------------------------------------------------
      DO 390 II=IST,L3
      I=IT2-II
      PT(JSTF)=0.
      QT(JSTF)=F(I,JSTF,N)
      DO 370 J=JST,M2
      DENOM=AP(I,J)-PT(J-1)*AJM(I,J)
      PT(J)=AJP(I,J)/DENOM
      TEMP=CON(I,J)+AIP(I,J)*F(I+1,J,N)+AIM(I,J)*F(I-1,J,N)
      QT(J)=(TEMP+AJM(I,J)*QT(J-1))/DENOM
370   CONTINUE
      DO 380 JJ=JST,M2
      J=JT1-JJ
380   F(I,J,N)=F(I,J+1,N)*PT(J)+QT(J)
```

```
390     CONTINUE
C
999     CONTINUE
        CALL RESET
        RETURN
        END
C*****************************************************************
        SUBROUTINE DIFLOW
        INCLUDE 'COMN.FOR'
C*****************************************************************
        ACOF=DIFF
        IF(FLOW.EQ.0.) RETURN
        TEMP=DIFF-ABS(FLOW)*0.1
        ACOF=0.
        IF(TEMP.LE.0.) RETURN
        TEMP=TEMP/DIFF
        ACOF=DIFF*TEMP**5
        RETURN
        END
C*****************************************************************
        SUBROUTINE RESET
        INCLUDE 'COMN.FOR'
C*****************************************************************
        DO 1 J=2,M2
        DO 1 I=2,L2
        CON(I,J)=0.
1       AP(I,J)=0.
        RETURN
        END
C*****************************************************************
C THIS IS COMN.FOR                                                *
C*****************************************************************
        IMPLICIT REAL*8 (A-H, O-Z)
        REAL*8 LARGE, NUAVG
        PARAMETER (NI=502, NJ=102, NIJ=NI, NFMAX=10, ITMAX=1000000,
       .SMALL=1.D-30, LARGE=1.D30)
        LOGICAL LSOLVE, LSTOP, LRAD, LOUT
        REAL*8F,GAM,CON,AIP,AIM,AJP,AJM,AP,X,XU,XDIF,XCV,XCVS,
       .Y,YV,YDIF,YCV,YCVS,YCVJ,YCVJP,XCVI,XCVIP,DU,DV,PT,QT,
       .Q1,Q2,QD1,QD2,QR1,QR2,QV1,QV2,J1,G1,J2,G2,J10,G10,J20,G20,
       .RELAX,QV10,QV20,C0,TW,EB,ET,RB,RT,NUM,NU0,LOSS1,LOSS2
C
        COMMON F(NI,NJ,NFMAX),GAM(NI,NJ),CON(NI,NJ),AIP(NI,NJ),
       .AIM(NI,NJ),AJP(NI,NJ),AJM(NI,NJ),AP(NI,NJ),X(NI),XU(NI),XDIF(NI),
       .XCV(NI),XCVS(NI),Y(NJ),YV(NJ),YDIF(NJ),YCV(NJ),YCVS(NJ),
       .YCVJ(NJ),YCVJP(NJ),XCVI(NI),XCVIP(NI),DU(NI,NJ),DV(NI,NJ),
```

```
     .PT(NIJ),QT(NIJ),Q1(NI),Q2(NI),QD1(NI),QD2(NI),QR1(NI),QR2(NI),
     .QV1(NI),QV2(NI),J1(NI),G1(NI),J2(NI),G2(NI),J10(NI),G10(NI),J20(NI),
     .G20(NI),RELAX(NFMAX),QV10(NI),QV20(NI),C0(NI),TW(NI),
     .NUM(NI),NU0(NI),LOSS1(NI),LOSS2(NI)
C
      COMMON/COEF/FLOW,DIFF,ACOF
      COMMON/RADG/VF(NI,NI),A1(NI,NI),A2(NI,NI),EB(NI),ET(NI),RB(NI),
     .RT(NI)
      COMMON/PARA/XL,DX,DY,RE,PR,GR,R1,R2,HW,DW,RK,REX,EI,EO,
     .CF,CS,STRX,STRY,TREF,TOUT
      COMMON/INDX/NF,L1,L2,L3,M1,M2,M3,IST,JST,ICONT,NW,LOUT,
     .LRAD,NI1,NO1,NI2,NO2,NI3,NO3,NI4,NO4,LSOLVE(NFMAX),
     .NTIMES(NFMAX)
C
      REAL*8 U(NI,NJ),V(NI,NJ),P(NI,NJ),PC(NI,NJ),T(NI,NJ),U0(NI,NJ),
     .V0(NI,NJ),T0(NI,NJ),UHAT(NI,NJ),VHAT(NI,NJ),COF(NI,NJ,6),
     .COFU(NI,NJ,6),COFV(NI,NJ,6),COFP(NI,NJ,6)
      EQUIVALENCE(F(1,1,1),U(1,1)),(F(1,1,2),V(1,1)),(F(1,1,3),P(1,1)),
     .(F(1,1,4),PC(1,1)),(F(1,1,5),T(1,1)),(COF(1,1,1),CON(1,1))
```